UNIVERSIDAD AUTÓNOMA DE MADRID

Departamento de Física de Materiales

Nonlinear Optical Waveguides in $LiNbO_3$ and Periodically Poled $LiNbO_3$

Olga Caballero Calero

Madrid, 10th May 2007.

UNIVERSIDAD AUTÓNOMA DE MADRID
Departamento de Física de Materiales

Nonlinear Optical Waveguides in $LiNbO_3$ and Periodically Poled $LiNbO_3$

Dissertation presented by
Olga Caballero Calero
submitted to the Universidad Autónoma de Madrid,
to obtain the title of Doctor in Science.

Thesis Directors:
Dr. Mercedes Carrascosa Rico
Dr. Ángel García Cabañes

Madrid, 10th May 2007

A Óscar

A mis padres

I have no special talent.

I am only passionately curious

– Albert Einstein

Contents

Aknowledgements - Agradecimientos

Me gustaría, en primer lugar, agradecer a mis directores de Tesis, Mercedes Carrascosa y Ángel García Cabañes, su ayuda a lo largo de estos años, poniendo siempre todos los medios a su alcance para que este trabajo fuera posible. La paciencia de Ángel, cuando recurría incansablemente a él o el tiempo que me ha dedicado Mercedes haciendo siempre hueco para atenderme, me han servido para descubrir no sólo el mundo científico, sino también la suerte que he tenido de que estas dos excelentes personas hayan estado conmigo todo el camino (incluso en el duro sprint final). También me gustaría incluir aquí a José Manuel Cabrera, alma del laboratorio de Óptica No Lineal. Su confianza y buen humor (y el pincho) han hecho que fuera fundamental para mi trabajo. Y "'last but not least"', Fernando Agulló-López, gracias por contagiarnos a todos de tu entusiasmo y vitalidad (¡aunque no consigamos seguir tu ritmo!).

Otro de los pilares fundamentales de mi tesis ha sido el Departamento de Física de Materiales, donde se ha desarrollado mi vida estos últimos años. El alto nivel profesional de sus miembros combinado con su magnífico carácter, hacen de este departamento un lugar excelente a nivel intelectual y humano. Me gustaría agradecer especialmente a Ginés Lifante y el grupo AMIGO el haberme proporcionado muestras de guías

de cinc y a Ernesto Diéguez y Verónica Bermúdez por facilitarme niobato de litio periódicamente polarizado, que han hecho posibles gran parte de los resultados de esta tesis. Y especialmente a Francisco Jaque, que espero que pronto esté de nuevo entre nosotros, por haberme medido los PPLNs con el SNOM. También en esta línea, agradecer a José Olivares y su grupo del CMAM las guías irradiadas y la ayuda proporcionada a lo largo de estos años. En realidad, todos los laboratorios han estado siempre abiertos para mí, tanto para utilizar su material como para escuchar y resolver mis consultas: José Manuel Calleja en cuyo laboratorio hice mi primera *estancia*; todos los miembros del Laboratorio de Crecimiento de Cristales, dónde me adoptaron desde el comienzo de mi tesis; Luis Arizmendi, quien me introdujo en el mundo de la Óptica; Carmen de las Heras, siempre dispuesta a escucharme... Y todos los miembros del departamento: Carlos Sánchez, Fernando Cussó, Fernando López, José García Solé, Luis Viña, Luisa Bausá, Carmen Aragó, Dani Jaque, Eugenio Cantelar, Fernando Moreno, Teo... que han hecho de mis días aquí una experiencia inolvidable, a la que ha contribuido de manera muy especial Elías y Emilio, anímica y gastronómicamente.

From my stay in Boston University, I would like to thank Prof. Sergienko, Prof. Saleh, and Prof. Teich, who trusted me and gave me the opportunity of working in their group. And all the people who worked there and helped me to learn that one can work on its own but never be alone. Lunch and coffe would not have been the same without Hugues, Greg, Martin, ... Specially, I would like to thank Silvia Carrasco, who was there to back me when I was learning how to do everything all by my self. Your company made everything seem easier. ¡Gracias!

Other place where I have lived for some time was Bonn, in the group of Prof. Buse. There I found exceptional scientists and, what is more important, real good friends. I am so grateful to all of you, that I do

not know how to begin ... Karsten, Elisabeth, Theo, Dirk, Thorsten, Katharina, and all the others made my stay there one of the most profitable periods of my thesis, always willing to help me and discuss about physic (or whatever). And then Ingo, Rosita and Helge, who made me always feel at home, and the ones who suffered me the most, that is Michael and Ulrich, who spent a lot of time in the lab with me (and in the mountains, too). Endlich habe ich es geschafft!! Klingt kömisch, ist aber so. Vielen, vielen Dank!!

Muchos doctorandos y post-docs han pasado por el C-IV mientras realizaba mi tesis. Puede parecer exagerado, pero guardo muy buenos recuerdos de todos ellos, aunque muchas veces nos veíamos menos de lo que me hubiera gustado. Me gustaría agradecerles el haber estado a mi lado y todo lo que hemos pasado juntos. Eva, Fabrice, Pablo Díaz, José Ramón, Sne, Alberto, Pablo Molina, Marta, Emma, Dario, Airán, Antonio, Jorge, Iván, Javi, Carmen, Edgardo, Verónica, José Luis, Gabriel, Ana García... ha sido un placer haber estado con vosotros. Y los del CMAM, José Olivares, siempre con ideas nuevas en la cabeza y cerca del teléfono para escuchar mis dudas, Miguel Crespillo (menudas tardes de microscopio...) y Andrés (tu risa y la proyección estereográfica del $LiNbO_3$ son inolvidables). Gracias a ellos, el acelerador ha sido como una tercera casa para mí. ¡Y qué decir de mis compañeros de despacho! Jesús, con quien también he compartido laboratorio, Javier, que en poco tiempo se ha convertido en un apoyo realmente importante para seguir adelante y, cómo no, Dipankar, con su paciencia y su buen humor. También me gustaría destacar a una serie de doctores y amigos que han ayudado a que todo fuera más fácil: Bruno y Aída, cuidándome física y anímicamente, Juan José Romero, pendiente y alerta para echar una mano, aunque sea en la distancia, Ángel Méndez, quien me cuida e incordia a partes iguales (pero con mucho cariño) y Lola Martín, que siempre está ahí para lo que se necesite.

A mis amigos de la facultad, que de una forma u otra han soportado estoicamente todos estos años a mi lado, no puedo dejar de mencionarlos aquí. Con muchos he compartido aficiones que me han ayudado a seguir adelante (y a canalizar mi hiperactividad, claro). Aikido (Loren, Javi, Anita...), Kempo (Lucía, Jorge...), la Coral de Materiales del CSIC (José Antonio, Josefina, Alicia, Elena, Cristina...), Japonés (Akiko, Juan Pablo...) me han ayudado a conocer a gente fantástica y a cambiar de aires de vez en cuando. Desde la carrera, y pese a que ahora seguimos caminos distintos, el cariño de Tania, Elena, Irene, Nico, Jorge, Miguel Ángel, Rodrigo (y Lola), Pablo, Ana, David, Ángel,... me ha seguido siempre. Fuera de la facultad, Quique, Patricia, Charo, Isabel y el resto del Coro, Gema Ballesteros, y nuestra perdurable amistad, Lauri, mi eterna pareja de sevillanas... y muchísimos más que han ayudado a que los ratitos de luz fuera de la oscuridad del laboratorio fueran maravillosos.

Un punto y a parte merecen las personas con las que empecé la tesis y que, de un modo u otro, han trascendido el trabajo y han pasado a ser realmente importantes en mi vida. El que ahora esté escribiendo esto es culpa vuestra (y que lo escriba en LaTeX sobre todo). Gonzalo, siempre a mi lado, sobre todo al principio; Jaime, una de las personas más preparadas y capaces que conozco (y organizada); Ángel Alcázar, quien consigue que tener una familia estupenda, ser un amigo maravilloso y patinar de miedo parezca cosa fácil. Estoy en deuda con todos vosotros por lo que me habeís enseñado, por vuestra paciencia y por vuestro cariño. Gonzalo, Jaime, Ángel... os quiero un montón.

Y los que sin duda tienen un importante lugar, tanto en esta tesis como en mi vida, son mis amigos de siempre, más lejos (María, Joa, Flapy, Otín), o más cerca (Wolfo, Juan, Jesús, Raúl, José, Pili...), pero siempre juntos. En cuanto a Estrella (¡llevamos mil años juntas!), Andrés (uy, otra vez ¿será porque te has leído esta tesis ya dos veces?), Ana, David, Begoña,

Raúl, Jorge y Alex, sólo espero que sigamos compartiendo nuestras vidas, por mucho que cambien. No os imagináis cuánto significaís para mí.

Finalmente, me gustaría mencionar a mi familia. A la de siempre, a la que me ha visto crecer y en la que me ha apoyado tantas veces: mis primos, Bea, Pedro, Miriam, Philip, Ángel, Teresa, Carol, Juan, Alberto, Nano, Inma... mis tíos Pilar, Luis, Marisi, Ascen, Carlos, Bea y Fernando... mi familia "'postiza"' M. Carmen, Javi, Loli, Sergio, Espe y, cómo no, M. Bel. Todos habeís estado pendientes de mis viajes, me habeís ofrecido vuestras casas y vuestro cariño. Y a la familia "'más nueva"', que me ha aceptado como soy y ha estado muy presente estos últimos años de tesis: Alberto, Luisa, Alberto, Meli... Por último, gracias a mis abuelos, Luis y Carmina, que todas las noches me pedían un resumen de lo que había hecho en el día, de quienes sigo aprendiendo y a los que tanto admiro. Aunque a los que no conseguiré agradecer suficientemente todo lo que han hecho por mí, y lo que me han aguantado son, cómo no, mis padres. Gracias. Por como sois, por lo que me habeís inculcado, por compartir las preocupaciones conmigo, por ayudarme a ser fuerte... y por otras mil cosas que siempre haceís como si fuera lo más normal del mundo. ¡Sois los mejores!

Muchos de los que he mencionado se merecerían un libro a parte, y habrá algunos que se me haya olvidado mencionar, seguro. Pero escribir estas líneas me ha ayudado a recordar buenos momentos, y a agradecer, en la medida de lo posible, toda la ayuda y apoyo que he recibido durante estos años. Ha sido un honor que me hayaís hecho un hueco en vuestras vidas.

Y para acabar, querría dedicar este último párrafo a quien no sólo me ha ayudado a perseguir un sueño, sino que lo ha hecho suyo. Gracias por tu fe en mí, por tu paciencia, por haber estado siempre a mi lado y por hacerme ver que era posible. Óscar, gran parte de esta tesis te la debo a tí.

Preface

The aim of this Thesis work has been the investigation and characterization of the nonlinear response of a variety of $LiNbO_3$ waveguides. To this end, the nonlinear properties of waveguides fabricated by proton exchange (PE), metal in-diffusion and ion irradiation have been studied. Three main topics affecting the efficiency in nonlinear optical frequency conversion processes have been thoroughly investigated:

- The determination of the second order nonlinear susceptibilities of different $LiNbO_3$ waveguides.
- The comparative study of the optical damage effect in a variety of $LiNbO_3$ waveguides, with a exhaustive study of those which presented higher resistance to this effect.
- Fabrication of high quality periodic structures with small period lengths. The combination of these "'quasi-phase-matching"' structures with the waveguide configuration make possible the obtainment of efficient frequency conversion devices.

To cope with all these data, this Thesis has been divided in three main parts: *I. Introduction*, *II. Experimental Techniques*, and *III. Results*.

The first part, *I. Introduction* contains three chapters: *1. Main properties of Lithium Niobate*, where the most relevant linear properties

of this material, as well as the growth techniques and its structure are presented; *2.Nonlinear optical properties of Lithium Niobate* not only the nonlinear optical properties of $LiNbO_3$ which lead to frequency mixing are presented, but also those which depend on the light intensity, such as the Photovoltaic effect, Photorefractive effect, and Optical Damage, which are very important for this thesis work; *3. Nonlineal optical waveguides*, finally, deals with waveguide description, characterization methods and their most relevant characteristics concerning their nonlinear response.

The second part, *II. Experimental Techniques* describes the different experimental techniques used throughout this work. Some of them are standard techniques, but others were carried out in this work. Firstly, the different waveguide fabrication techniques are described, as well as the fabrication of channel waveguides (made for the first time in our laboratory). Secondly, the waveguide characterization techniques are explained, from the most standard ones (profile characterization, optical losses measurement, and absorption) to those in which most of this thesis work has been done (optical damage, photovoltaic current, and nonlinear coefficients measurements). Thirdly, periodic poling of $LiNbO_3$ is described, via the Czochralski off-center growth method and the electric field polarization technique. An important contribution of this thesis work has been the development and adaptation of this technique to the periodic poling of $LiNbO_3$ waveguides with small periods. Finally, different ways of ferroelectric domain characterization are presented.

Also related with the experimental techniques described in this chapter, an appendix has been included, dealing with a new method that provides the actual intensity in the waveguide. This method has been also proposed and developed in the framework of this thesis.

Then, the last part, *III. Results* is devoted to the description of the original results of this thesis work. It has been divided in three chapters

(from 5 to 7):

Chapter *5. Second order susceptibilities of $LiNbO_3$ waveguides* is focused on a thorough study of the nonlinear coefficients of the different waveguides, namely PE, metal in-diffused and ion irradiated waveguides. Therefore, systematic measurements of the relative nonlinear coefficients by the Second Harmonic Generation in the Strong Absorption Regime technique have been carried out. The measurements show that a variety of waveguides preserve essentially the second order non linear coefficients: α -phase PE waveguides ($80 - 90\%$) , Zn-in-diffusion ($\sim 100\%$), Ti-in-diffusion ($\sim 100\%$) and the novel ion irradiated waveguides ($\sim 70\%$).

Chapter *6. Optical Damage* is devoted to the study of this effect in waveguide configuration. From the measurements carried out, the optical damage intensity threshold is obtained, that is, the intensity at which the linearity between the in- and out-coupled intensities is lost. This is a main feature related to nonlinear applications, because it limits the light intensity that the device can support and so their efficiency in non linear optical process. Firstly, a comparative study of the optical damage thresholds in a variety of waveguides is presented, because this aspect had not been enough studied previously.

In order to further understand the phenomena underlying the optical damage, one of its basic mechanisms, namely the photovoltaic transport mechanism, was also investigated. Among the obtained results it is worthwhile to mention the superlinear behavior of the photovoltaic currents in some of the studied waveguides, as well as its relation with the optical damage data.

The second part of this chapter is focused in a deeper study on α-phase PE waveguides, which showed high nonlinear susceptibilities and low optical damage. Different configurations, such as waveguides fabricated in z-cut substrates, channel waveguides and waveguides periodically poled

are studied.

The last chapter of this thesis, *7. Electric Field Periodic Poling* deals with the description and discussion of the periodic poling of α-phase PE waveguides. These waveguides were chosen, as it was mentioned before, because they are suitable for nonlinear devices and, as they are fabricated in our laboratory, they were more available for this work. It is shown how domain period lengths down to $5\,\mu\mathrm{m}$, which is the generally accepted lower limit of this technique at room temperature with congruent $LiNbO_3$, were achieved. At difference with most previous works in PE waveguides, electric field periodic poling was carried out after waveguide fabrication. These obtained periodically poled waveguides had a very good domain period quality, even for the shortest periods of $5\,\mu\mathrm{m}$, and their optical performance was not affected by the domain reversal.

Prefacio

El objetivo de este trabajo de Tesis ha sido la caracterización e investigación de la respuesta no lineal de guías fabricadas sobre $LiNbO_3$. Con este objetivo se han estudiado las propiedades no lineales de guías fabricadas por intercambio protónico (PE del inglés, Proton Exchange), por difusión de metales y por irradiación iónica. Tres factores fundamentales que afectan a la eficiencia de los procesos no lineales de conversión de frecuencia han sido investigados en profundidad:

- Determinación de la susceptibilidad relativa de segundo orden de los diferentes tipos de guías fabricadas en $LiNbO_3$.
- Estudio comparativo del daño óptico que presentan las diferentes guías de $LiNbO_3$, con una caracterización exhaustiva posterior del comportamiento de las guías con bajo daño.
- Fabricación de estructuras periódicas por campo eléctrico de alta calidad y períodos pequeños, aplicables en la conversión de frecuencias de forma muy eficiente, al combinar estructuras de "'quasi-phase-matching"' con la configuración de guía óptica.

La Tesis se ha dividido en tres partes: *I. Introducción*, *II. Técnicas Experimentales*, y *III. Resultados*.

La primera parte, *I. Introducción* contiene tres capítulos: *1. Propiedades básicas del niobato de litio*, dónde se describen las propiedades lineales más relevantes de este material, así como las técnicas de crecimiento habitualmente empleadas y su estructura cristalina; *2.Propiedades no lineales del niobato de litio* trata, no sólo de las propiedades no lineales de segundo orden del $LiNbO_3$, responsables de la mezcla de frecuencias, si no también de aquellos efectos que dependen de la intensidad luminosa, como el efecto fotovoltaico, el efecto fotorrefractivo y el daño óptico, claves en este trabajo; *3. Guías de onda no lineales*, describe los distintos tipos de guía, los métodos de caracterización usualmente empleados y las características más relevantes de su respuesta no lineal.

La segunda parte, *II. Técnicas experimentales* describe de las técnicas experimentales utilizadas. Algunas de ellas son técnicas estándar, pero otras fueron desarrolladas y puestas a punto en este trabajo. En primer lugar se describen las distintas técnicas de fabricación de guías planas, así como la fabricación de guías por PE acanaladas (realizadas por primera vez en nuestro laboratorio). Seguidamente, se pasa a explicar las técnicas de caracterización de guías, desde las más comunes (caracterización del perfil, medida de pérdidas y absorción) hasta las que han sido la base de este trabajo de tesis (daño óptico, corrientes fotovoltaicas y medida de coeficientes no lineales). A continuación, se describen dos técnicas de polarización periódica de $LiNbO_3$: la técnica de crecimiento por Czochralski fuera de eje y la polarización periódica por aplicación de campo externo. Dentro de esta última, y como parte original de este trabajo, se mostrará cómo se ha desarrollado y adaptado para conseguir polarización periódica en guías de onda previamente fabricadas con dominios pequeños. Para finalizar, se describen distintos métodos de caracterización de dominios ferroeléctricos.

En relación con las técnicas descritas en este capítulo, se ha incluido un apéndice en el que se propone un método nuevo para la medida fiable de la intensidad de luz dentro de la guía y que también ha sido desarrollado en esta tesis.

La última parte de la tesis, *III. Resultados* está centrada en la descripción de los resultados originales a los que ha dado lugar este trabajo de tesis y su discusión. Se ha dividido a su vez en tres capítulos (del 5 al 7):

El capítulo *5, Susceptibilidades de segundo orden de guías de onda en $LiNbO_3$*, está centrado en un exhaustivo estudio de los coeficientes no lineales de diversas guías de onda, fabricadas mediante intercambio protónico (PE), difusión de metales e irradiación iónica. Para ello, se han realizado medidas sistemáticas del coeficiente no lineal relativo al del $LiNbO_3$ congruente, mediante la técnica de Generación de Segundo Armónico en Régimen de Alta Absorción. Se muestra cómo ciertos tipos de guías mantienen un alto porcentaje del coeficiente no lineal: PE en fase α ($70 - 90\%$) , difusión de Zn ($\sim 100\%$), y las novedosas guías por irradiación de iones ($\sim 70\%$).

El capítulo *6, Daño Óptico*, está dedicado al estudio de este fenómeno en configuración guiada. De las medidas efectuadas en las distintas guías, se obtiene el umbral de daño óptico, esto es, la intensidad a la cual se pierde la linealidad entre la luz acoplada y la desacoplada en la guía. El conocimiento de estos datos, es fundamental para aplicaciones no lineales, ya que limita la intensidad luminosa que el dispositivo puede soportar, con lo que afecta la eficiencia que puede obtenerse en procesos no lineales. En primer lugar se describe el estudio comparativo de los umbrales de daño óptico en diversas guías, puesto que éste aspecto no ha sido investigado suficientemente con anterioridad.

Para obtener una mayor comprensión del fenómeno del daño óptico, un mecanismo básico del mismo, el efecto fotovoltaico, fue investigado y también se describe en este capítulo. Entre los resultados obtenidos merece la pena citar el comportamiento súper lineal de la corriente fotovoltaica en algunas guías, así como su correlación con los datos de daño óptico y las implicaciones derivadas.

La segunda parte de este capítulo se dedica a un estudio más amplio del daño óptico en guía α, en las que se había mostrado que poseían altos coeficientes no lineales y alta resistencia al daño. Se exploran y caracterizan nuevas configuraciones de particular interés para aplicaciones, como guías fabricadas en sustratos en corte z, guías fabricadas sobre PPLN y guías acanaladas.

El último capítulo de esta tesis, *7. Polarización Periódica con Campo Eléctrico* se describe y discute cómo se ha realizado la polarización periódica en guías PE en fase α. Se eligió trabajar en estas guías, porque, como ya se ha mencionado, son muy adecuadas para dispositivos no lineales y porque, al fabricarse en nuestro laboratorio, eran más accesibles para la realización del trabajo. Se muestra cómo se han llegado a obtener estructuras de dominios con períodos tan pequeños como $5\,\mu\mathrm{m}$, que es límite más pequeño generalmente aceptado para esta técnica en volumen y con $LiNbO_3$ congruente. Al contrario que en trabajos anteriores con guías por intercambio protónico, la polarización con campo eléctrico se llevó a cabo tras la fabricación de las guías. Las guías ópticas así polarizadas periódicamente muestran una gran calidad en sus dominios, incluso para los más pequeños de $5\,\mu\mathrm{m}$. Además, las propiedades ópticas de las guías no se han visto afectadas por la inversión de dominios.

Part I

Introduction

Introduction:

Chapter 1
Main properties of Lithium Niobate

Main properties of Lithium Niobate

In this chapter, the material which has been the basis of this thesis work, will be introduced: Lithium Niobate. This crystal has been thoroughly studied since it was first synthesized by B. T. Matthias and J. P. Remeika [143] in 1949. It is a quite hard solid (5 in the Mohr scale), with a fusion temperature of $1253^{o}\,\mathrm{C}$. Its refractive index is relative high (~ 2.3 in the visible spectra). Depending on its oxidation state, impurities content and their concentration, it presents a wide range of colors, from bright black when it is completely reduced to transparent when it is totally oxidized, going through brown and yellow in between.

Nowadays there is an intense research effort centered in $LiNbO_3$ throughout the world. This interest is mainly due to its excellent optical properties, which makes $LiNbO_3$ suitable for a great variety of applications, such as devices of superficial acoustic waves (SAW) [129, 185], commutators, multiplexors, filters [155], electrooptic modulators [214] and holographic storage devices [39].

Throughout this chapter, a brief review of the updated knowledge about $LiNbO_3$ properties will be made, as well as the fabrication method and the crystal defects present in the material.

1.1 Structure

One of the most remarkable features of $LiNbO_3$ is that it is a ferroelectric material at room temperature (R. T.). It has a Curie temperature T_c between 1050 and 1200º C, depending on the crystal stoichiometry, i.e. [Li]/[Nb] ratio [34]. $LiNbO_3$ structure is shown in figure 1.1 over and below T_c. For temperatures over T_c, the crystal structure is a kind of distorted perovskite, composed of oxygen octahedra with the Li^+ atoms in an oxygen layer, and, in the center of one out of three octahedron, a Nb^{5+} atom. This is called the *paraelectric* phase, and corresponds to the symmetry group $3m(D_{3d})$ and to the spatial (trigonal) R$3c$.

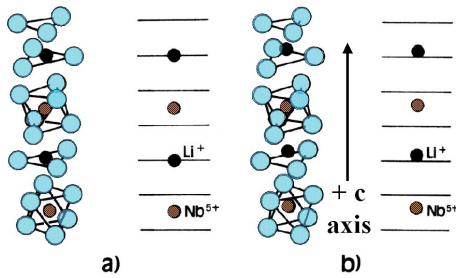

Figure 1.1: Crystalline structure of $LiNbO_3$: (a) paraelectric phase, (b) ferroelectric phase. White spheres represent oxygen atoms [218].

Below T_c the structure changes and it is called the *ferroelectric phase*: the thermal contraction pushes the Li^+ out of the oxygen plane and into one of the free octahedron. As a consequence, the Nb^{5+} are displaced in the same direction. On account of that, a spontaneous polarization of the crystal takes place and the symmetry is also changed to the punctual symmetry group $3m$ (C_{3v}) and the spatial R$\bar{3}$c [218]. In figure 1.2, the symmetry of a z-cut $LiNbO_3$ crystal is shown by means of a Rutherford Backscattering Spectrometry in channeling configuration (RBS/c) [211][1]

[1]This results were measured at the CMAM by Andrés Redondo-Cubero. The

The polarization direction determines the **c** axis of the crystal. The positive sense direction is defined as that where the displacement of the ions has taken place. It can be fixed during the crystal growth [29] or after it. In the second case, there are multiple possibilities: to apply an electric field near T_c [159, 209], to irradiate it with an electron beam [97] or, as it has been used in this work, to apply high electric fields near room temperature [62].

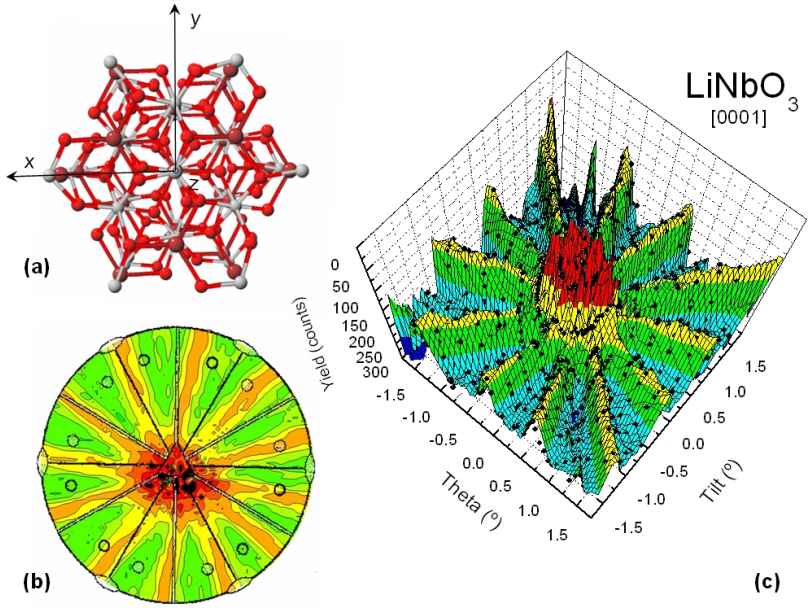

Figure 1.2: (a) Crystal structure of $LiNbO_3$ oriented along the **c** axis [0001]. (b) Comparison between the stereographic projection of a theoretical 3m(C_{3v}) lattice [173] and the actual experimental data. (c) Angular scan centered in the [0001] channel. Solid points represent the experimental data. The yield axis is inverted for a better view of the dip.

This structure makes $LiNbO_3$ an uniaxial crystal, where the refractive

experiment was performed with $3.5\,\mathrm{MeV}$ He^+ ions and minimum yield appears along the symmetry directions of the lattice.

indexes in **x** and **y** directions are equal and referred to as the ordinary index n_o of $LiNbO_3$, but different to that of **z**, called extraordinary index n_e. Spontaneous polarization of $LiNbO_3$ in the ferroelectric phase and its hyper-polarization are the origin of most of its interesting optical properties.

1.2 $LiNbO_3$ growth

1.2.1 Czochralski technique

Since 1965, the Czochralski method [64, 158, 59] has been the most employed growing technique for homogeneous, reproducible and rather bulky $LiNbO_3$ crystals, because of its versatility and simplicity [16]. This technique consists in the immersion of a single crystal seed in a melt with the components needed for the crystal. In the case of LN the melt usually comprises a mixture of Nb_2O_5 y Li_2CO_3, (or even powdery $LiNbO_3$). Following, the seed is slowly rotated and vertically pulled out in such a way that the crystal growth proceeds around the seed, and a cylindric single-crystal is developed. For $LiNbO_3$, the pulling and rotation rates are typically $1 - 5\,\mathrm{mm/h}$ and $10 - 60\,\mathrm{r.p.m}$, respectively. Once the crystal growth is finished, the cooling rate ($\sim 50^\circ\,\mathrm{C/h}$) must be strictly controlled to avoid fractures and cracks in the structure. Furthermore, the atmosphere in this last part of the growth is usually made in oxygen atmosphere, to prevent Li losses due to the high temperature [16, 193]. Nowadays, commercial crystals of 4 inches diameter and 50 mm thickness with a high homogeneity and good crystal properties are commercially available. In table 1.1 a set of parameters for $LiNbO_3$ provided by a commercial house.

As far as the stoichiometry of the crystal is concerned, $LiNbO_3$ crystals are usually grown in the congruent composition. In the phase

Crystal structure	Trigonal, space group R_{3c}
Cell parameters	a=$0,5148\,\mathrm{nm}$, c=$1,3863\,\mathrm{nm}$
Density	$4,64\,\mathrm{g/cm^3}$
Hardness	$5\,\mathrm{Mohr}$
Curie point	$1140°\,\mathrm{C}$
Melting point	$1250°\,\mathrm{C}$
Birefringence gradient	$10^{-5}\,\mathrm{cm^{-1}}$
Absorption coefficient	$0.1\,\mathrm{cm}$ at $1064\,\mathrm{nm}$
Dielectric constant	$\varepsilon_{11}^T/\varepsilon_0 = 85$ $\varepsilon_{33}^T/\varepsilon_0 = 29.5$
Thermal expansion coeff.	$\parallel$ a, $2.0x10^{-6}/\,\mathrm{K}$ at $25°\,\mathrm{C}$ $\parallel$ c, $2.2x10^{-6}/\,\mathrm{K}$ at $25°\,\mathrm{C}$
Transparence range	$420 - 5200\,\mathrm{nm}$
Optical homogeneity	$\sim 5x10^{-5}/\,\mathrm{cm}$
Refractive indices	$\mathrm{n}_e = 2.146$, $\mathrm{n}_o = 2.220$ at $1300\,\mathrm{nm}$ $\mathrm{n}_e = 2.156$, $\mathrm{n}_o = 2.232$ at $1064\,\mathrm{nm}$ $\mathrm{n}_e = 2.203$, $\mathrm{n}_o = 2.2286$ at $632.8\,\mathrm{nm}$
NLO coefficients	$\mathrm{d}_{33} = 34.4$ pm/V $\mathrm{d}_{31} = d_{15} = 5.95\,\mathrm{pm/V}$ $\mathrm{d}_{22} = 3.07\,\mathrm{pm/V}$
Electro-optic coefficients	$r_{33}^T = 32\,\mathrm{pm/V}, r_{33}^S = 31\,\mathrm{pm/V}$ $r_{31}^T = 10\,\mathrm{pm/V}, r_{31}^S = 8.6\,\mathrm{pm/V}$ $r_{22}^T = 6.8\,\mathrm{pm/V}, r_{22}^S = 3.4\,\mathrm{pm/V}$ $r_{51}^T = 32\,\mathrm{pm/V}, r_{51}^S = 28\,\mathrm{pm/V}$
Piezo-electric coefficients	$d_{31} = -0.91 \pm 0.08\,\mathrm{pm/V}$ $d_{33} = 8.1 \pm 0.2\,\mathrm{pm/V}$ $d_{22} = 20.9 \pm 0.1\,\mathrm{pm/V}$ $d_{51} = 70 \pm 3\,\mathrm{pm/V}$

Table 1.1: $LiNbO_3$ wafer parameters given by Photox. The piezo-electric coefficients and the r_{51} electrooptic coefficient have been taken from [218]

diagram of the Li_2O – Nb_2O_5 system (figure 1.3), there can be found a maximum in the solid-liquid curve corresponding to a concentration near the stoichiometric one (Li_2O 50%) but slightly different, that is 48.470% molar of Li_2O when the crystal is grown along the **z** axis and 48.490% if grown along the **x** axis [20]. The melt tends to crystallize at this concentration, known as *congruent*, where there is a deficiency of lithium with respect to the stoichiometric composition [59, 63]. Any other composition of the melt produces a variation on its composition while the development of the crystal growth. And this variation is transferred to the crystal composition itself, affecting its physical properties. Among the most perturbed characteristics by the [Li]/[Nb] are the Curie Temperature (T_c), [161, 92], birrefringency [92, 24, 191], the ultraviolet absorption edge [125], and the phase matching temperature for second harmonic generation [230]. As a matter of course, a great variety of measurement techniques have been developed to know the exact stoichiometry of the $LiNbO_3$ crystals [191, 125, 10].

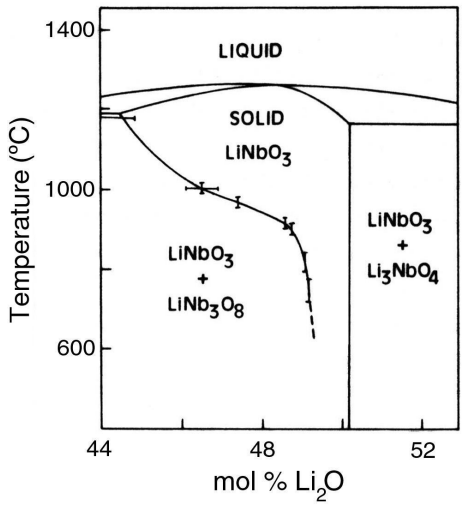

Figure 1.3: Phase diagram of Li_2O-Nb_2O_5 corresponding to $LiNbO_3$ formation [205].

Despite the natural trend of $LiNbO_3$ is the congruent composition, great efforts are made to obtain pure stoichiometric crystals (or quasi-stoichiometric). These processes are more difficult and several methods have been proposed, such as Czochralski growth with K_2O added to the melt [193, 140], the double crucible technique [119], and Vapor Transport Equilibrium (VTE) [35, 110].

1.2.2 Other crystal growth techniques for $LiNbO_3$

Apart from the Czochralski crystal growth technique, there are other methods also used for $LiNbO_3$, for example the Stepanov technique [85]. Most of them are used for thin layers, as molecular beam epitaxy (MBE) [31], liquid phase epitaxy (LPE) [225], laser ablation [212] or sol-gel technique [220]. Also fiber optics made of $LiNbO_3$ have been developed [234, 228].

1.2.3 Single domain crystals

The Czochralski growth of congruent $LiNbO_3$ crystals usually presents a random orientation of ferroelectric domains. To avoid it, there are several methods that, applied during the crystal growth (addition of MoO_3 or WO_3 to the melt [159]) or after it (application of an external field [29] over the coercive field of $LiNbO_3$, which is around $21\,\mathrm{kV/mm}$), result in an homogeneous single domain $LiNbO_3$ crystal. The commercial wafers are usually single domain, to avoid inhomogeneities in the properties of the $LiNbO_3$.

1.2.4 Periodically poled $LiNbO_3$

In recent years, there has been a special interest in controlled ferroelectric domain structures. Several techniques have been employed to obtain Periodically Poled Lithium Niobate (PPLN), Opposite Domain Lithium Niobate (ODLN)... (see figure 1.4) [27]. Two of these procedures, namely the off-center Czochralski method and the electric field periodic poling, were used in this thesis work and are described in the following sections (for more details about this techniques, see sections 4.3.1 and 4.3.2).

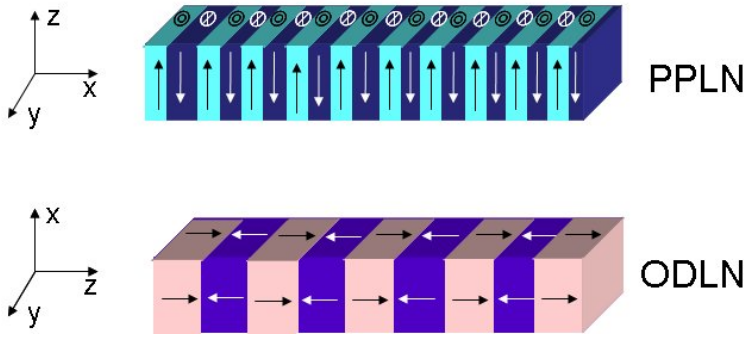

Figure 1.4: PPLN and ODLN crystals. The arrows indicate the direction of the polarization vector in each region.

Off-center Czochralski growth method

The first technique is a variation on the usual Czochralski growth method. It is called off-center Czochralski growth because it is exactly the same as the usual technique except that the crystal seed is not placed in the center of the oven, but in such a way that its rotational axis is displaced from the symmetry axis of the temperature field of the oven. That being so, the crystal growth temperature varies with the temperature gradients produced out of the central axis, because of the convection currents within the melt.

When the melt contains rare earth ions, such as Er, Nb or Yb, the P_s vectors of the different regions grown in the center of the crucible appear to be anti-parallel to those grown off the center axis [25, 8, 30]. Even though domain reversal can be successfully achieved with this technique, there are many variables that should be taken into account: the compositional nature of the impurity concentration [27, 26], the cooling effect on the periodic structure [28], the domain wall thickness [40] and other variables. These days several studies are trying to clarify these phenomena in order to improve this polarization technique.

Electric field periodic poling

The electric field periodic poling, in contrast with the above mentioned technique, is applied once the ferroelectric crystal has been grown, cut and polished. To create the PPLN structure, the spontaneous polarization of $LiNbO_3$ has to be reversed. To pole the samples periodically, most of the techniques involving electric field use periodic electrodes in one of the $+c$ or $-c$ faces of the sample and a planar electrode in the other one to apply an electric field along the **c**-axis of the crystal (other possibilities, such as using 82° z-cut substrates have also been studied [200]). In order to fabricate these electrodes with widths in the range of micrometers, photolithography, chemical pattering, laser ablation or other techniques are commonly used. Then, an electric field higher than the coercive field of the crystal ($21\,\mathrm{kV/mm}$ for congruent $LiNbO_3$ at R. T.) has to be applied to the photolithographically patterned electrodes [226]. Therefore, the samples (usually z-cut crystals of $0.5\,\mathrm{mm}$ width) are introduced in *poling chambers* [153, 130, 197], where both the structured and the non-structured faces can be independently contacted with liquid electrodes, and the high field can be applied.

Nowadays, a lot of studies are devoted to find the best way of obtaining

homogeneous periodically poled structures by different means: chemically patterned electrodes [17, 93], MgO doped lithium niobate, which has a lower coercive field than undoped $LiNbO_3$ [149, 157], illumination with ultraviolet light [152], different voltage pulses to perform backswithching [19] and many other variations. Also a lot of research is being carried out to clarify the kinetics of the whole polarization reversal process [195, 151].

1.3 Defects in $LiNbO_3$

In $LiNbO_3$ one of the key factors of its properties are the defects present in the crystal, as occurs for most materials. These impurities not only modify the crystal, but are also responsible of phenomena – such as the photorefractive effect. Most of these defects appear as a consequence of the crystal growth technique, but they can be also introduced on purpose to modify certain properties of the material in a controlled way.

The most used criterion used to classify the defects of $LiNbO_3$ is to distinguish between *intrinsic* and *extrinsic* defects, which will be briefly described in this section.

1.3.1 Intrinsic defects

It was mentioned before in section 1.2.1 that for $LiNbO_3$, the preferred composition is the congruent one. This differs slightly from the stoichiometric one, having a deficit of Li, and the crystal needs some charge compensation mechanism. The *intrinsic* defects are those which appear during the growth of the crystal to compensate this lack of Li.

The study of these defects has produced different points of view with respect to their origin, such as niobium vacancies [172], oxygen vacancies

[206] or lithium vacancies [72]. From the experimental perspective, a lot of measurements have been made to clarify this point: nuclear magnetic resonance (NMR) [32], X-ray diffraction [237]... Recently, due to a simulation which took into account the three models mentioned above, carried out by Safaryan *et al* [186], the Li vacancies model was reported to be the most plausible one. This model considers that some of the Nb ions in excess ($\lesssim$ 6% [Nb] [123]) occupy lithium vacancies, being this niobium in lithium places the so-called *antisites* (Nb_{Li}^{5+}). There has also been detected the presence of small polarons which derivate from electrons trapped by this antisites, which form Nb_{Li}^{4+} ($\sim$ 2% [Nb]) [215, 108, 139]. Nevertheless, being this model the one which shows better accordance with the experimental data [237, 223, 103], there are still studies devoted to clarifying if this is the correct description of the intrinsic defects in $LiNbO_3$[171].

1.3.2 Extrinsic defects

The presence of extrinsic defects is due to the addition of defects due to the crystal growth technique (due to impurities present on the melt, or in the atmosphere) or introduced after it. Ions such as Fe, H and others always appear in $LiNbO_3$ crystals grown with the Czochralski method, and their presence is inevitable [182]. Sometimes they are introduced on purpose to obtain doped $LiNbO_3$ in a controlled way. Nowadays high quality Fe, Cu, Zn, Mg or rare earth $LiNbO_3$ doped crystals can be obtained [102, 174, 51, 231, 11]. These extrinsic defects affect the optical properties of $LiNbO_3$ [107, 232], even in quantities as low as a few ppm. Some examples are Mg and Zn doping, use to reduce optical damage [15], Fe and Cu to enhance the photorefractive effect and many others.

1.3.3 Hydrogen

Among all the impurities that can be found in $LiNbO_3$, hydrogen has a relevant importance for this work, because most of the waveguides used in the experiments were formed by the inclusion of hydrogen atoms in a layer of the crystal.

Hydrogen ions can be always found in $LiNbO_3$ in concentrations of $\sim 10^{19}\,\mathrm{cm}^{-3}$. Their addition to the composition of the crystal happens during its growth, due to the presence of H in the melt, in the atmosphere or both. It is possible to diminish their presence in already grown $LiNbO_3$; therefore thermal treatments over $400^\circ\,\mathrm{C}$ in vacuum have to be done, which produce out-diffusion of H in the form H_2O and reduces the crystal [48]. Following, it has to be oxidized in pure O_2 atmosphere at temperatures of $900^\circ\,\mathrm{C}$. It is also possible to increase the concentration of hydrogen with thermal treatments over $400^\circ\,\mathrm{C}$ with pressures of $1 - 30\,\mathrm{bar}$ in hydrogen or water atmosphere, obtaining values of $\sim 10^{20}\,\mathrm{cm}^{-3}$ [33].

As in other materials such as SiO_2 or TiO_2, the H ion is bonded to the oxygen, in the form of OH^- [124]. These bonds are placed in planes normal to the **c** axis, along O–O directions. In figure 1.5 the possible positions of H are shown.

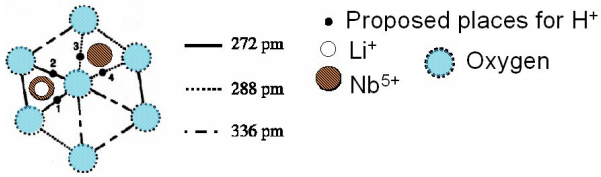

Figure 1.5: Hydrogen in $LiNbO_3$ [48].

Each of those positions produce an optical absorption band in the infrared. In congruent $LiNbO_3$, these bands are widened and overlap

with each other, due to the distortion caused by the Nb_{Li}, but they can be measured to obtain an idea of the hydrogen concentration.

Higher concentrations of H produce changes in the structure of the crystal which in turn modify properties such as the refractive index or the temperature for quasi-phase-matching [48]. To take advantages of this changes, different techniques have been developed to introduce massive H ions in the crystal: ion implantation ([H]$\sim 10^{20}\,\mathrm{cm}^{-3}$ [76]) or proton exchange in an acid melt ([H]$\sim 10^{22}\,\mathrm{cm}^{-3}$ [105]). Both techniques produce the highest concentrations of H that can be achieved in $LiNbO_3$, but only in a few microns depth. Consequently, they can not be used to study bulk samples. Even though, these amounts of H produce changes in the refractive index, which make these techniques very important ways of obtaining waveguide layers in $LiNbO_3$, as it will be shown in section 4.1.1.

1.4 $LiNbO_3$ Properties

Pure ant totally oxidized $LiNbO_3$ is colorless and transparent. For normal incidence, it has a reflectivity of 15% in the visible, and a transmittancy of almost 100%, from $5.5\,\mu\mathrm{m}$ in the infrared to the ultraviolet absorption edge, at $330\,\mathrm{nm}$ [158]. As it was already mentioned in section 1.2.1, this absorption edge is very sensitive to the [Li]/[Nb] rate in the crystal [183, 125], being displaced $0.1\,\mathrm{eV}$ to higher energies for stoichiometric crystals. The reason is that, as in other perovskite compounds, the band structure is characterized by the NbO_6 octahedra [69, 96].

1.4.1 Refractive index

$LiNbO_3$ is a uniaxial material, with a negative birrefringency of around $n_e - n_o \sim -0.08$ [218]. There have been several studies on the actual refractive indices of $LiNbO_3$, which show great dispersion, to obtain a general Sellmeier equation for different stoichiometries, wavelenghts and impurities. An example of this could be the Sellmeier equation obtained by U. Schlarb and K. Betzler [190]:

$$n_i^2 = \frac{50 + c_{Li}}{100} \times \frac{A_{0,i}}{(\lambda_{0,i} + \mu_{0,i}[f(T) - f(T_0)])^{-2} - \lambda^{-2}} + \\ + \frac{50 - c_{Li}}{100} \times \frac{A_{1,i}}{(\lambda_{1,i} + \mu_{1,i}[f(T) - f(T_0)])^{-2} - \lambda^{-2}} + A_{UV} - A_{IR,i}\lambda^2 \tag{1.1}$$

with

$$f(T) = (T + 273)^2 + \alpha \left[\coth\left(\frac{\tilde{T}}{T + 273} \right) - 1 \right] \tag{1.2}$$

Where $i = e, o$ marks the polarization, c_{Li} the %molar Li_2O concentration, λ the wavelength in nm, T the temperature in $^\circ\mathrm{C}$ and $T_0 = 25.4^\circ\mathrm{C}$. All the others are fitting parameters. In this equation, the first term is related to the NbO_6 structure, and the second to the Nb^{5+} in Li^+ places, i.e. *antisties*. Both terms are temperature dependent, given by equation 1.2. The third term deals with the contribution of the plasmons in the far UV ($13 - 25.5eV$) [141] and is independent of the polarization [222]. Finally, the last term takes the infrared absorption into account.

As the study of the refractive index in $LiNbO_3$ is basically empirical and the adjustment of the parameters depends so strongly on the nature

of each crystal, a wide variety of Sellmeier equations for different stoichiometries and wavelength ranges can be found in literature. For example, in reference [224], different Sellmeier equations are presented for congruent, stoichiometric and doped $LiNbO_3$ at different wavelength ranges (visible, mid-IR, IR and even microwaves). Depending on the crystal stoichiometry and the wavelength range one wants to work with, the ordinary and extraordinary refractive indices should be calculated with the appropriate Sellemier equation.,

1.4.2 Electro-optic effect

A change in the refractive index of a material due to the presence of an electric field is known as electro-optic effect [3]. In its ferroelectric phase, $LiNbO_3$ presents a index change proportional to the applied electric field, which is known as the *Pockels effect*. This proportionality varies slightly with the crystal composition [68]. It can be described as a third order tensor (r_{ijk}) as follows:

$$\Delta \left(1/n^2\right)_{ij} = \sum_k r_{ijk} E_k \,. \tag{1.3}$$

Because of the 3m punctual symmetry, only four of the components of the Pockels matrix (equation 1.4) are independent, r_{13},r_{51}, r_{22} and r_{33}, according to the contracted notation for the electrooptic tensor [218]. Then, the contracted $(r_{ij}$ tensor writes in terms of this components as:

$$(r_{ij}) = \begin{pmatrix} 0 & -r_{22} & r_{13} \\ 0 & r_{22} & r_{13} \\ 0 & 0 & r_{33} \\ 0 & r_{51} & 0 \\ r_{51} & 0 & 0 \\ -r_{22} & 0 & 0 \end{pmatrix}. \tag{1.4}$$

The effective values of these coefficients are very high (see table 1.1) and that makes $LiNbO_3$ one of the most employed materials for electro-optic devices.

For those applications requiring elevated electric fields, the second order term of the electro-optic interaction, *Kerr* becomes important, and the index change is now expressed as:

$$\Delta \left(1/n^2\right)_{ij} = \sum_k r_{ijk} E_k + \sum_{kl} S_{ijkl} E_k E_l \tag{1.5}$$

where S_{ijkl} (S_{ij} are the quadratic electro-optic coefficients or Kerr coefficients. In most experiments, this term is too low compared to the linear one ($|S_{13}| \leq 2.3 \times 10^{-21}$ m^2/V^2, [138]).

1.4.3 Electric properties

The electric behaviour of $LiNbO_3$ is strongly related to the composition and defects of the crystal, both intrinsic and extrinsic (as can be seen in section 2.3). Therefore, from the study of the **electric conductivity**, information from the structure and transport mechanisms can be obtained, also related with the photovoltaic and photorefractive effects already mentioned. At room-temperature, the electric conductivity for congruent

$LiNbO_3$ is $\sim 10^{-18}\,\mathrm{ohm/cm}$ [201].

Through a variety of experiments, different transport mechanisms have been investigated. For temperatures below 400 K, the hopping model has been proposed, that is, the electrons or small polarons *jump* between neighbour positions of the crystal lattice [23, 56]. Between 80 and $600^{\circ}\,\mathrm{C}$ the high proton mobility is supposed responsible for the conductivity [48].

Another phenomenon that can be found in $LiNbO_3$ is the **piezoelectric effect**, that is, if the crystal is deformed, an electric field appears, and vice versa. It can be expressed as:

$$P_i = \delta_{ijk}\sigma_{jk}; \epsilon_{jk} = \delta_{ijk}E_i \tag{1.6}$$

Where δ_{ijk} are the piezo-electric coefficients (see table 1.1) and σ_{jk} the stress tensor. And if an electric field with E_i components is applied, an stress ϵ_{jk} will be generated. This effect depends on the stoichiometry of the crystal, decreasing with the increase of lithium concentration [92]. This effect has to be taken into account in the design of electro-optic devices. For other applications, such as piezoelectric mirrors and components [156] or surface acoustic waves (SAW) devices [129], $LiNbO_3$ piezo-electricity is the key of their functionalism.

But those are not the only electric phenomena which appear in $LiNbO_3$. Also a variation in the temperature generates an electric field. This is known as the **pyroelectric effect** [189, 188] and is a result of the dependence of the spontaneous polarization with temperature. If the crystal is heated, negative charge accumulates in its **+c** face. The dependence of this effect on the stoichiometry of the crystal is the same as in the case of the *piezo-electric effect* [92]. For the congruent composition at R.T., the relation between the spontaneous polarization change and the change in the temperature is given by [18]:

$$p_3 \equiv \frac{\partial P_s}{\partial T} = -\left(6.4 \pm 0.6\right) \times 10^{-5} \frac{\mathrm{C}}{\mathrm{m}^2 K} \tag{1.7}$$

Chapter 2
Nonlinear optical properties of Lithium Niobate

Nonlinear optical properties of Lithium Niobate

Nonlinear media present several characteristics, such as a change of the refractive index with light intensity, the violation of the superposition principle, interaction of photons and the alteration of the light frequency as it travels throughout the material. The medium is changed by the presence of the optical field and this transformation reciprocally modifies the optical field.

$LiNbO_3$ is one of these nonlinear media, and this chapter is devoted to briefly describe the main features of nonlinear phenomena in this material, particularly those connected to the results of this thesis work. Firstly, I will speak about frequency conversion. Then, the photovoltaic effect will be studied in order to introduce other important nonlinear effect, that is, the photorefractive effect. One of the consequences of this photorefractive effect, namely the optical damage effect, will be also considered at the end of the chapter.

2.1 Non linear optical properties (Frequency conversion and SHG)

The interaction between the medium and light is described by the relation between the polarization density vector and the electric field vector. If the relation is nonlinear, then the medium is said to be nonlinear too and the polarization density is written as:

$$P_i = \sum_j \chi_{ij} E_i + \sum_{jk} \chi^{(2)}_{ijk} E_j E_k + \sum_{jkl} \chi^{(3)}_{ijkl} E_j E_k E_l + \dots \qquad (2.1)$$

being the first term the linear response, $\chi^{(2)}_{ijk}$ the second order nonlinear susceptibility, $\chi^{(3)}_{ijkl}$ the third order one and so on. Some interesting applications associated with the second order term are the interaction of two monochromatic waves that gives rise to a third one with a frequency equal to the sum or difference of the original frequencies (*frequency conversion*), the amplification of a wave thanks to other two (*parametric amplification*) and frequency doubling of a monochromatic wave (*second harmonic generation*, SHG). In the case of the third order term, it gives rise to *third harmonic generation, self-focusing, four wave mixing* ... These nonlinear phenomena are treated in detail in references [37, 187].

$LiNbO_3$ is a noncentrosymmetric material that presents a high $\chi^{(2)}_{ijk}$, and therefore, a high second order nonlinear response. The terms of v which are different from zero are indicated in contracted notation [218] in equation 2.2.

$$(\chi_{ij}) = \begin{pmatrix} 0 & 0 & 0 & 0 & \chi_{51} & -\chi_{22} \\ -\chi_{22} & \chi_{22} & 0 & \chi_{51} & 0 & 0 \\ \chi_{13} & \chi_{13} & \chi_{33} & 0 & 0 & 0 \end{pmatrix} \tag{2.2}$$

Frequently, in experimental works, the second order nonlinear coefficient, $d_{ij}^{(2)}$ is used instead of $\chi_{ij}^{(2)}$. The equivalence between them is simply $d_{ijkl}^{(2)} \equiv \frac{1}{2}\chi_{ijkl}^{(2)}$. The values of the non zero components of this tensor for commercial $LiNbO_3$ can be found in table 1.1. The magnitude of these coefficients are high enough to permit the generation of second harmonic light with different methods: phase-matching, [73, 114], quasi-phase-matching in periodically polarized crystals [111, 75]...

2.1.1 Fundamentals of frequency conversion

Let us consider that an electric field with two harmonic components at frequencies ω_1 and ω_2 reach the nonlinear material. The incident field can be written as

$$E(t) = E(\omega_1)exp(i\omega_1 t) + E(\omega_2)exp(i\omega_2 t) \tag{2.3}$$

Then, if one takes the second term of equation 2.1:

$$P_{ij}^{NL} = \chi^2 \; E_{ij}(t)^2 \tag{2.4}$$

and the above mentioned electric field is substituted, one gets

$$P_{ij}^{NL} = \chi^{(2)} E_1^2 e^{-2i\omega_1 t} + \chi^{(2)} E_2^2 e^{-2i\omega_2 t} + \chi^{(2)} 2E_1 E_2 e^{-(\omega_1+\omega_2)t}$$

$$+ \chi^{(2)} 2E_1 E_2^* e^{-i(\omega_1-\omega_2)t} + c.c + 2\chi^{(2)} \left[E_1 E_1^* + E_2 E_2^*\right] \tag{2.5}$$

From this equation, one can take the five components of the polarization P_{NL}, which have different frequencies, and one obtains the frequency conversion terms, that is, sum frequency generation $\omega_+ = \omega_1 + \omega_2$,, difference frequency generation $\omega_- = \omega_1 - \omega_2$, second harmonic generation $2\omega_1, 2\omega_2$, and optical rectification 0:

$$P_{NL}(0) = d\left[|E(\omega_1)|^2 + |E(\omega_2)|^2\right] \tag{2.6}$$
$$P_{NL}(2\omega_1) = dE(\omega_1)E(\omega_2) \tag{2.7}$$
$$P_{NL}(2\omega_2) = dE(\omega_2)E(\omega_2) \tag{2.8}$$
$$P_{NL}(2\omega_+) = 2dE(\omega_1)E(\omega_2) \tag{2.9}$$
$$P_{NL}(2\omega_-) = 2dE(\omega_1)E^*(\omega_2) \tag{2.10}$$

These equations show how in a nonlinear media, two optical waves of different frequencies can be used to obtain a third optical wave. Even though these two waves generate a set of polarization densities at five different frequencies, it does not mean that all of these optical waves are produced. There is an additional condition, namely *phase matching* that has to be fulfill. To understand this new requisite, one can consider this wave mixing as a photon interaction process. Then, in a three wave mixing process, three photons will be involved: one photon of frequency ω_1 and wavevector $\mathbf{k}_1$ is combined with another photon of frequency ω_2 and wavevector $\mathbf{k}_2$ to produce a third photon of frequency ω_3 and wavevector $\mathbf{k}_3$, as shown in figure 2.1.

The energy exchange among the interacting waves must obey the conservation of energy law, that is

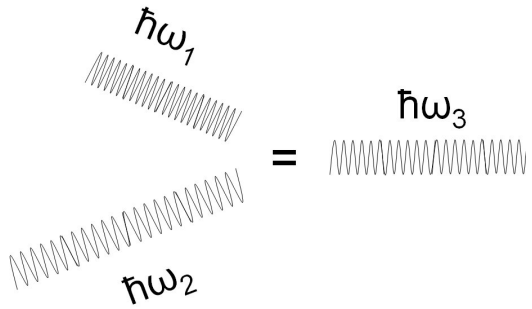

Figure 2.1: Three photons combining in a nonlinear medium

$$\hbar\omega_1 + \hbar\omega_2 = \hbar\omega_3 \tag{2.11}$$

Also, for an efficient nonlinear interaction to take place, the momentum has to be conserved. This condition is usually called *phase-matching*, and, as the momentum of a photon can be written as $\hbar\mathbf{k}$, this requirement takes the form

$$\hbar\vec{k}_1 + \hbar\vec{k}_2 = \hbar\vec{k}_3 \tag{2.12}$$

2.1.2 Second Harmonic Generation (SHG)

To illustrate with one very significant example the main physics of frequency conversion phenomena, let us consider in detail the second harmonic generation (SHG). In this case, only one incident harmonic electric field of frequency ω

$$E(t) = E(\omega)exp(i\omega t) \tag{2.13}$$

(where $\omega = 2\ \pi\ c/\lambda$ is the frequency and $E(\omega)$ is the amplitude)

enters the material. Then, if one substitutes this field in 2.4, the nonlinear polarization density becomes

$$P_{NL}(t) = 2dE(t)^2 = dE(\omega)E^*(\omega) + dE(\omega)E(\omega)exp(i2\omega t) \qquad (2.14)$$

This means that the scattered optical field has a component at the second harmonic of the incident one, with a frequency 2ω (and a correspondent wavelength $\lambda/2$). This is called *second harmonic generation*

However, the main problem for the efficient generation is the phase mismatch between the incident wave and the second harmonic wave. In this case, it is easier to figure the effect as a second order polarization wave ($P^{2\omega} = dE(\omega)E(\omega)$) created by the fundamental wave that travels along with it, with a velocity determined by the refractive index n_ω. The velocity of the second harmonic generated wavelength is determined by $n_{2\omega}$, which in the most general case, is different from n_ω. As a consequence, light generated at different points of the material has a phase mismatch that produces a destructive superposition after a certain propagation length. Subsequently, the intensity $I^{2\omega}$ has a sinusoidal dependence with the distance, as can be seen in figure 2.2.a.

This phase mismatch can be completely removed if $n_\omega = n_{2\omega}$, which is called the *birefringent phase matching*. This condition can be sometimes fulfilled in birefringent materials, where a direction can be found in which the ordinary index for one of the frequencies is the same as the extraordinary index for the other one. Then, the efficiency presents a quadratic dependence with the distance (see figure 2.2.b). The main drawback of the birrefringent phase matching is that the fundamental and second harmonic beams do not usually propagate parallel to each

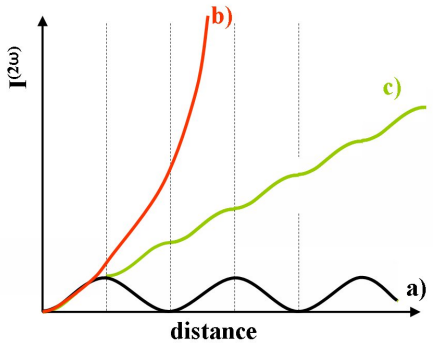

Figure 2.2: Effect of the phse matching on the intensity of second harmonic light generated in the crystal with the distance of the nonlinear crystal. a) non-phase matched interaction b) first-order QPM (when the spontaneous polarization is reversed each coherence length) c) perfect phase matching in a single-domain crystal

other. This is called *walk-off*, and reverts in the loss of the superposition between them, affecting also the efficiency of second harmonic generation, reaching a saturation value at a certain point.

2.1.3 Quasi-phase matching

In order to obtain the best results for the second harmonic generation, the nonlinear materials have to fulfill basically three requirements: transparency for both wavelengths, fundamental and doubled, relatively high nonlinear coefficients and a high optical damage threshold. As it was showed in the table of page 11, the nonlinear coefficient d_{33} of $LiNbO_3$ is $34.4\,\mathrm{pm/V}$ and its transparency range covers a really wide part of the spectrum, which makes $LiNbO_3$ a very promising material for nonlinear applications.

The main problem that has to be solved in order to obtain efficient second harmonic generation in nonlinear materials is the maintenance of the relative phase between the fundamental and the generated waves as

long as possible. Curiously, it was at the beginning of nonlinear optics and even before the birefringent phase matching had been proposed, when the *quasi-phase matching* method was conceived. Two independent groups, Bloembergen *et al.* [12] and Franken *et al.* [79] proposed the modulation of the nonlinear coefficient using a periodically structured nonlinear medium to correct the relative phase mismatch between both waves.

In the case of $LiNbO_3$, this structure consists on the periodical inversion of the nonlinear coefficient, i.e., the fabrication of periodical ferroelectric domains (already discussed in section 1.2.4). To maximize the efficiency of the second harmonic generation, the nonlinear coefficient has to be reversed each time the change of the relative phase between both waves becomes π. This distance is called the coherence length for the fundamental wavelength (λ), and can be written as:

$$l_c = \frac{\lambda}{4(n_{2\omega} - n_{\omega})} \tag{2.15}$$

When the structure periodicity is that of $2l_c$ the efficiency obtained is showed in figure 2.2.c, and it is called called *first order quasi phase matching* structure. Lower efficiencies can be obtained if the periodicity of the domain structure corresponds to a multiple of this distance, that is $2ml_c$, being m an integer. Even though these higher order quasi phase matching structures do not achieve the highest possible efficiency, the second harmonic power generated grows with the distance of interaction in the nonlinear crystal.

For more details on the quasi phase matching, a comprehensive description of this method and theory can be found in a review by Fejer *et al* [75]. **[*comentar importancia QPM en la actualidad*]**

2.2 Photovoltaic effect

This effect was discovered by A. M. Glass, D. von der Line and T.J. Negran in 1974 [89]. They observed that in a $LiNbO_3$ crystal under illumination, if **+c** and **-c** faces were short-cut, appeared an electric current (j_{ph}), which was proportional to the light intensity (I) and to the absorption coefficient of the crystal (α).

$$j_{ph} = \kappa \alpha I \tag{2.16}$$

being κ the corresponding proportional coefficient, known as *Glass constant*. More recently, and in order to get a clearer picture of the material parameters involved in this phenomena, Carrascosa *et al.* proposed a more specific expression that will be used in this work [58], which is

$$j_{ph} = eL_{pv}S_{ph}I[Fe^{2+}] \tag{2.17}$$

where e is the value of the electron charge, L_{pv} is the effective photovoltaic transport length, S_{ph} the photoionisation cross section, I the photon flux and $[Fe^{2+}]$ the donor concentration.

The photovoltaic effect is present in some ferroelectric materials and is a consequence of the anisotropy of the crystal lattice, which produces an asymmetric potential and a directional excitation of the photoelectrons (see figure 2.3). This direction, in the case of uniaxial crystals ($LiNbO_3$ for instance) is essentially along the **c** polar axis.

However,photovoltaic currents in normal directions to **c** have also been measured [80, 77], although they are very small. These measurements point out the tensorial nature of the photovoltaic effect, because equation 2.16 should be actually written as

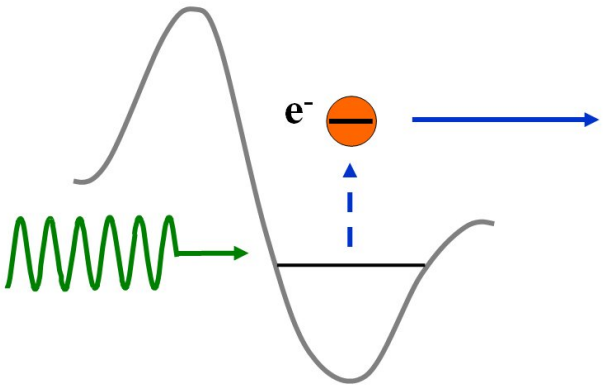

Figure 2.3: Scheme of the potential well of $LiNbO_3$. When an electron is excited, there is a higher probability that it goes in one direction rahter than in the other, due to the asymmetry of the well.

$$j_{ph,i} = \alpha \sum_{j,k} \kappa_{ijk} E_j E_k^* \tag{2.18}$$

If this tensor is written in the contracted way, only 4 elements are independent, which are κ_{31}, κ_{33}, κ_{22} y κ_{15}. The values of this coefficients for different doped $LiNbO_3$ crystals can be found in references [80, 77].

Finally, it is worthwhile mentioning that in bulk $LiNbO_3$ at high light intensities, there is a second center that contributes to the photovoltaic current, and the linear dependence with the intensity I of equation 2.17 is no longer valid [115, 198]. This second active center in $LiNbO_3$ is usually identified as the antisites, $Nb_{Li}^{4+/5+}$, always present in congruent $LiNbO_3$.

2.3 Photorefractive effect

The photorefractive effect was discovered by Ashkin *et al.* in 1966 [13] in $LiNbO_3$ and $LiTaO_3$. They detected that, when the crystal was illuminated with a high intensity laser beam, it was expanded along the **c** direction. This nonlinear optical effect is due to the variation of refractive index produced under illumination in the material.

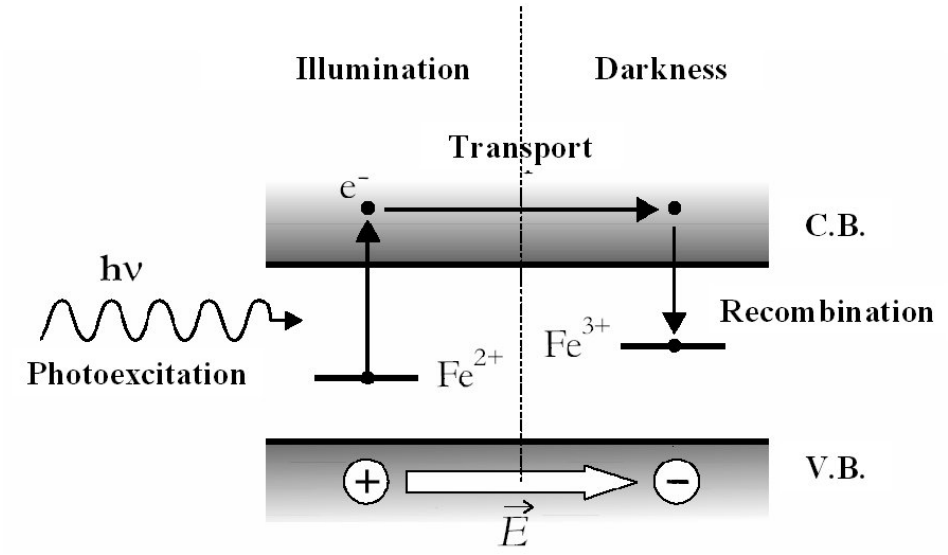

Figure 2.4: Scheme of the photorefractive effect mechanisms in $LiNbO_3$.

To understand this effect, one has to consider different processes that occur under illumination: photogeneration, transport, recombination, space charge distribution, electric field generation (indicated in figure 2.5)[1] and finally, refractive index change. In photorefractive material under illumination, free charge carriers (which could be electrons or holes, but in our case are always electrons) from impurity ions (Fe^{2+}) are photoexcited to the transport band. These electrons go away from the light

[1]This figure, as well as figure 2.5 are courtesy of Dr. G. de la Paliza

exposed region where they were generated. In this transport of carriers, there are three different contributions: diffusion, drift by an external electric field and photovoltaic transport. In the illuminated regions, the impurities left there become charged with the opposite sign (Fe^{3+}), and are fixed in their positions, whereas the electrons which have traveled to other places of the crystal without illumination can be trapped by ionized impurities, and this gives rise to an inhomogeneous space-charge distribution. As a consequence, an internal electric field is created, which in turn and via the electro-optic effect (*Pockels*), causes a change in the refractive index $\Delta n \sim 10^{-5}$.

If the illumination is not homogeneous, a refractive index pattern can be recorded (see figure 2.5). This pattern is semi-permanent, but can also be erased with homogeneous illumination, without affecting the structure of the crystal, as in other holographic materials. The photorefractive effect is therefore used to generate refractive index gratings, create holograms (filters, deflectors...) [155, 65] or store information [150, 2]. However, sometimes this refractive index change appears non intentionally in other linear or non linear applications of $LiNbO_3$ and generates beam distortions. In these cases, this undesirable effect is called optical damage, which will be briefly described in next section.

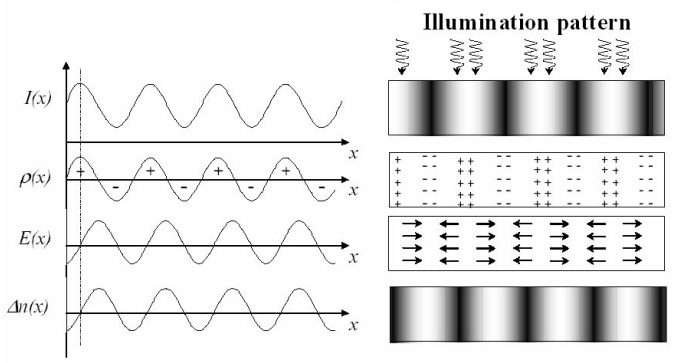

Figure 2.5: Creation of a Δn pattern from a sinusoidal illumination pattern, *I(x)*. ρ and *E* are the charge density and the electric field produced by this illumination.

2.4 Optical Damage

Optical Damage was first observed by Ashkin *et al.* [13] and from its study, the photorefractive effect was discovered (as it is described in the previous section, 2.3). Basically, optical damage is the distortion of the light beam due to the photorefractive effect.

Initially, it was explained as a defocussing produced directly by the decrease of refractive index due to the photorefractive effect. However, the characteristics of the distorted beam (spatial symmetry of the intensity profile, divergence degree and so on) are not always justified by this simple explanation. Therefore, the effect was thought to be also partially related to *photorefractive parametric amplification processes* (*fanning*). These processes are a consequence of the dispersion of the light beam produced in the inhomogeneities of the crystal (*scattering centers*). This scattered light interferes with the main beam and produces certain photorefractive gratings that cause light diffraction. Some of these gratings experience an increase in its modulation, also due to the scattered light, and as a result, more light is diffracted (*parametric amplification*). At high light

intensities, this beam distortion caused by this spurious gratings can become chaotic [4].

This effect is one of the main drawbacks of $LiNbO_3$ when medium or high light intensities have to be used, and in particular, in nonlinear optical applications, such as frequency conversion. Many efforts have been done in order to reduce the optical damage to avoid this problem, such as Mg or Zn doping [233, 207, 92]. However, a definitive solution has not been already found, and the field is still quite active nowadays, and new methods have been proposed, such as nearly complete oxidization of iron doped $LiNbO_3$ [74]. Up to now, only partial inhibition of optical damage has been achieved, and different measurement techniques have been developed to characterize this effect both in bulk and waveguide configurations, to determine the beam distortion [135], the power loss [90] and others.

The investigation of this phenomena in planar $LiNbO_3$ waveguides will be one of the main topics of this thesis work.

Chapter 3
Nonlineal optical waveguides

Nonlineal optical waveguides

Optical waveguides are structures where light can be confined in one or two directions in the order of several microns. When the objective is to take advantage of the nonlinear characteristics of a certain material, waveguide configuration, due to its extreme confinement, makes possible the performance of experiments at really high light intensities. In this chapter, waveguide parameters and characteristics will be described, along with the nonlinear properties that lead to frequency-conversion and, in particular, SHG in waveguide configuration.

3.1 Optical waveguides

3.1.1 Geometry

An optical waveguide consists on a dielectric medium with a higher refractive index than the surrounding media. In this medium, which may have different shapes, such as slabs (see figure 3.1.a), stripes (3.1.b) or even cylinders (as in optical fibers), light is transported without radiation into the surrounding media by virtue of total internal reflection. The inner medium is usually referred to as *core*, *guide* or, *film* in the case of planar waveguides, and the upper and lower media are called the *cover* or

cladding and *substrate* respectively.

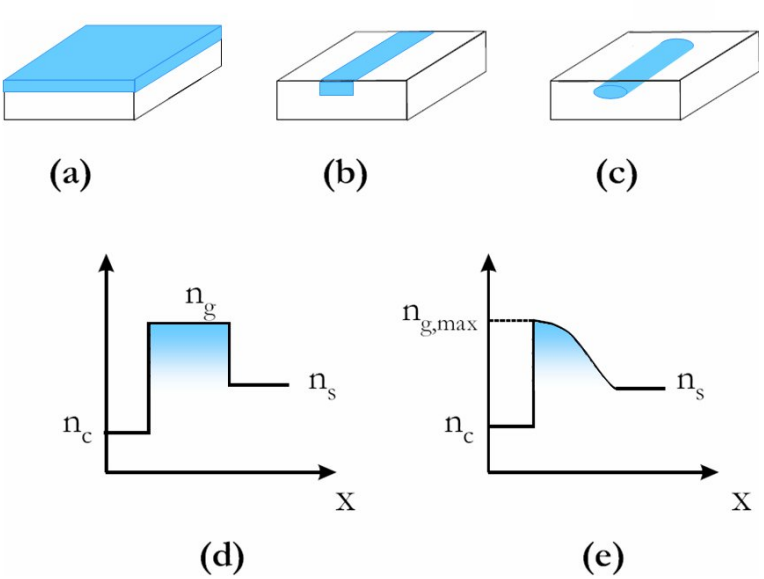

Figure 3.1: Different geometries of waveguide structures: (a) planar (b) channel (c) channel and embedded. (d) and (e) Different *index profiles* (d) step profile (d) smooth profile.

In the case of the waveguides used in this work, the substrate will always be $LiNbO_3$. As it was shown in the previous chapter, properties such as refractive indexes, spontaneous polarization and so on are different for different directions in the crystal. Therefore, x-cut or z-cut substrates (that is, the surface of the substrate normal to the **x** or **z** axis, respectively), were used in this work, allowing the study of different configurations. The cover will be air in all cases, because no buried or embedded waveguides have been used (see figure 3.1.c).

As far as the core is concerned, it will be fabricated on $LiNbO_3$ substrates by means of proton exchange, ion irradiation or metal in diffusion (a detailed description of the fabrication techniques can be found in sections 4.1.1, 4.1.3 and 4.1.2 respectively). These procedures induce an

increase in the refractive index and form the film or core of the waveguide. In the case of proton exchange, only the extraordinary index is increased and, as a result, only extraordinary polarized light can be guided. These methods, apart from inducing different index changes, give rise to different boundary geometries between the substrate and the film layer. In the case of ion irradiation, it is rather steep, and form what is called *step index profiles*. But metal in-diffused waveguides are characterized by a rather smooth index change between both media (see figure 3.1). In the case of proton exchanged waveguides, this feature can be customized depending on the concrete fabrication process.

3.1.2 Waveguide modes

From now on, the confinement dimensions will be considered that of photonic applications (of the order of microns). In this case the propagation of light along the waveguide is not simply explained by multiple reflections. Only those electromagnetic waves that after two reflections in the boundaries reproduce themselves, can be propagated along the waveguide. This is called the *constructive interaction* condition, and the waves that fulfill it, are the *modes of the waveguide*. These are characterized by the maintenance of their transverse distribution and polarization along their propagation in the waveguide. The accurate study of these modes has to be done with the aid of the electromagnetic theory.

A thorough theoretical analysis of optical waveguides can be found in most optics books [187, 47], but there are also more simple ways to have a quite correct and intuitive idea of the phenomena without going into too many details. With the aid of ray optics and a very elementary waveguide structure, the main properties of a waveguide can be presented. In figure 3.2 there is a planar waveguide with a film width of d and refractive indexes

for the substrate, cover and guide n_s, n_c, n_g, respectively. For the above mentioned condition of constructive interaction to be fulfilled, the phase change after two reflections for a waveguide mode has to be multiple of 2π.

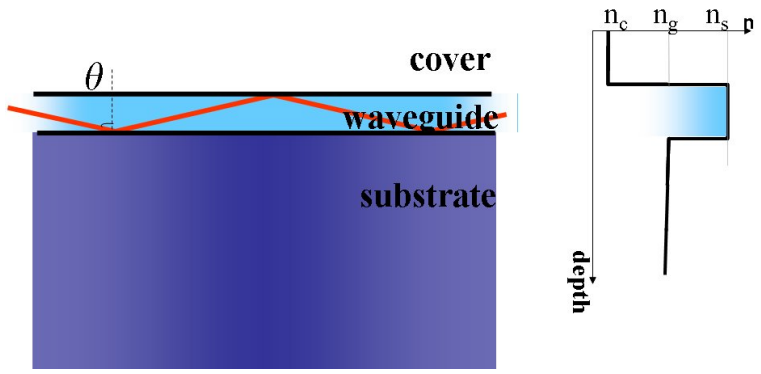

Figure 3.2: Index profile and schematic view of a step planar waveguide

The phase change of a ray traveling a distance d with a bounce angle, θ, is

$$\phi = k\, d \cos\theta = k_0\, n_g\, d \cos\theta$$

being k and k_0 the waveguide vector in the guiding medium and in vacuum ($k = \frac{2\pi}{\lambda}$), respectively. In addition, two other phase changes take place in the boudaries, $2\phi_c$ y $2\phi_s$, which depend on the polarization of the light. If all these contributions are taken into account, the self-consistency equation is obtained:

$$k_0\, n_g\, d \cos\theta_m + \phi_s\left(\theta_m\right) + \phi_c\left(\theta_m\right) = m\pi \tag{3.1}$$

where m is an integer called the mode order. This equation must be satisfied by all θ_m angles corresponding to guided modes. Other relevant

magnitudes of waveguides are:

- $\beta_m = k \sin\theta_m \Rightarrow$ Propagation constant
- $N_m = n_g \sin\theta_m \Rightarrow$ Effective refractive index

The number of modes is finite, because the angles θ_m of these modes must be higher than the critical angle for total internal reflection for both boundaries. That means,

$$\theta_m > \arcsin\frac{n_{c,s}}{n_g} \Leftrightarrow n_{c,s} < N_m < n_g \Leftrightarrow k_{c,s} < \beta_m < k_g \tag{3.2}$$

Therefore, in the most general case, a finite number of modes propagate along the waveguide. From these, the one with $m = 0$ is referred to as the *fundamental mode* and will be the chosen one for most of the experiments performed in this work. There are also waveguides where there is only one possible mode, which are called *monomode waveguides*.

3.1.3 Index profile characterization

The calculation of the index profile is important in the characterization of any waveguide. It includes two steps. First, the effective refractive indexes for the different propagation modes have to be obtained from experimental data. The experimental method used to determine them is the m-lines spectroscopy (described in section 4.2.1) Then, the refractive index profile can be inferred by means of numerical calculations.

Index profile calculation

The calculation of the refractive index profile is not an easy task. Once the propagation modes are known, one has to infer the actual index profile function that originates those modes. The answer is not unique, because different profiles could give the same modes. Therefore, it is necessary to have a former idea of the kind of profile expected in each case.

For step index profiles, the *reflection calculation method* method can be used. This method consists on the extrapolation of the self consistency equation 3.1 to calculate the refractive index of the waveguide, (n_g). Then, an approximate idea of the depth of the waveguide is obtained. If the waveguide is not exactly a step one, the obtained effective depth will be different for each mode, giving a rough idea of the actual depth corresponding to each of them.

For metal in diffused waveguides, soft proton exchanged and others, the most likely index profile shape is a rather smooth one, as it was mentioned in page 45. Furthermore, the self-consistency equation in the case of smooth boundary conditions takes the form of:

$$\int_{x_A}^{x_B} \sqrt{n^2(x) - N_m^2}\, dx = \left(m + \frac{1}{2}\right) \frac{\lambda}{2} \tag{3.3}$$

which has to be numerically solved. To cope with this problem, one can take advantage of the analogy between this problem and another similar one in quantum mechanics. That is, the modes are the roots of the system comprising guide, substrate and cover (the *wave equation*) and the boundary conditions of this system are analogous to that of quantum wells. Besides, the wave equation is equivalent to the *Schrödinger equation*, where the roots are discrete energy levels associated with a wave function. In this analogy, the potential becomes the refraction index profile

and the field distribution is changed into the wave function. As a result, the energy levels are changed to *effective refractive indexes* with discrete values, lower than the guiding layer but higher than the surrounding media.

Given that analogy, a variation of the WKB method (Wentzel, Kramers and Brillouin) [199] used to solve the Schrödinger equation, called the inverse WKB method [221, 99, 142] is used. Its use is limited to small refractive index variations, in the order of a wavelength, which is not always fulfilled, but the errors in the calculation are $\sim 10^{-4}$ for smooth profiles (for step profiles it is not recommended, because the errors are much higher).

Another numeric technique is the *multilayer approach* [60], where a proof profile is proposed and then it is divided in multiple layers (see figure 3.3) with constant refractive index values. Then, the Schrödinger equation for a step profile is solved for each layer. Continuity between the layers and boundary conditions are imposed. After this, the values of the theoretical modes are compared with the experimental ones, and the profile is modified to minimize the differences between them.

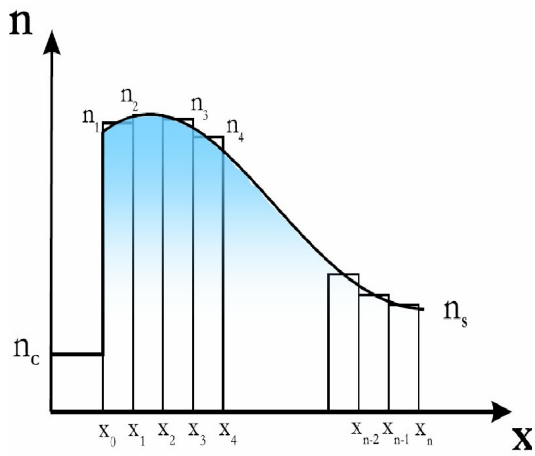

Figure 3.3: Index profile calculation ($n(x)$) with the multilayer approach.

In the case of single mode waveguides, where any index profile shape could be fitted, or channel waveguides, where light is not easily coupled with a prism, none of the above described methods can be employed. In those cases, *far field* [177] or *near field* [178] are used. They are based on the direct observation of the actual intensity distribution of light inside the waveguides and the analysis of the diffraction pattern at the output of the polished edge.

3.2 Nonlinear optical properties in waveguides

The properties of nonlinear media were treated in the previous chapter (section 1.4.3). Throughout this thesis work, nonlinear optical waveguides have been studied, meaning that we have dealt with waveguide fabrication methods that preserve the nonlinearity of the material ($LiNbO_3$ in this case) in order to take advantage not only of the high confinement due to waveguide configuration, but also of the good properties of the substrate. Therefore, how waveguide fabrication affects the nonlinear properties of the substrate has to be studied, in order to obtain the most appropriate structures for nonlinear applications.

3.2.1 Optical frequency doubling in waveguides

Among the different nonlinear frequency conversion phenomena, we will focus now in the optical frequency doubling in waveguides (note that the concepts for other nonlinear frequency conversion processes are equivalent). One of the greatest advantages of waveguide configuration is the high optical intensity that can achieved inside a waveguide and that this intensity can be maintained over long distances. This makes waveguides optimal structures for efficient frequency conversion. In the simplest

model (for low efficiencies) of SHG, the efficiency of the generated light is proportional to

$$|S(2\omega)|^2 \propto \omega^4 d^2 I^2 \tag{3.4}$$

being ω the fundamental frequency, d the corresponding nonlinear coefficient, and I the intensity of the incident wave. This intensity can be written as $I = P/A$, where P is the incident power and A is the cross-sectional area. It is easy to see that in order to increase the generation of second harmonic, the power of the incident light should be made as large as possible, and the incident beam should be tightly focused. Another way of enhancement of the second harmonic efficiency is to have the longer possible interaction region. Waveguides are really attractive for this purpose, thanks to the high confinement that make possible higher intensities and larger interaction regions because light can be guided for long regions.

Requirements for SHG in waveguides

As it was seen in equation 3.4, the SHG efficiency is proportional to the second order susceptibility. In the case of waveguides, most fabrication processes lower the nonlinear coefficient values of $LiNbO_3$ [179], but this loss varies a lot between the different kinds of waveguides studied in this work. Therefore, one of the objectives is to characterize various $LiNbO_3$ waveguides in order to study the preservation of the nonlinear coefficients.

Another important feature in waveguides that is not present in bulk SHG, is the mode overlapping. To have a better physical insight, one can solve the nonlinear wave equation for the second order nonlinear term of equation 2.1 and making some simplifying assumptions:

- The interaction between one fundamental mode at frequency ω and another second harmonic mode at frequency 2ω is considered. The variation of the wave amplitude along one wavelength is negligible (*slowly varying approximation*).

- The intensity of the pump beam does not vary appreciably (*undepleted pump approximation*).

Taking all of this into account, the growth rate of the second harmonic generated light is given by:

$$\frac{dE_{2\omega}(z)}{dz} = -iKE_{\omega}^{2}(z)e^{-1\Delta\beta z} \tag{3.5}$$

being $\Delta\beta$ the phase velocity mismatch between the fundamental and second harmonic waves and K the coupling constant.

As far as the phase velocity mismatch is concerned, it can be written as

$$\Delta\beta = \beta_{2\omega} - 2\beta_{\omega} = 2\pi\left(\frac{N_{2\omega}}{\lambda_{2\omega}} - 2\frac{N_{\omega}}{\lambda_{\omega}}\right) = \frac{2\pi}{\lambda_{2\omega}}\left(N_{2\omega} - N_{\omega}\right) \tag{3.6}$$

being N_i the effective refractive indices and λ_i the wavelength. It is easy to see that the maximum growth rate will happen if the effective refractive indices for both wavelengths are equal. But there is another way, also mentioned in the previous chapter, of having *quasi-phase-matching* (QPM) between both the fundamental and generated wavelengths. This method consists on the periodic inversion of the relative phase of the interacting waves. Then, another factor appears in the phase mismatch term

$$\Delta\beta = \beta_{2\omega} - 2\beta_{\omega} - \frac{2\pi m}{\Lambda} \tag{3.7}$$

where Λ is the grating period and m is an integer which indicates the order of the QPM. This term corrects by means of the periodic structure the phase mismatch. But obviously, although we are no longer limited by the actual values of the effective indices, the periodicity of this structure has to be very good, because otherwise, the phase mismatch will occur again. The most effective periodicity is that of the coherence length, but also odd integer times this length produce QPM, but in a less effective way.

With regard to the coupling constant, it is given by

$$K = \frac{\omega d_{eff}}{cN_{2\omega}} \int\int \epsilon_{2\omega}(x,y)\epsilon_{\omega}^{2}(x,y)dxdy \tag{3.8}$$

where c is the speed of light and d_{eff} is the nonlinear optical susceptibility in the waveguide. This coupling constant, also called overlap integral, represents the inverse effective cross-section of the interaction. That means that it represents the specific interaction between the fundamental and the second harmonic generated waveguide modes. In order to generate second harmonic light in an efficient way, the conversion process should be done with modes with a large overlap area. A schematic illustration of two typical situations is given in figure 3.4.

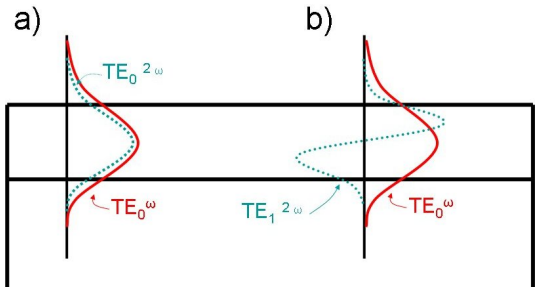

Figure 3.4: Two examples of field distributions of fundamental and generated waveguide modes for SHG a)a fundamental TE_0^{ω} gives rise to a $TE_0^{2\omega}$ (large interaction area). b)a fundamental TE_0^{ω} mode gives rise to a $TE_1^{2\omega}$, (very small interaction area).

SHG efficiencies obtained in waveguides

To get an idea of the results achieved with nonlinear waveguides, one can use the normalized conversion efficiency

$$\bar{\eta} \equiv \frac{P_{2\omega}(L)}{[P_{\omega}(0)]^2} = \eta L^2 \tag{3.9}$$

which units are %W^{-1}, and being η the efficiency of the SHG and L the interaction lenght. In table 3.1 a relation of the normalized efficiencies obtained in different waveguides can be found.

Waveguide type	$\lambda_{2\omega}$ (nm)	Domain inversion	$P_{2\omega}$ (mW)	$\bar{\eta}$ $(\%W^{-1})$	Year	Ref.
APE pl.	532	Ti-indif	5×10^{-7}	4×10^{-2}	1989	[133]
APE ch.	410	Ti-indif	1.1×10^{-3}	0.36	1989	[132]
APE ch.	532	heat treatm	2.6×10^{-5}	16.3	1991	[82]
APE ch.	435	Ti indif.	0.65	6.8	1992	[94]
APE ch.	425.9	e.b.s.	20.7	47	1993	[226]
APE ch.	432	e.f.p.	1.7	128	1996	[94]
Ti-ind. ch.	422.5	e.f.p.	0.0079	0.39	1997	[7]
APE ch.	421	Ti-indiff.	25	110	1997	[217]
SPE pl.	830	e.f.p.	1×10^{-6}	210	2000	[61]
APE(x-cut) pl.	386	e.f.p.	1.2	1000	2001	[203]
Zn-ind. ch.	397.8	Czochralski	78×10^{-6}	10^{-4}	2002	[71]
Ti-ind. pl	412.6	e.f.p.	6	$22.8/cm^2$	2004	[41]

Table 3.1: Some results of efficiencies and actual obtained powers of second harmonic generation in waveguides. The acronyms stand for: APE, annealed PE; Ti-ind. Ti-in-diffusion; ch. channel; pl. planar; e.b.s electron beam scanning; e.f.p. electric field poling.

3.2.2 Optical damage in waveguides

An important feature in $LiNbO_3$ integrated optics is the maximum power that the device can safely handle in operation. In most cases, this maximum power is limited by the phtorefractive optical damage, which is particularly present in $LiNbO_3$ within the visible region of the spectrum. As an example, frequency doublers based on periodically poled $LiNbO_3$ annealed PE-waveguides, have produced up to $30\,\mathrm{mW}$ of blue light [217, 200], a maximum value which is apparently limited by optical damage.

Nevertheless, the measurement of the optical damage effect in the case of waveguides is not a simple issue. Even though, there are many works in which the optical damage resistance of planar $LiNbO_3$ waveguides is studied basically with different experimental techniques: interferometric [84], holographic [104], and single beam technique [90]. With these techniques different types of waveguides have been studied, such as PE [120], Ti-indiffusion [83], and ion implanted [91]. The main problem is that the data obtained in these experiments for different kinds of waveguides is difficult to compare. One of the main causes is that the substrates, although nominally pure, usually have a remaining impurity concentration that influences the optical damage effect. Moreover, the waveguide fabrication technique modify certain parameters that also modify the optical damage behaviour. In order to make a comparison among different waveguides, the concept of *optical damage threshold* should be well defined, which is not usually the case.

Despite these inconveniences, some qualitative results can be extracted from the literature, such as the higher optical damage threshold that planar PE and Zn-in-diffused waveguides present compared to that of bulk congruent $LiNbO_3$ (higher light intensities can be propagated into the

waveguide without beam distortion) or the reduction of optical damage when the waveguides are fabricated in Mg doped substrates. Anyhow, in order to have reliable comparative measurements, a comprehensive analysis of the optical damage effect in different kinds of waveguides and geometries (PE, Zn-in-diffused, Ti-in-diffused, fabricated in x-cut or z-cut substrates, planar or channel configuration, waveguides periodically poled...) has been carried out in this thesis work, in order to find the most suitable for carrying the high intensities required nonlinear frequency conversion.

Part II

Experimental Techniques

Chapter 4
Experimental techniques

Experimental techniques

In this chapter the different experimental techniques used in this thesis work will be described. Firstly, different fabrication methods, along with the sample preparation necessary to carry out the experiments, will be shown. Then, several techniques used to characterize the waveguides in order to study and optimize their nonlinear performance to obtain efficient waveguides for frequency conversion applications, will be described. In order to obtain periodically poled lithium niobate, two different techniques, namely the *off center Czochralski* and the *electric field poling*, will be outlined. Finally, the experimental setups used for the study of the ferroelectric domains, the dynamics of the domain reversal on proton exchanged samples and their performances will be reported.

4.1 Waveguide fabrication

4.1.1 Proton exchange

Proton exchange is the waveguide fabrication technique most employed in this work. The exchange process consists on the substitution of ions Li^+ with H^+. These incoming H^+ do not exactly replace the Li^+ ions, but are placed in the oxygen plane (see section 1.3.3). Therefore, a new

layer $H_xLi_{1-x}NbO_3$ appears in the surface of the $LiNbO_3$ substrate, where the extraordinary index is increased and the ordinary index decreased. Besides, this layer also gives rise to a certain stress in the **z** axis, because of the difference between their crystal lattices [49, 121]. Given that $LiNbO_3$ is a photoelastic, piezoelectric and electro-optic material, different phenomena are produced in the crystal. The stress gives rise, due to the photoelastic effect, to changes in the refractive index. At the same time, via the piezoelectric effect, an electric field is also produced, which in turn modifies the refractive index by means of the electro-optic effect. As a result, an increase in the extraordinary refraction index, where light can be guided, and a decrease in the ordinary index [184] take place.

Sealed ampoule technique

The most common proton exchange process consists on the immersion of a substrate in an acid melt. In our case, congruent optical grade polished $LiNbO_3$ was purchased to *Photox Optical Systems, Oxford*. Due to the variety of experiments performed, x and z-cut wafers were used, $3\,\mathrm{inches}$ diameter and 1 or $0.5\,\mathrm{mm}$ thick. Samples were sawn from these wafers to an approximate surface size of $20 \times 8\,\mathrm{mm}^2$ (**x** and **z** directions in x-cut wafers; **x** and **y** directions, in z-cut, respectively). To perform certain measurements, especially when dealing with z-cut samples, it was necessary to assess that only one of the faces was proton exchanged. Therefore, a $0.1\,\mu\mathrm{m}$ silicon oxide layer was deposited in one of the faces, by plasma deposition, to prevent the exchange. In figure 4.1 the fabrication method of the proton exchanged waveguides can be seen. They were produced by immersion of the substrates in a benzoic acid melt buffered with lithium benzoate within a sealed Pyrex ampoule [67, 163]. To separate the melt from the sample, the ampoule is narrower in the middle, (see figure 4.1). Different crystallographic phases can

be produced varying the exchange temperature, time and acidity of the sample, as will be shown in section 4.1.1

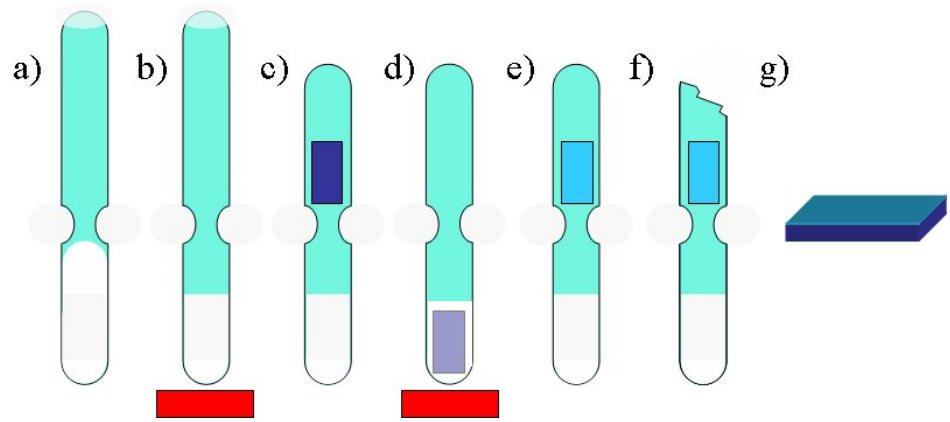

Figure 4.1: Different steps of the proton exchange process: a) Benzoic acid and lithium benzoate are introduced in an ampule b) The ampoule is introduced in the oven and the components are melted c) A $LiNbO_3$ substrate is introduced in the ampule and then it is sealed in open air d) The ampule is introduced in the oven and it is rotated $180°$, being the sample immersed in the melt for a certain time e) The oven is rotated again and cooled down f) The ampule is broken g) The process gives rise to a planar waveguide.

The whole fabrication process can be seen in figure 4.1, and it can be described as follows: Once the sample and the melt are ready and placed inside the ampoule, it is sealed in open air [1]., and introduced inside a furnace, which were designed and fabricated in our laboratory. The temperature of these ovens is controlled with a thermocouple placed in an aluminium tube near the exchange zone, inside the oven, and an Eurotherm (mod. 903-A) controller, which gives a precision of 0.1º C and they were designed in such a way that they can turn around on their horizontal axis. This feature, combined with the fact that the sample and the melt are separated unless the ampoule is turned upside down, gives us a precise control of the exchange time. To begin the exchange process, being the

[1]The sealing of the ampoules was made in the workshop facilities of the university, SEGAINVEX

temperature the desired one, the oven is turned down. Then, the sample is immersed in the melt and the exchange takes place. To prevent the inhalation of toxic benzoic acid vapours, mainly when there is a breakdown of the ampoule (see fig. 4.2.a), the ovens are placed inside a fume hood, as can be seen in figure 4.2.b. To finish the process, the oven is rotated again and the ampoule is extracted from the oven. Finally, once it is cooled down to room temperature, the ampoule is sawn and the $LiNbO_3$ substrate with the waveguide structure is finished.

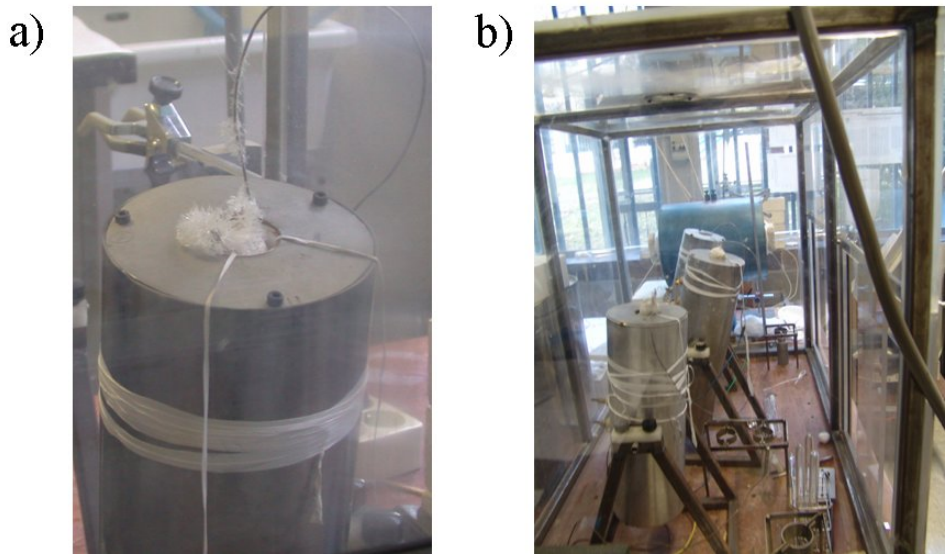

Figure 4.2: a) One of the ovens with solidified benzoic acid after the breaking of an ampoule. b) The ovens in the fume hood where they are placed to prevent hazardous vapours.

Pure crystalographic phases

Depending on the conditions of the process, such as melt composition, acidity, atmosphere, time and temperature of the exchange, the features of the obtained waveguide can vary appreciably. Moreover, there have been

defined some crystallographic $H_xLi_{1-x}NbO_3$ phases [121], which usually appear mixed together in the PE or Annealed Proton Exchanged (APE) waveguides. Studies on the properties of different proton exchanged waveguides (PE, APE, SPE) abound in literature [136, 126], although not much care is usually taken to determine which kind of crystallographic phase is being studied. In our group the processes to obtain pure crystallographic phases were already developed [163, 65, 6] and in this work we were able to fabricate, study and compare pure α and β_1, Vapor Proton Exchange (basically, β_2-phase) and reversed proton exchanged (RPE) waveguides in x-cut and z-cut $LiNbO_3$ samples. The parameters used for each kind of waveguide are shown in the table 4.1

Crystalline phase	Cut	%Lithium benzoate	T (^{o}C)	Time
α	X,Z	3	300	$18-96\,\mathrm{h}$
β_1	X,Z	1	300	$0.5-46\,\mathrm{h}$
VPE	Z	0 (Vapour)	$300-305$	$4-24\,\mathrm{h}$
Reversed P.E.	X	1 Reverse treatment: (1:1:1)(Li:Na:K)NO_3	300 315	$46\,\mathrm{h}$ $46\,\mathrm{h}$

Table 4.1: Fabrication parameters to obtain different pure crystallographic phases via proton exchange.

4.1.2 Metal in diffusion waveguides

Another waveguide fabrication method commonly used in $LiNbO_3$ is the diffusion of metals (titanium, zinc, nickel and others). These processes give rise to waveguides of gaussian index profiles [117]. Given that Titanium in diffused waveguides are extensively used in literature and easily available commercially, we have used them as a reference for the performance of our proton exchanged waveguides in some experiments,

as, for instance, optical damage measurements. We have also used zinc diffused waveguides prepared by the AMIGO group of the U.A.M. (G. Lifante *et al.*, [160, 52]).

In order to fabricate Ti:$LiNbO_3$ waveguides, a thin layer of titanium ($\sim 100\,\mathrm{nm}$) was electron beam evaporated (Telemark, mod 231) on congruent $LiNbO_3$ substrates. They were introduced in an oven, which could reach temperatures up to $1200^\circ\,\mathrm{C}$. To avoid the out diffusion of lithium and the reaction of $LiNbO_3$ with the alumina [9], the samples were placed in a platinum box. There, they were heated at a rate of $8^\circ/\mathrm{min}$ up to $1000 - 1100^\circ\,\mathrm{C}$. They were kept at this temperature for $9 - 10\,\mathrm{hours}$, always in wet oxygen atmosphere also to prevent any lithium loss [106]. After that, the samples were slowly cooled down to room temperature. These waveguides can guide both ordinary and extraordinary polarized light. The problem was that they broke easily, which made them not suitable for many experiments. In the case of the measured samples throughout this work, they were fabricated in our laboratory. Although the experience of our group in these waveguides is limited, it was preferred this way to have a better control over the substrates employed in all the samples in order to compare different kind of waveguides in a better way. Nevertheless, it was quite difficult to achieve the measurements in our Ti-in-diffused waveguides because they easily broke under the coupling pressure.

As far as Zn:$LiNbO_3$ waveguides are concerned, their study is quite recent. Zinc doping in $LiNbO_3$ presents a main advantage: it is known to reduce optical damage. Therefore, different zinc waveguide fabrication processes have been developed to take advantage of this feature along with the high confinement due to waveguide configuration ([14, 214, 229]). In this work, the zinc diffused waveguides were obtained through a two step process, described in [160, 70]. In a first stage, the sample is heated at 550^o C for 2 hours in a Zn atmosphere. As a result, a rich Zn layer is formed

in the surface of the sample. The second step consists on an annealing in open air at 800º C for 4 hours, in order to diffuse the Zn into the $LiNbO_3$ substrate. This procedure gives rise to an increase in both extraordinary and ordinary refractive indices in a layer of $\sim 5 - 6\,\mu\mathrm{m}$ with a smooth gaussian profile.

4.1.3 Ion beam irradiated waveguides

Apart from the most common waveguide fabrication techniques, in this work there have also been studied to some extent ion irradiated $LiNbO_3$ waveguides. They were fabricated at the "'Centro de Microanálisis de Materiales"' (CMAM) by the group of Photonic Applications with Ions (J. Olivares, F. Agulló-López *et al.*).

High energy low fluence irradiation

At difference with light ion implantation, which has been widely used to obtain optical waveguides in dielectric and electrooptic materials [213], heavy ions such as Ni^{2+} [137], Si^{+} [101], O^{3+} [21], F^{4+}, Cl^{8+} [88] are starting to be used to fabricate waveguides with higher energies but lower doses. The refractive index obtained when dealing with light ions is due to nuclear collision damage, but in the case of heavy ions, the electronic damage is the main cause of the refractive index change. This second technique overcomes some of the disadvantages the light ion implantation, such as the large fluence of ions required (10^{16}-10^{17} cm^2) and the contamination of the material with the irradiated ions in the optical barrier. Moreover, the profile index shapes obtained with this new technique is sharper and the index change is higher and the barrier can be thicker.

In the case of the samples studied here, they were irradiated with F^{4+} at energies of $20 - 22\,\mathrm{MeV}$ in the 5 MV tandetron accelerator of the CMAM [170], with fluences as low as $\sim 10^{14}\,\mathrm{cm}^{-2}$, as described in [164]. In this case, the refractive index change is caused by electronic excitation. An schematic view of the refractive index change that the ion irradiation produces in the material can be seen in figure 4.3. With the ion energies used for the irradiation, the electronic stopping power reaches a maximum beneath the surface, with a value close to the amorphization threshold. The surface layer remains crystalline, thus the optical waveguide core preserves the properties and refractive indices of virgin $LiNbO_3$, and an amorphous low index layer ($n = 2.10$ at $\lambda = 633\,\mathrm{nm}$) is created by the swift ion-beam irradiation. In addition, the F^{4+} ions go far inside the $LiNbO_3$ and they do not affect the optical waveguide.

As a result of this technique, the high-step index jumps created ($\Delta n_o \sim 0.2, \Delta n_e \sim 0.1$) allow the propagation of highly confined modes. The optical losses of this waveguides were also measured with the scattered light detection technique, and they were found $\sim 1\,\mathrm{dB/cm}$ [164].

Swift ion irradiation at ultra-low fluences

This new kind of waveguides was also fabricated at the CMAM, using chlorine ions at ultralow fluences [167]. The formation of the waveguides can be described as follows: when the electronic stopping power is above a certain threshold, ($\sim 5\,\mathrm{keV/nm}$ in the case of $LiNbO_3$), amorphous tracks are created along the trajectory of the ions into the material. In figure 4.4, a scheme of the formation of these waveguides can be seen. The radius of the track depends on the irradiation conditions. If swift-heavy ions are irradiated at a very low fluence, the tracks formed do not overlap, and instead of an amorphous layer as in the previous section, a nanostructured heterogeneous medium of single nanometric tracks and

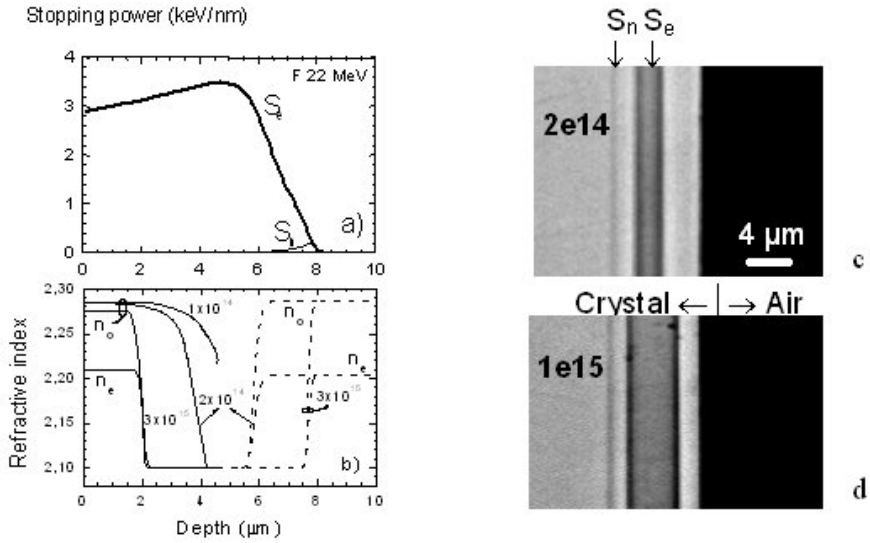

Figure 4.3: a) shows the electronic stopping power for F^{4+} at $22\,\mathrm{MeV}$ in $LiNbO_3$ [164]. b) The refractive index profiles of z-cut samples with this irradiation at different ion fluences (at/cm^2) [164] c) and d) Optical microphotographs of a polished y-cut cross section for samples irradiated with F^{4+} at fluences of 2×10^{14} (c) and 1×10^{15} (d). The depths of the maximum electronic stopping power, (S_e) and nuclear stopping power (S_n) are indicated with arrows [165].

crystalline $LiNbO_3$ is formed. This gives rise to a waveguide structure because the tracks have an amorphous core, with lower index than $LiNbO_3$, and a preamorphous damaged halo [168, 166] with lower refractive index than congruent lithium niobate.

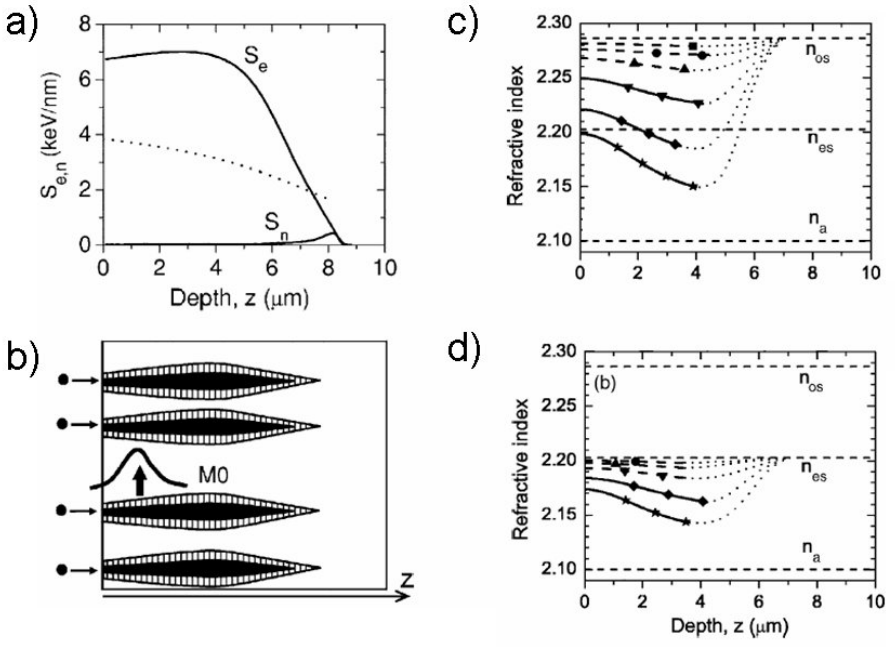

Figure 4.4: a) electronic S_e and nuclear S_n stopping power curves for Cl $48.5\,\mathrm{MeV}$. The dotted curve corresponds to the amporphization threshold. b) Scheme of the morphology of the tracks in depth. The core is black and the halo is dashed. (MO) stands for a probable light profile in this waveguide. c) ordinary and d) extraordinary index profiles of samples irrdiated with Cl $45.8\,\mathrm{MeV}$ at different fluences. (These results have been taken from reference [166]

4.1.4 Channel waveguides

For nonlinear optical applications, it is convenient to have as much light power as possible in our device. Therefore, channel waveguides were fabricated to obtain higher light confinement. Photolithographic masks [2] were used to fabricate arrays of channel waveguides, with widths ranging from 1 to 20 μm. The process, showed in figure 4.5, can be briefly

[2]The photolithograpic processes in Madrid were made in the Microelectronics Laboratory by Eduardo Ruiz

described as follows: first, a silicon oxide layer is deposited on one of the faces of the substrate via plasma deposition. Then, the sample is coated with a positive resist (Microposit S1813 photo resist) by spinning to obtain a uniform layer on the same face and is soft baked. After this preparation, the mask and sample are placed in a proper aligner and exposed to ultraviolet light. Being the resist a positive photosensitive material, the areas which have been irradiated can be now selectively removed with the aid of an special developer (Microposit developer). Then the sample is hard baked at 120° for some minutes to strength the remaining photoresist. At this point, the pattern has to be transferred from the resist to the silicon oxide, and this can be made with Reactive Ion Etching (RIE), which combines ionic bombing (energies between 300-700 eV) with chemical processes. Once the SiO_2 is structured, the resist is removed with acetone and the substrate is ready for proton exchange waveguide fabrication. A microscope image of this SiO_2 channels can be seen in figure 4.7.a.

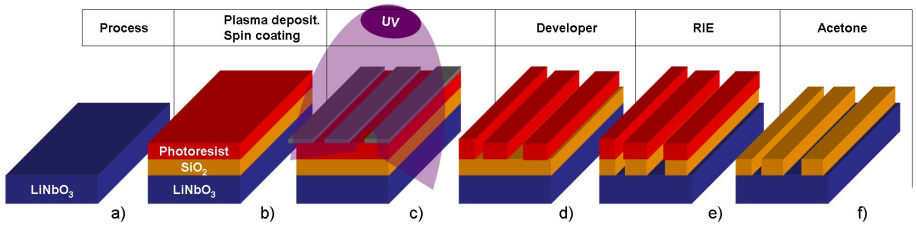

Figure 4.5: a) bare $LiNbO_3$ substrate b) one of the faces is covered with SiO_2 and a positive resist. c) Illumination through a mask with ultraviolet light d) Irradiated photoresist is removed with a developer e) SiO_2 removed with Reactive Ion Etching (RIE) f) After the remaining photoresist is removed with acetone, the sample has a SiO_2 mask.

4.1.5 Cutting and polishing of the samples

As was mentioned before in Section 4.1.1, the commercial wafers had to be cut to smaller size samples before the proton exchange process 4.6. This was made with a diamond disk cutting machine (*Metal Research*). Around 20 samples were obtained from each wafer. Then, they were marked with a diamond pen to be able to distinguish their faces and between samples.

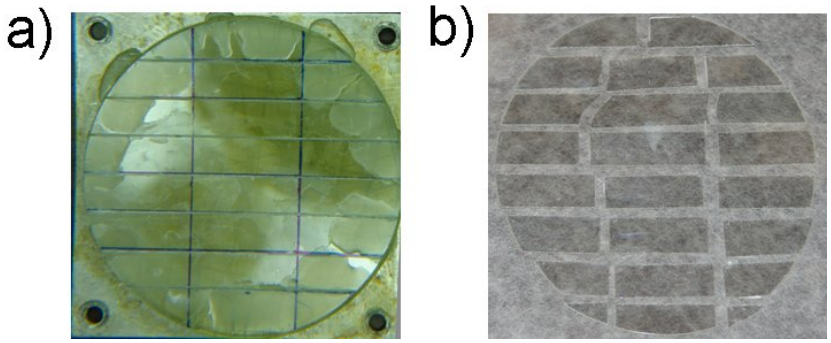

Figure 4.6: a) 3 inches $LiNbO_3$ wafer prepared to be cut in samples for waveguide fabrication. Actually, all the horizontal lines have been already cut, and the vertical are marked. b) The same wafer once it has been cut and cleaned. 21 effective substrates were obtained.

Apart from the commercial congruent $LiNbO_3$ substrates, some as grown poled erbium doped $LiNbO_3$ substrates were also used [3]. In those cases, samples had to be cut first in thin layers, taking into account the crystallographic axes, which can be distinguished in the crystal due to its shape and characteristic striae. Once the wafers were prepared, the surfaces had to be polished to optical grade. At the first stages of this work, the polishing was made sample by sample by hand, with diamond polishing compounds (*Buelmer*) ranging between 15 and 0.25 μm. This time consuming technique was replaced by a commercial polishing

[3] These crystals were grown in the Crystal Growth Laboratory by Dr. Bermúdez

machine (*Logitech*), where abrasive chemical compounds (Calcined aluminium oxide Powder 9 μm and Polishing Suspension Type SFI, *Logitech*) made the polishing. Not only does this commercial machine save time, but it has also other advantages, such as a better parallelism of the faces and that only two kinds of chemical compounds were necessary, instead of 5 different diamond size powders.

For some of the measurements made in planar waveguides and all the ones made in channel waveguides the edges had to be polished, because the light had to be fired end coupled. Also in the case of channel waveguides, the mask does not usually cover the whole surface as can be seen in figure 4.7.a. Then, to couple light in a channel, one has to get rid of this section of the substrate. In order to use the polishing machine for the edges as well, a special accessory was purchased. To preserve the sharpness of the edges, special care had to be taken. A simple way to prevent this is to stuck a number of samples together, as it can be seen in the picture 4.7.b.

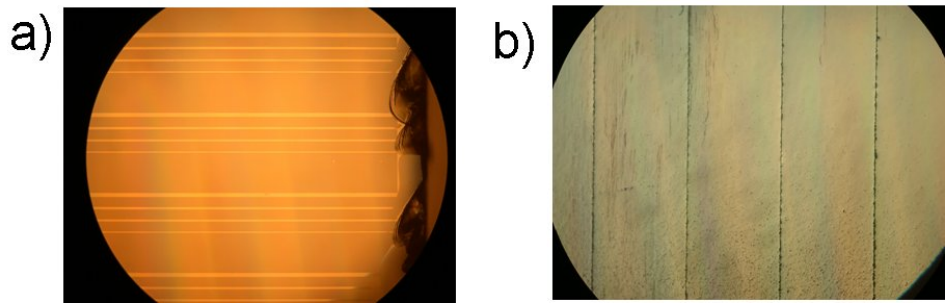

Figure 4.7: a) Surface photograph of the SiO_2 mask of a channel waveguide. It can be clearly seen that the channels do not reach the edge. b) Polished edges of some samples.

4.2 Waveguide characterization

The characterization carried on the waveguides inquire into their optical properties, that is, refractive index profile, optical losses and so on. But in our case we pay particular attention to the nonlinear optical and electrooptical properties, because it was very important to fully typify the waveguide in order to find the most suitable ones for nonlinear optical applications. Therefore, optical damage and nonlinear coefficients were also studied.

4.2.1 Refractive index profile: Dark modes

The dark modes technique, also called m-line spectroscopy, was implemented in our laboratory by J. Olivares [163]. A brief scheme of the experimental setup can be seen in figure 4.8.

Given that the dark modes technique is extensively treated in many other thesis works of our group [65, 6], an abridged explanation of the setup will be given here. The continuous light sources used are an argon laser (Omnichrome, mod 543-AP, $\lambda = 457, 488, 497, 514\,\mathrm{nm}$,), a He-Ne laser (Uniphase, mod 1125, $\lambda = 632.8\,\mathrm{nm}$) and an Ns:YULF infrared diode laser (Spectraphysics, $\lambda = 1040\,\mathrm{nm}$)). After passing through a polarizer, the beam is expanded with a microscope objective (40x) and collimated with a spherical lens. Then, to have a wide range of $\vec{k}$ vectors reaching the waveguide, light is focused on the sample with another lens. A rutile (TiO_2) biprism is used to couple light into the waveguide. To assess a good optical contact between the prism and the guide, they are pressed against each other. The holder we use can be seen in fig 4.9, where even the optical contact can be distinguished.

This rutile biprism also decouples most of the incoming light, except

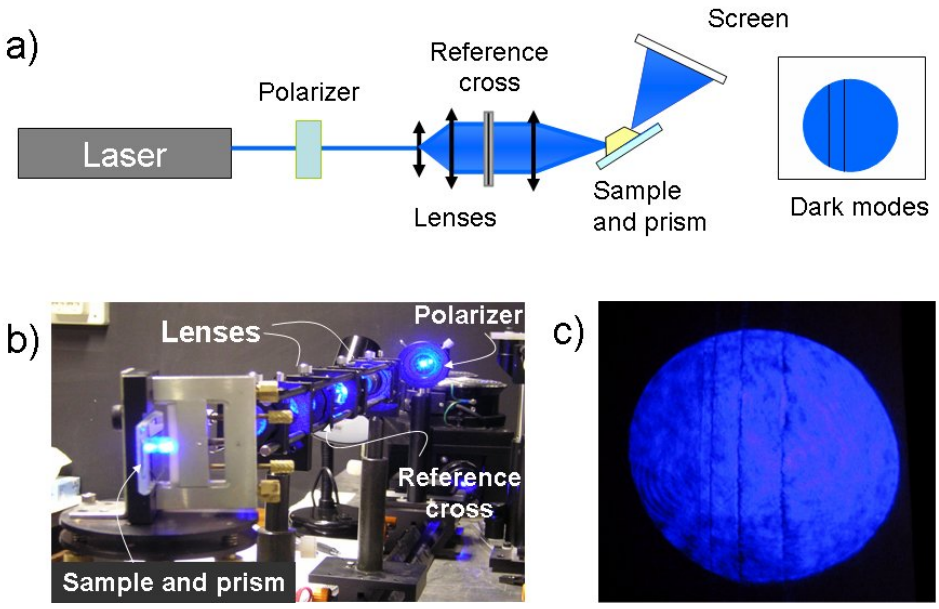

Figure 4.8: a) Sketch of the experimental setup necessary for the characterization of the index profile with the *dark modes* technique. b) Photograph of the actual setup. c) Photograph of the dark modes as they appear on the screen.

from the light matching the angles which fulfill the self-consistency equation. For these angles, light is guided in the waveguide and they produce dark lines in the image corresponding to the outcoupled light. The angles which satisfy the guiding condition can be measured with an accuracy of $\sim 0.001°$, thanks to a cross placed in the optical path between the two lenses, and to a circular precision rotation stage, with stepper motor and optical encoder, which holds the sample. Once these external $\varphi_{exp,m}$ angles are determined, and given that the geometry (see figure 4.10) and refractive indexes of the prisms and substrate are known, from the measured values of $\varphi_{exp,m}$, the effective index for each mode can be obtained.

Once the angles which the light is guided at have been measured, and

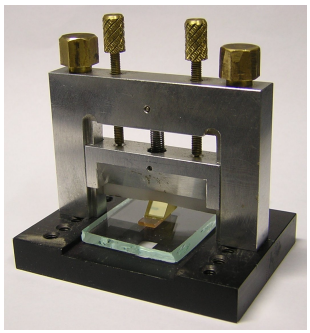

Figure 4.9: Optic contact between the rutile prism and the waveguide.

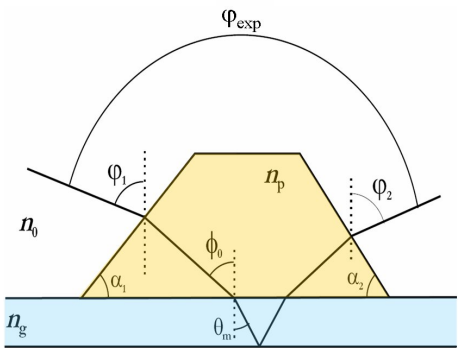

Figure 4.10: Scheme of the prism-waveguide coupling from the ray-model point of view.

providing that the angles and refractive indices of the rutile prism and $LiNbO_3$ are known, the effective refractive indices can be obtained. There are different calculation methods, such as WKB or reflection calculation method (described in section 3.1.3), with the aid of several computer programs [163]. In most cases, the profiles so obtained have enough precision. Nevertheless, if the number of modes were not enough or a more accurate profile was needed, a more sophisticated calculation method based on the exact resolution of the wave equation in an analytic index profile was used [4] which supplies a much better profile, based on the

[4]The program used was made by Prof. Cabrera

minimization of the differences between the experimental modes and the calculated ones.

In order to know the refractive indices for different wavelengths in $LiNbO_3$ waveguides in order to design devices for frequency conversion, a first study with different Sellmeier adjustments was made. Then, it was found more convenient to use the SNLO software [5], a very user friendly program that, calculates the coherence length (see section 2.1.3) and its temperature dependence.

4.2.2 Optical losses

Propagation losses were evaluated by measuring the scattered light detection technique of a coupled mode [78]. There, the scattered light intensity out of the waveguide of a guided mode is monitored with a CCD camera. Although only the scattered light at 90° can be detected, this is expected to be proportional to the intensity scattered inside the waveguide at the same point. Then, the decay of scattered light along the waveguide can be mapped from the image of the propagated mode captured with the camera. The corresponding intensity for each point follows equation 4.1

$$I_L = I_0 exp(-\alpha \cdot L) \tag{4.1}$$

where I_L is the intensity of scattered light at a propagation length L, I_0 the intensity at the beginning of the propagation and α the loss coefficient. A brief scheme of this technique can be seen in figure 4.11. Light was in coupled with a rutile prism, and then propagated along the waveguide for around $20\,\mathrm{mm}$. Once the image has been recorded, with an appropriate

[5] Written by A. Smith at Sandia National Laboratories

software [6] , the light intensity at different propagation lengths is extracted and plotted. The value of α is obtained from the fit of these data.

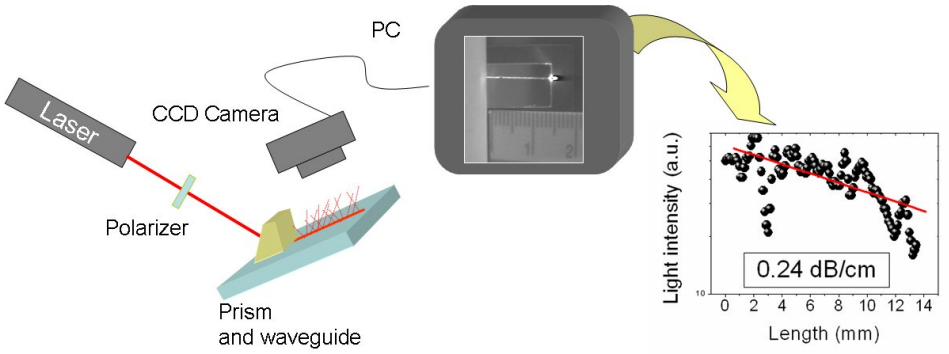

Figure 4.11: Scheme of the experimental setup used for the measurement of propagation losses, with the scattering light technique.

4.2.3 Absorption measurements

Although we are usually interested in the properties of the waveguides, sometimes it is also important to know if after certain aggressive processes, the exchanged layer has been completely removed. In the case of proton exchanged waveguides, there is an straightforward method to check if there is an exchanged layer with the aid of an spectrophotometer.

It was already said at the beginning of chapter I that oxidized $LiNbO_3$ is colorless and transparent. But there are two regions of spectroscopic interest, being one the absorption edge in the ultraviolet, and the other one the absorption band of the O–H bonds, which lays in the infrared. The first one is sensitive to the stoichiometry of the crystal, and will not be used here. And the second one gives information of the presence of hydrogen

[6]Different software applications have been used, for example the public domain program ImageJ 1.36 (available in http://rsb.info.nih.gov/ij)

in the sample produced by the proton exchange process. A double beam spectrometer (Hitachi, mod. U3501) has been used to measure the regions 2950 - 2750 nm and 2400 - 2150 nm (forbidden transition).

4.2.4 Photovoltaic currents

The measurements of photovoltaic currents were made for x-cut planar waveguides. A scheme of the experimental setup can be seen in figure 4.12. Light was in- and out-coupled through rutile prism couplers, separated $\sim 15\,\mathrm{mm}$ in the **y** crystallographic direction. The photovoltaic current was recoiled thanks to two aluminium electrodes evaporated on the **x** face of the sample, also with the electron beam evaporator (Telemark, 231) used for Ti deposition. Their size was $0.0003 \times d \times 2\,\mathrm{mm}^3$ in **x**, **y**, **z** respectively, with d ranging from 9 to 16 mm. The distance between the electrodes was of $1\,\mathrm{mm}$ in the **z** direction, being the laser beam width larger than it. The steady value of the current produced under illumination was measured after the transient pyroelectric current disappeared. Two different picoammeters were used during this work, a Kithley M-610C (sensitivity of 0.01 pA) and a newer model, Kithley Model 6485 (also 0.01 pA sensitiviity)

In order to study the dependence of the photovoltaic current on the wavelength, a 15 W argon laser (Spectra Physics, mod. 2040) along with a solid state laser (Mod. Verdi from Coherent, 5 W at 532 nm) were used.

The calculation of the actual light intensity inside the waveguide has been made measuring the out-coupled intensity from the output prism and the method proposed in appendix. The power density was calculated taking into account the effective thickness of the different waveguides for the fundamental mode and the distance between the electrodes.

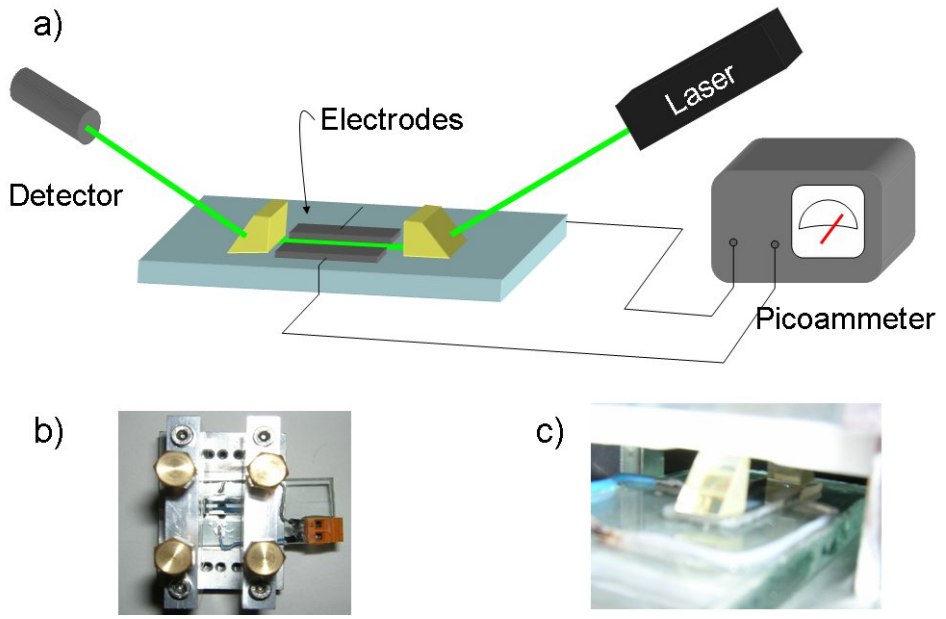

Figure 4.12: a) Scheme of the experimental setup used for the measurement of photovoltaic currents. b) Sample in the holder, with the electrodes and electronic connections. c) Detail of the prism couplers and cable connections.

4.2.5 Optical Damage

As it was already mentioned in the first chapter (section 2.4), the term optical damage refers to the beam distortion found at high light intensities due to the photorefractive effect. Throughout this work, optical damage has been studied for different waveguides in both $LiNbO_3$ and periodically poled $LiNbO_3$ substrates to characterize this effect, as it will be shown in chapter 6. To accomplish these measurements for waveguides, the experimental setup described in [6, 5] was used with most of the samples. In this case, light is coupled with a rutile prism into the fundamental mode of the waveguide, as can be seen in figure 4.13. To assess a good coupling, a large focal lens (f $\approx$30 cm) was used. Special care was taken to guarantee that in those cases, the beam waist produced by the lens coincided with

the light path along the waveguide. That also provides a definite width of the propagating laser beam inside the waveguide of $\sim 80\,\mu\mathrm{m}$.

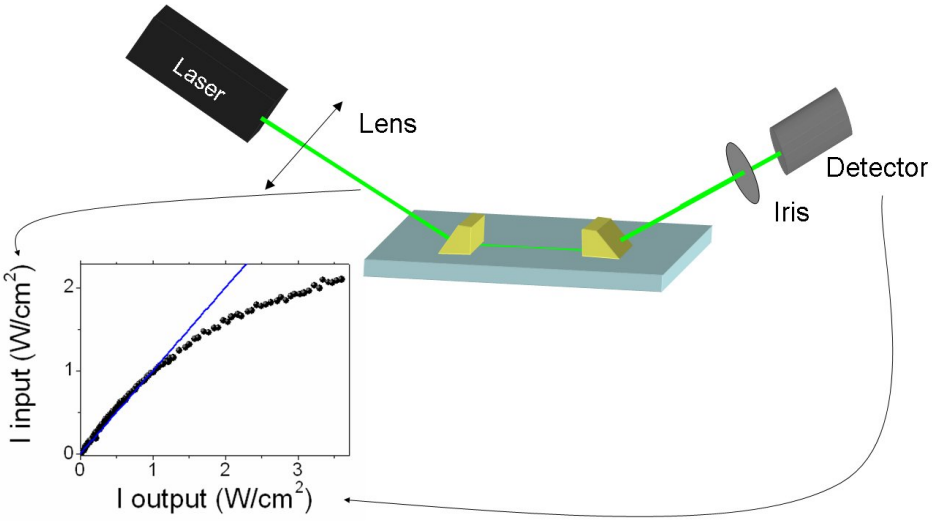

Figure 4.13: Experimental setup used for optical damage measurements in planar waveguides. A typical result of the in-coupled light intensity versus the out-coupled can be also seen.

This method can only be achieved for planar waveguides. In the case of channel waveguides, light was coupled and decoupled by means of microscope objectives, and the width of the propagating beam was determined by the channel width itself. Besides, in planar waveguides it was found that, with the 0.5 mm thick z-cut $LiNbO_3$ substrates used for periodic poling, the pressure necessary to have optical contact between the waveguide and the prism broke most of the samples. In those cases, the beam was focused with the lens and coupled with a prism, but edge decoupling was preferred.

In both cases, to determine the optical damage threshold, the out coupled light at low intensity, was detected with a silicon photodetector. The restriction to the widening of the out coming light was made placing

an iris diaphragm before the detector, which let only pass the beam diameter at low intensity. Then, the input power was increased and only the light emitted in the same direction and within the diaphragm aperture as before was recoiled. An illustration of a typical result obtained in the laboratory is presented in figure 4.13, where there is a plot of the light intensity passing through the diaphragm (I out-coupled) versus the light intensity inside the waveguide (I in-coupled).

4.2.6 Nonlinear coefficients

The measurement of nonlinear coefficients in the surface of a waveguide was first implemented in our laboratory by Joaquín Rams [175, 180]. The main goal of this technique is the finding of a configuration where no contribution from the substrate to the nonlinearity is taken into account, as it occurs with methods often used in bulk, such as Maker fringes, which are not suitable for waveguides. The approach of measuring the second harmonic generation in the strong absorption regime was found very convenient for the study of thin layers, even thinner than the waveguides themselves.

Even though the experimental setup will be thoroughly presented in chapter 5, a brief description could be the following: A light beam of $532\,\mathrm{nm}$ from a pulsed doubled Nd:YAG (Quanta-Ray GRC-130 model, from Spectra Physics) hits the surface of the sample and is transmitted through it. The second harmonic $266\,\mathrm{nm}$ light generated in the crystal lies deep inside the ultraviolet absorption band of $LiNbO_3$, and is therefore strongly absorbed. Just the light generated in a very thin layer ($\sim 40\,\mathrm{nm}$ depth) avoids being absorbed and can escape from the crystal in the same direction as the incident beam. As the ultraviolet light intensity is $\sim 10^{-9}$ times smaller than the fundamental beam, two *Pellin Broca*

dispersive prisms are used to separate them. After a selective mirror which reflects the remaining green light, the UV light intensity is recoiled in an AsGa In photomultiplier (Hamamatsu R 2658P) connected to an oscilloscope (Tektronik TDS 520 A). In figure 4.14 an actual measurement of the second harmonic generated intensity in a Zn-in-diffused waveguide, compared to the intensity generated by a bulk sample can be seen.

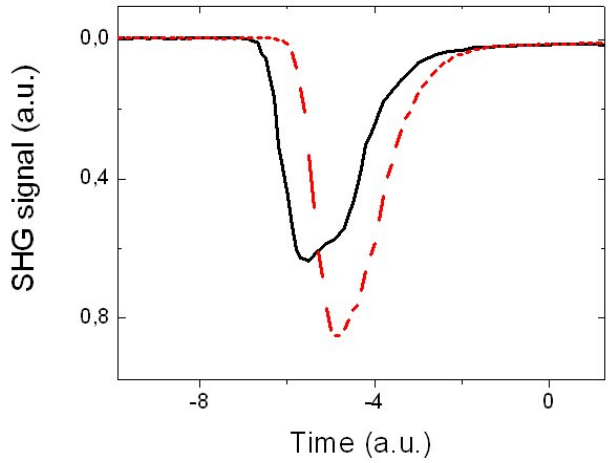

Figure 4.14: Light intensity of ultraviolet light detected by the photomultiplier for both a waveguide (solid curve) and a $LiNbO_3$ congruent substrate (dashed curve) as it is seen in the oscilloscope.

The second harmonic intensity measured is proportional to $(d_{ij}/\alpha)^2$, being d_{ij} the nonlinear coefficient and α the absorption coefficient for this wavelength [128]. If α is assumed to be similar in the waveguide and in $LiNbO_3$, and a bare $LiNbO_3$ substrate is measured in the same way than the sample, the relative nonlinear coefficient can be obtained. Moreover, the value of different components of the nonlinear tensor d_{ij} can be obtained by changing the polarization of the beam before reaching the sample, for the incident field, and before the photomultiplier, for the generated field.

4.3 Periodic polarization techniques

At the beginning of this work, periodically poled $LiNbO_3$ crystals grown in the Crystal Growth Laboratory of the U. A. M. were used. After some trials, it was found necessary to go to smaller periods and to pole the crystals once the waveguide was made. For those reasons, electric field polarization was finally used. In this section, both polarization techniques will be described.

4.3.1 Offcenter Czochralski technique

The off-center Czochralski method was already described in the introduction chapter (1.2.4). In this work, Er:PPLN, Yb:PPLN and Nd:PPLN samples grown by the Crystal Growth Laboratory of the U.A.M., were studied. The melts used were composed of the congruent $LiNbO_3$ melt and one of the above mentioned impurities (and Mg in some cases) in the form of oxides. Their concentrations were 0.7 - 0.4 mol% for Er, and 0.7 mol% for Yb and Nd. The crystals were grown along the **x**-axis. The pulling and rotation rates were $\sim 2\,\mathrm{mm/h}$ and $\sim 10\,\mathrm{r.p.m.}$

Once the crystals were grown, the samples were cut and polished up to optical grade as described before in section 4.1.5.

4.3.2 Electric periodic poling

This technique, also detailed in 1.2.4, was in our case applied to bare congruent single domain $LiNbO_3$ substrates, z-cut, 0.5 mm thick, and afterwards, to proton exchanged waveguide samples, made on the same kind of substrates. In all the steps that will be described below, cleanness of the sample was essential.

Lithographic masks

To periodically pole the samples it is necessary to have periodic electrodes in one of the faces of the sample and a planar electrode. In order to fabricate electrodes with widths of micrometers, photolithographic techniques, already described in section 4.1.4, were used. At difference with the channel mask fabrication, in the electrode fabrication no SiO_2 was used, only photoresist. One surface of the sample was covered with positive photoresist (Microposit S1813), that was exposed to ultraviolet light through a photolithographic mask with hollow stripes of half the desired period. On the substrates with planar α-phase waveguide in +**z** or -**z** face, the resist pattern was fabricated in the same face as the waveguide. After photolithography, the samples were post-baked to enhance the photoresist dielectric strength.

The photoresist acts as an insulator and the free spaces between the resist stripes act as the electrodes, contacted with the LiCl solution. In the first trials, metals were evaporated once the periodic resist structure was made, to make a better contact between the liquid electrode and the sample in the gaps with no photoresist. This additional step made the preparation process rather cumbersome, and it was found sufficient to have just the resist pattern to achieve good periodic poling of the samples.

Additional care has to be taken once the resist is patterned, specially with the cleaning of the samples. It was important to avoid any dust before high voltage was applied. As no acetone could be used, because it erased the resist, the samples were cleaned with pressurized air.

Poling chamber

To apply the high electric field necessary to achieve the domain inversion, a Plexiglass chamber was designed, based on the ones used for electric poling [153, 130, 197], but adapted to hold samples of the small sizes of our waveguides (Figure 4.15). Two quartz windows were placed in both sides of the chamber to allow direct visualization of the poled area without disarranging the setup. The high voltage is applied to the sample through liquid electrodes (water saturated with LiCl).

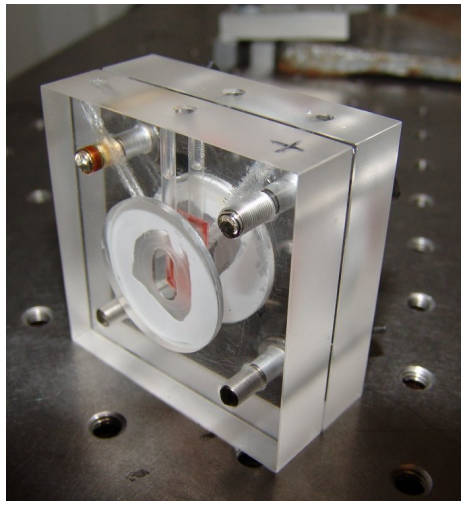

Figure 4.15: Poling chamber used in the experiments.

Both sides of the chamber were adjoined to the sample with silicon o-rings in order to isolate both faces of the sample and avoid any leakages. One had to be careful with the pressure of this o-rings, because if it is not homogeneous or if it is too high, the sample broke easily. Another important feature that was taken into account, were the bubbles. A few minor adjustments were made to the chamber design in order to get rid of most of them. That was important because they had two adverse effects on the experiment: First, they were responsible for several breaks during

the poling process. Secondly, given that our samples were rather small, we had a clear limit on the area which could be poled, and the presence of bubbles prevented a fraction of the surface to be contacted with the liquid electrodes and the poled area was even more reduced.

Poling circuit

The first experiments were done with voltage ramps in no structured samples, that is, with no photolithographic electrodes, in order to find the actual coercive field of the samples. To know the voltage at which the poling began, the current produced in the process was monitored in a oscilloscope. Once the samples were poled and re-poled without problems, the conventional electric field poling technique [157, 219] with high voltage pulses was studied and adapted to the poling of our waveguides. The circuit that has been used can be seen in figure 4.16. The high voltage waveform´s shapes are generated with a function generator (DS354, Standford Research Systems) and amplified with a voltage amplifier (20/20C-L, TRek). The intensity current produced in the poling process is registered with an oscilloscope, which in turn gives information about how much area of the sample has been poled by the relation 4.2

$$Q = \int i dt = 2P_s A \tag{4.2}$$

where Q is the charge, A the area of domain reversal, 2 accounts for the polarity reversal and $P_s \sim 0.71\,\mathrm{Cm}^{-2}$ [235] or $78\,\mu\mathrm{C/cm}^2$ [148] is the spontaneous polarization of $LiNbO_3$ [235].

It was found that a good control in the pulse intensity and duration was quite critical in order to obtain homogeneously poled samples. The final chosen pulse shapes can be described as follows: a first stage consisted

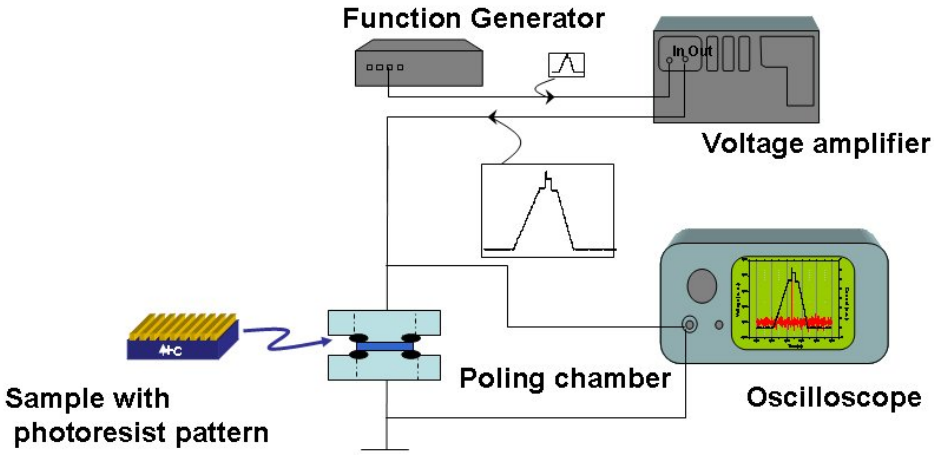

Figure 4.16: The poling circuit: The voltage waveform is generated in the function generator, then amplified and applied to the structured sample. Both the actual voltage pulse and the produced current through the sample are monitored in an oscilloscope.

on a ramp which was increased until it reached a certain value under the coercive field. This was maintained for a while (second stage) and then the field was risen far above the coercive field for one or two milliseconds, to start the nucleation of the domains in the areas where there was no photoresist (third stage). Then, it was decreased for some milliseconds to a value just above the coercive field to let the domain seeds grow and join each other under these regions (fourth stage). The next step consisted on maintaining the value of the applied field just below the coercive field to stabilize the domain structure (fifth stage). After that, the field was decreased down to 0 V/mm (sixth stage) [19]. The implications of the pulse waveform will be discussed later along with the results on the periodic poling of $LiNbO_3$ waveguides and substrates (chapter 6.2.4).

4.3.3 Ferroelectric domain characterization

Crossed Polarizors

The most straightforward technique that was used to visualize whether there was a domain pattern in the sample, apart from detecting the current produced in the process, was the visualization of the sample under crossed polarizers, also referred as the Miller and Savage technique [147]. The domain walls, due to the birrefringence induced by the residual strains in them, can be seen with transmitted light (see figure 4.17).

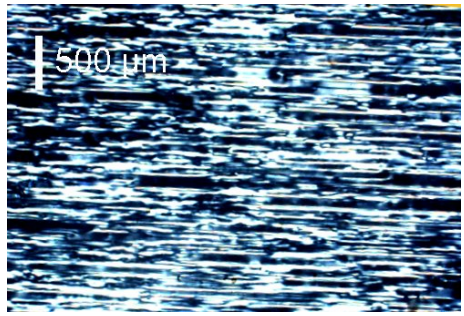

Figure 4.17: Microscope image of an α-phase PE waveguide after periodically poling, with crossed polarizers

Diffraction by the domain walls

Another characterization technique used in this work to visualize the domain pattern in the waveguide was diffraction by the domain walls. This technique has been used for characterizing bulk PPLN samples [30, 154], but in our case a waveguide is present and only guided light is used. As it can be seen in figure 4.18, extraordinary polarized light was coupled into the waveguide with a rutile prism, propagated in the y-direction, and then decoupled with another rutile prism. Bright modes

and their diffraction orders were observed in a white screen. The main advantage of this technique, apart from being not destructive, is that it characterizes the structure within the waveguide, not in the whole bulk as the previous one.

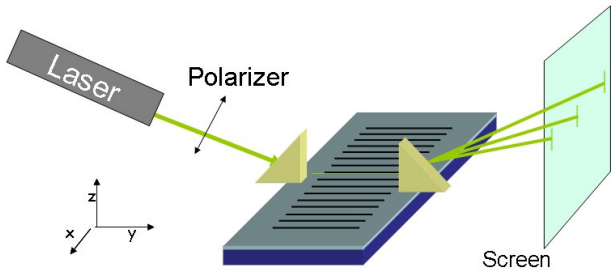

Figure 4.18: Experimental setup for the visualization of bright modes of a waveguide diffracted by the domain walls.

Nevertheless, it cannot be used alone, because it gives no detailed information about the quality of the domains, unless it is combined with an external field to extract information about the duty cycle (D.C.) [122]. In our case, it was not experimentally possible to find a way of applying an external field and guide light in the waveguide at the same time.

Chemical etching

The most straightforward characterization technique, namely selective chemical etching [25], was used to make a study of the quality of the preliminary samples. First of all, the photoresist pattern was cleaned from the sample with acetone. Then the samples were immersed in hydrofluoric acid (HF) or HF:HNO_3 (1:2 by volume) at room temperature for 10 to 30 minutes to etch the **z**-face, or 1 hour to etch the **y**-face. (Even etching times as long as 9 hours were used to study the in-depth structure of the domains) [50, 82] As a result of the different etch rates of the negative (much faster)

and the positive **z** faces of $LiNbO_3$, the resulting topography was observed directly with an optical microscope. To be sure that the etching process did not destroy the whole waveguide structure, OH spectra of planar waveguides, already explained in section 4.2.3, after etching processes were taken. It was found that, for the times used in the experiment, the domain pattern revealed after the etching process lied on the waveguide layer.

The main drawback of this method is that it destroys at least the first $50\,\mathrm{nm}$ of the etched face, and the waveguide is not suitable because of the roughness of the surface, unless it is polished after it. But if done so, the effective thickness of the waveguide would be reduced, giving rise to a shallow structure with different guiding properties than the original one. To avoid this inconvenience, once the electrical poling set-up was optimized and good quality domain patterns obtained, the samples were cut in two equal pieces along the **x** axis with a diamond saw. One of the pieces was kept to repeat the optical characterization previously made of the waveguide, but this time after the electrical poling, and to be used in further experiments. The other piece was optical-grade polished along the **y**-face. Then it was etched for 1 hour in HF:HNO_3 in order to reveal the domain pattern not only in the surface, that is, **z**-faces, but also the in-depth development of the domains in the waveguide layer and in the whole substrate as well.

Part III

Results

Results:

Results:

Chapter 5
Second order susceptibilities of $LiNbO_3$ waveguides

Second order susceptibilities of $LiNbO_3$ waveguides

Throughout this chapter the nonlinear coefficients of different $LiNbO_3$ waveguides will be presented. Given that the objective of this Thesis work is to carry out a study on the nonlinear characteristics of a variety of $LiNbO_3$ waveguides, the actual measurement of how the waveguide fabrication itself has affected the nonlinear coefficients of $LiNbO_3$ is a very important issue. In most cases, these second order nonlinear capabilities were not measured before. In order to know which waveguides are the most suitable for efficient frequency conversion, not only these coefficients have to be taken into account, but their measurement will provide a good starting point to evaluate different waveguides.

The measurement of the nonlinear coefficients in $LiNbO_3$ waveguides is not a simple task. The main problem arises from the nonlinear contribution of the substrate, which is very high, and has to be separated from the nonlinear signal generated in the waveguide. There are mainly three techniques to evaluate the nonlinear coefficients in waveguides: Cerenkov method, quasi-phase-matching in waveguides and SHG in the strong absorption regime.

In the first one, the fundamental wavelength is guided and the second

harmonic radiation created by the nonlinear polarization is radiated into the substrate at an angle that preserves k vector component parallel to the interface, providing automatically phase matching. This is caused by the different phase velocities of the nonlinear polarization with respect to the propagating fundamental light. This configuration receives the name of *Cerenkov configuration*. From this second harmonic generated light, the Cerenkov method provides information about the nonlinear coefficients of the waveguide. The problem arises from the reliability of these data, because the technique is very sensitive to the waveguide depth and refractive index profile shape [208]. With this method, a reduction of the nonlinear coefficients of $50 - 70\%$ for PE waveguides has been reported [131]

The second technique does give information about the nonlinear coefficients of the waveguide layer, but in a qualitative way. From the second harmonic generation efficiency one can know whether the waveguide fabrication has decreased the nonlinear properties of the substrate or not. But the efficiency of second harmonic generation depends on so many variables, that one has to take into account not only the nonlinear coefficients, but also the domain structure irregularities, the overlap between the fundamental and second harmonic waveguide modes, etc. Then, it is hardly possible to obtain an objective evaluation of the nonlinear coefficients of different waveguides with this method [217, 54].

In this chapter, a third approach to the measurement of the nonlinear coefficients is going to be used. The technique, known as the *Second Harmonic Generation in the Strong Absorption Regime* [180] and already described in section 4.2.6, is based in the study of the second harmonic generation in the surface, where the waveguide lies. The main feature of this method is that the second harmonic generated light lies deep inside the absorption band of $LiNbO_3$. Then, only the light which is generated

in the outer layer of the material, that is, in a very thin layer within the waveguide near the surface ($\sim 40nm$ depth), can avoid being absorbed (see figure 5.1) and the contribution of the substrate to the second harmonic is completely avoided. This technique has been used throughout this work to characterize the nonlinear coefficients of the different waveguides, in order to optimize the fabrication techniques. Therefore, in this chapter, after a deeper insight to the measurement configurations, a systematical study on different waveguides will be presented. Firstly, sections 5.2 will be focused in the different proton exchanged pure phases, then metal in-diffused waveguides (Ti and Zn-in-diffused) will be studied (section 5.3 to finish with different irradiated waveguides (section 5.4.

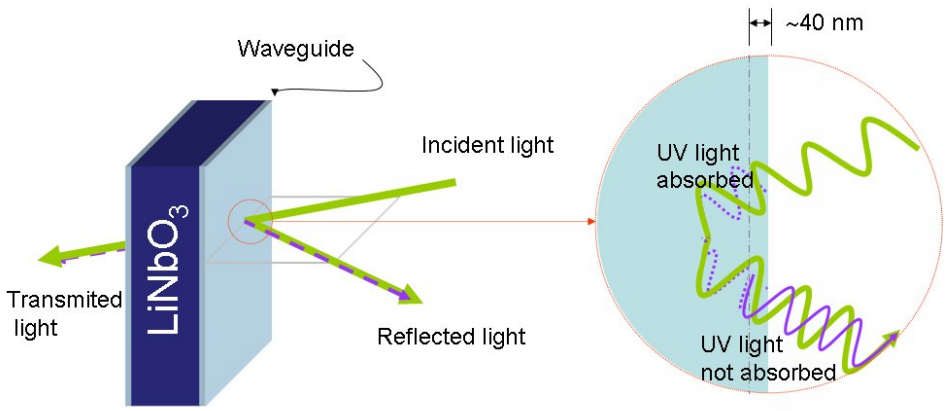

Figure 5.1: Ultraviolet second harmonic light is generated in the sample, but as it is strongly absorbed by the material, only the ultraviolet light generated in the very last layer of the material avoids being absorbed. Note that for the transmitted beam, the second harmonic generated light is analogous.

5.1 Measurement configuration

The experimental setup of nonlinear coefficients in the strong absorption regime was briefly described in chapter II. In this section, the different measurement configurations used will be detailed.

First of all, the tensorial nature of the nonlinear coefficients has to be pointed out. From equation 2.1, and taking into account that $d^{(2)}_{ijkl} \equiv \frac{1}{2}\chi^{(2)}_{ijkl}$, the second order nonlinear term becomes

$$P_i(2\omega) = 2d_{ijk}E_j(\omega)E_k(\omega) \tag{5.1}$$

This equation can be also written in matrix notation. Using the contracted d_{ij} nonlinear tensor for $LiNbO_3$ (see equation 2.2),it writes:

$$\begin{pmatrix} P_x^{2\omega} \\ P_y^{2\omega} \\ P_z^{2\omega} \end{pmatrix} = \begin{pmatrix} 0 & 0 & 0 & 0 & d_{51} & -d_{22} \\ -d_{22} & d_{22} & 0 & d_{51} & 0 & 0 \\ d_{13} & d_{13} & d_{33} & 0 & 0 & 0 \end{pmatrix} \begin{pmatrix} E_x^2(\omega) \\ E_y^2(\omega) \\ E_z^2(\omega) \\ 2E_y(\omega)E_z(\omega) \\ 2E_x(\omega)E_z(\omega) \\ 2E_x(\omega)E_y(\omega) \end{pmatrix} \tag{5.2}$$

Then, the expression for each of the polarization components can be written as

$$\begin{aligned} P_x^{2\omega} &= 2d_{15}E_x(\omega)E_z(\omega) - 2d_{22}E_x(\omega)E_y(\omega) \\ P_y^{2\omega} &= d_{22}[E_y^2(\omega) - E_x^2(\omega)] + 2d_{15}E_y(\omega)E_z(\omega) \\ P_z^{2\omega} &= d_{31}[E_x^2(\omega) + E_y^2(\omega)] + d_{33}E_z^2(\omega) \end{aligned} \tag{5.3}$$

With the experimental setup of SHG in the strong absorption regime,

the magnitude measured is the intensity of the generated ultraviolet light ($266\,\mathrm{nm}$) that escapes from the crystal, which is proportional to the square of $P^{2\omega}$ ($I(2\omega) \propto P^{2\omega}$). Then, in order to separate the different nonlinear coefficients in the experiment, one can change the propagation direction, the input polarization of the light and the output polarization detected. The different measurement configurations for each nonlinear coefficient, are shown in table 5.1

Propagation	Incident polarization	Output polarization	d_{ij}
$\|\| x-axis$	$\|\| y-axis \quad (E_z = 0)$	$\|\| y-axis \quad I(2\omega) \propto d_{22}^2 \lvert E_y\rvert^4$	d_{22}
		$\|\| z-axis \quad I(2\omega) \propto d_{31}^2 \lvert E_y\rvert^4$	d_{31}
	$\|\| z-axis \quad (E_y = 0)$	$\|\| y-axis \quad I(2\omega) \propto 0$	$-$
		$\|\| z-axis \quad I(2\omega) \propto d_{33}^2 \lvert E_z\rvert^4$	d_{33}
$\|\| y-axis$	$\|\| x-axis \quad (E_z = 0)$	$\|\| x-axis \quad I(2\omega) \propto 0$	$-$
		$\|\| z-axis \quad I(2\omega) \propto d_{33}^2 \lvert E_z\rvert^4$	d_{33}
	$\|\| z-axis \quad (E_y = 0)$	$\|\| x-axis \quad I(2\omega) \propto 0$	$-$
		$\|\| z-axis \quad I(2\omega) \propto d_{33}^2 \lvert E_z\rvert^4$	d_{33}
$\|\| z-axis$	$\|\| x-axis \quad (E_y = 0)$	$\|\| x-axis \quad I(2\omega) \propto 0$	$-$
		$\|\| y-axis \quad I(2\omega) \propto d_{22}^2 \lvert E_x\rvert^4$	d_{22}
	$\|\| y-axis \quad (E_x = 0)$	$\|\| x-axis \quad I(2\omega) \propto 0$	$-$
		$\|\| y-axis \quad I(2\omega) \propto d_{22}^2 \lvert E_y\rvert^4$	d_{22}

Table 5.1: Different configurations in order to measure the different nonlinear coefficients of the waveguides

Given these relations, it is easy to see that, once the input and output polarizations have been properly chosen, from the comparison between substrate and waveguide second harmonic generations, one gets

$$\left(\frac{d_{ij}^s}{d_{ij}^g}\right)^2 \propto \left(\frac{I^s(2\omega)(I^g(\omega))^2}{I^g(2\omega)(I^s(\omega))^2}\right) \tag{5.4}$$

where d_{ij}^s, d_{ij}^g are the corresponding nonlinear coefficients for the substrate and waveguide, respectively, and I^s, I^g are the intensities ($|E|^2$)

for each case. Taking all of this into account, it is possible to obtain the relative nonlinear coefficients of the different waveguides compared to bare $LiNbO_3$. The values of the d_{ij} coefficients for congruent $LiNbO_3$ are the following:

d_{33}	$d_{31} = d_{15}$	d_{22}
$34.4\,\mathrm{pm/V}$	$5.95\,\mathrm{pm/V}$	$3.07\,\mathrm{pm/V}$

Table 5.2: Nonlinear coefficients of congruent $LiNbO_3$ (values provided by Photox Optical Systems. See also table 5.1)

In the actual experiment, the measured second harmonic light is recoiled in transmitted or reflected configurations (see figure 5.2). In both cases, the incident light can propagate normal to the waveguide surface or with a certain angle, being the intensity of second harmonic generated light slightly higher in transmission configuration than in reflection [180]. Anyhow, if light propagates normal to the surface, the equations mentioned above are valid. But if the incident angle is different from $0°$, the equations should be modified to take into account that the incident electric field will have components in more than one direction. In the case of the waveguides studied in this work, they have basically two different geometries, that is, some of them were fabricated on x-cut and others on z-cut substrates. From table 5.1 it is easy to see that, if the substrate is x-cut and the incident beam is normal to the surface (propagation in the x-axis), and polarized along the **z** direction, the second harmonic light intensity generated depends on d_{33} alone, which is the highest one. Then, in both transmission and reflection configurations, the signals obtained were enough to accomplish the measurements.

In the case of waveguides fabricated on z-cut substrates, if the incident beam travels normal to the surface, that is, along the **z** direction, for any polarization of this incoming light, the second harmonic generated light

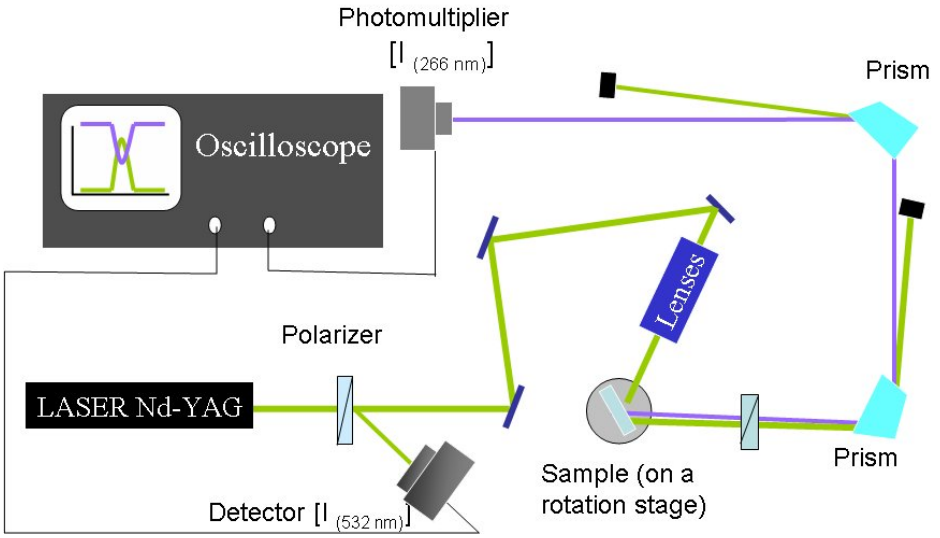

Figure 5.2: Brief scheme of the reflection configuration setup. To make measurements in transmission, the first mirror is put aside and the lenses system is moved to that place, remaining all the rest exactly the same.

depends on the value of the d_{22} coefficient, which for bare $LiNbO_3$ is approximately 10% of d_{33} (see table 5.2). Being the second harmonic light deep inside the absorption band of $LiNbO_3$, the intensity that escapes the crystal corresponds to light generated in the last $40\,\mathrm{nm}$, and this is a very tiny signal. If this is combined with the fact that the nonlinear coefficients are usually lower in waveguides than in bulk $LiNbO_3$, we obtain a second harmonic generated intensity in most cases too low to be detected. To have a noticeable signal, the samples were rotated a certain angle in such a way that some of the incident electromagnetic field propagated along the **z** direction. Then, the second harmonic light generated due to the d_{33} coefficient is much higher than in the case of normal propagation.

Note that the d_{22} contribution in this new orientation decreases, at the same time that the contribution from the d_{33} coefficient increases. And if with normal incidence, second harmonic light generated due to d_{22} was

not distinguishable, in this arrangement its contribution is negligible. The most important thing is that the waveguide and the $LiNbO_3$ substrate used for comparison are placed at the same angles with respect to the incident light. To achieve a good repetitiveness, the samples were mounted on a rotatory platform, with an angular resolution of $0.01°$. In the case of z-cut samples, they were rotated to the Brewster angle when measuring in transmission configuration, because this is a very repetitive angle. In reflection configuration, as the Brewster angle cannot be used, an arbitrary $42°$ angle was chosen.

5.2 Proton exchange waveguides

At the beginning of the discovery of the proton exchange waveguide technique, they were really appealing for nonlinear generation. The main cause is that the fabrication lowers the ordinary index and increases the extraordinary index, as it was mentioned before, allowing a better control over the phase-matching condition. The first experiments on second harmonic generation were made with the Cerenkov method, and later on, quasi-phase-matching was performed in waveguides fabricated on periodically poled substrates [134, 53, 36]. In any case, the measurement of the actual nonlinear coefficients in the waveguide remained an issue, because they were known to be lower than in bulk but their values differed a lot, from groups which claimed a 50% reduction in PE waveguides [204] to others which ascerted a total erasure of the nonlinear properties of the material after PE waveguide fabrication [113]. Finally, measurements in reflection configuration were made, to avoid any influence from the substrate, and a reduction of 3% in their values was obtained. The main problem with all these measurements is that the PE waveguide fabrication methods varied from one group to the others, and the crystallographic

phase obtained were not specified.

At difference with previous works, here all the measurements of the nonlinear coefficients have been made with the same technique (SHG in the strong absorption regime). A preliminary study of different Proton Exchange waveguides was performed by Joaquin Rams *et al.* [175, 180] at the starting point of PE waveguide fabrication in the Nonlinear Optics Laboratory in the U.A.M. Nowadays, the fabrication methods of the different waveguide phases have changed to optimize their quality and homogeneity (samples were of $5 \times 10 \times 1\ \mathrm{mm}^3$ and presently homogeneous samples of larger areas are achieved). Therefore, an updated investigation of their real nonlinear coefficients was necessary. This study has been achieved for α, β-phases, *vapor* and *reverse* proton exchange waveguides, to determine which among them are more suitable for nonlinear frequency conversion.

5.2.1 α-phase proton exchange waveguides

Different α-phase PE waveguides were studied. All these samples were made by immersion in benzoic acid buffered with 3% lithium benzoate, at $300^\circ\,\mathrm{C}$. The objective of these measurements was to find out whether the exchange process affected the nonlinear coefficient. Therefore, the fabrication process of the different samples was the same except from the exchange time, which was changed from 8 to 25 hours. The measurements were carried in transmission configuration, and in the case of waveguides fabricated in **z**-cut, an incident angle of 45° was used.

The preserved nonlinear coefficient d_{33} with respect to congruent $LiNbO_3$ for α-phase PE waveguides are presented in figure 5.3. There, it can be seen that for waveguides fabricated on z-cut substrates, the nonlinear coefficients appear to be around 75% of bare $LiNbO_3$. In the

case of waveguides on x-cut substrates, the nonlinear coefficients were approximately 90% of $LiNbO_3$.

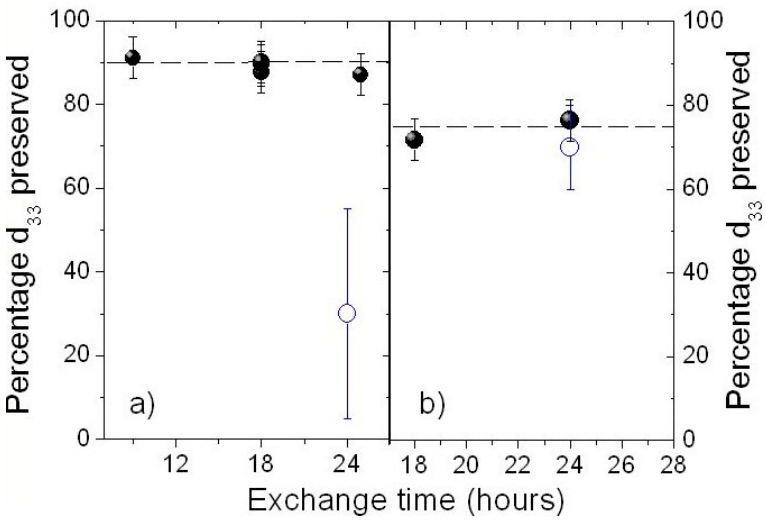

Figure 5.3: Percentage of the nonlinear coefficient d_{33} of $LiNbO_3$ preserved after α-phase waveguide fabrication on a) x and b) z-cut substrates, depending on the exchange time (black circles). The values obtained by Rams are also plotted (open circles) for comparison [175].

In literature abound *soft proton exchanged* or *annealed proton exchanged* waveguides used for frequency conversion devices, which indicates that their second order nonlinear coefficient must be high. These waveguides consist on a mixture of phases, being the most relevant the α-phase. In figure 5.3 only pure α-phase waveguides are shown. Also the results obtained by J. Rams *et al.* are plotted. In the case of waveguides fabricated in x-cut substrates, the preservation of the second order nonlinear coefficient measured by Rams is around 30% of the substrates value, whereas the preservation measured in our case is around 90%. It is important to indicate that the value plotted here is the one measured for one waveguide fabricated by immersion of the sample in a melt composed of benzoic acid and lithium benzoate, at the early stages

of PE-waveguide fabrication in our laboratory. But the technique has improved ever since, and the repetitiviness of the results obtained now make us think that this 90% value is more consistent. Moreover, there are also measurements carried out by Rams in α-phase waveguides fabricated not by immersion but by vapour proton exchange, which show a preserved nonlinear coefficient of around 100%, in good agreement with our results [175, 180]. As far as the waveguides fabricated in z-cut substrates are concerned, the obtained value is in very good agreement with the one measured by Rams for a sample of $24\,\mathrm{hours}$ exchange time.

The fabrication parameter that has been studied, that is, exchange time, does not seem to affect the nonlinear coefficient of the samples (see figure 5.3). Anyhow, in the chapter devoted to optical damage (chapter cap:danno) it will be shown that the study of the influence of the exchange time in the waveguide properties is quite interesting, because it actually affects the photorefractive properties of these waveguides [57]. Although a similar influence of the exchange times on the nonlinear coefficient was quite improbable, it was worth to confirm it.

One possible explanation for the decrease of the nonlinear coefficient in PE waveguides is the depolarization of $LiNbO_3$. If this is correct, other properties which are affected by the polarization of the sample, should be also affected. One of these polarization dependent properties is the electro-optic effect. Actually, the measured value of the electro-optic coefficient for α-phase PE waveguides is $70 - 95\%$ the value of the substrate [144, 145]. This suggests the electro-optic effect, as well as the second order nonlinearity, are affected by the depolarization of $LiNbO_3$ due to the slight symmetry change in the waveguide.

The main novelty of these measurements is that they have been obtained for pure α phases and that the technique allows a thorough study of how different processes or variations in the fabrication technique affect

the nonlinear properties of the waveguides.

5.2.2 Vapor proton exchange waveguides

One of the most interesting features of optical waveguides is the confinement of light. This confinement is better when the index profile is step-shaped, but in the case of α-phase waveguides, the index profile is rather smooth. Better confinement is provided by β-phase PE waveguides, but in these waveguides the nonlinearity of the $LiNbO_3$ substrate is almost completely lost. For example, there could not be found any signal of second harmonic light, thus the nonlinear coefficients are completely erased. In this work, several β-phase waveguides were measured. They were fabricated by immersion in a melt of benzoic acid and $1\%\,\mathrm{molar}$ lithium benzoate, at $300^\circ\,\mathrm{C}$, and even though the exchange times varied from $30\,\mathrm{minutes}$ to $46\,\mathrm{hours}$ and x-cut and z-cut substrates were used, no ultraviolet light was detected.

There is a different kind of waveguides, namely *Vapor Proton Exchange* (VPE) waveguides, which have the same step index profile that β-phase waveguides. Rams *et al.* [175] found some promising results in this kind of waveguides, showing that the proton exchange in the vapor phase the fabrication method does not remove completely the nonlinear coefficients. But in that study, the homogeneity of the samples and their too small sizes (around $5 \times 5 \times 1\,\mathrm{mm}^3$) made them useless for practical applications. Therefore, the main objective of the work presented in this section was to improve the homogeneity and to obtain the highest possible nonlinear coefficients in bigger samples.

These waveguides are not fabricated by immersion of the sample in a melt. Instead of that, the ampoule is not rotated and the vapours comming from the melt reach the substrate, and the proton exchange is produced.

In the fabrication process, a double oven was used, that is, an oven where the region of the melt was kept at a different temperature than the sample. This is necessary to warranty a constant vapour flux in order to achieve better homogeneity. A number of experiments were made, varying the two temperatures of the oven, the composition of the melt and the exchange times. The best results were found for temperatures of 305° C for the melt and 300° C for the sample, and pure benzoic acid as proton source. Among these samples, the exchange time was varied between 4 and 24 hours.

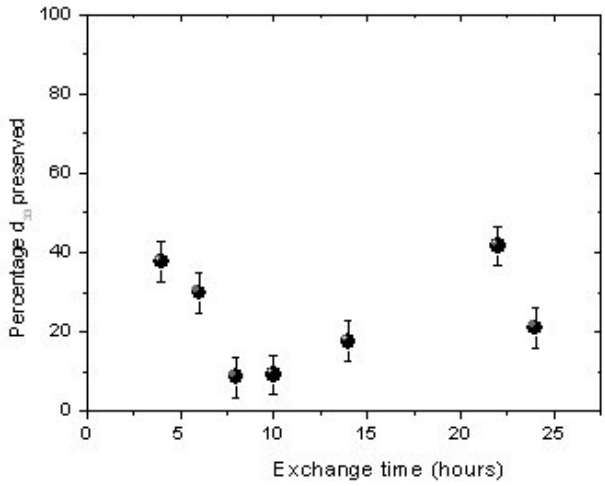

Figure 5.4: Percentage of the nonlinear coefficient d_{33} of $LiNbO_3$ preserved after Vapor Proton Exchange waveguide fabrication for different times.

In figure 5.4, the percentage of nonlinear coefficient preserved with respect to congruent $LiNbO_3$ in samples with different exchange times can be seen. The value of the nonlinear coefficient preserved is quite reasonable for practical applications in some samples, being around 40% of congruent $LiNbO_3$. The nonlinear coefficient is plotted versus exchange time because this was the fabrication parameter that was varied in order

to find some kind of trend or behaviour that helped us to fabricate in a repetitive way VPE-waveguides with high nonlinear coefficients. But in figure 5.4 there can also be seen that the variation on the nonlinear coefficient with the exchange time does not seem to have a clear trend. For those samples with exchange times of less than 10 hours, the nonlinear coefficient seems to decrease with the exchange time, but these waveguides are very thin ($1-2\,\mu\mathrm{m}$ effective depht). Then, for samples fabricated with times longer than 10 hours, there is no clear trend. Moreover, the effective depth and index change were also measured for each of those samples, and they both increase with the exchange time, as it is expected in usual PE processes, giving us no further clue of why for a 22 hours treatment a 40% preservation of the nonlinear coefficient was obtained.

To sum up, VPE waveguides fabricated with the two zone temperature oven present a second order nonlinear coefficient preservation of around 40% for certain exchange times, but the actual change of this parameter with the exchange time is not understood yet. Moreover, the repetitiveness in the fabrication of these VPE waveguides is very poor, because of the many parameters involved, which are not controlled yet. In order to make these samples competitive with α-phase waveguides or others with high nonlinear coefficients, a deeper study on the fabrication processes should be performed to be able to obtain higher nonlinear coefficients in a repetitive way.

5.2.3 Reverse proton exchange waveguides

In this work, *Reversed Proton Exchanged* (RPE) waveguides were also characterized with this technique. These waveguides are fabricated in a two step process, being the first one a proton exchange treatment by immersion of the sample in an acid melt, and the second, the so-called

reverse treatment, the immersion in a Li^+ rich melt to recover more or less the structure of $LiNbO_3$. The fabrication parameters can be seen in table 4.1. This process gives rise to an outer layer where the ordinary index is increased and the extraordinary index decreased, with respect to the previous proton-exchange waveguide. Therefore, in the outer layer only ordinary polarized light can be guided, being the guiding layer the reversed region, the substrate the remaining proton exchange waveguide and the cover, air. This structures are most often used to *bury* the first proton exchange waveguide, being for this layer only extraordinary polarized light guided and both substrate and cover, $LiNbO_3$[169, 86]. In these works, the buried waveguides were annealed PE or soft PE, which are processes that do not erase the nonlinear coefficients.

In the case of the SHG in the strong absorption regime technique, the outer layer is measured. The aim of the measurement of nonlinear coefficients in this layer was to study how after a β-phase waveguide fabrication, the reverse treatment produced a recovery of the nonlinear coefficients. Therefore, the buried waveguide in our case has erased completely the nonlinear coefficients. The result was that, in the reversed layer and for the treatment mentioned before, a preservation of $70 \pm 10\%$ of the coefficients with respect to congruent $LiNbO_3$ was found.

Although the result obtained is very promising, the problem is that only ordinary light can be guided. Then, in table 5.1 the possible configurations for guided light generation show that if light is polarized along **x** direction, no generation is possible. In the case of light polarized along **y** direction, only d_{22} plays a role in the nonlinear generation, and as it was shown in table 5.2, its value is around 10% of d_{33}, which makes these waveguides less suitable for nonlinear frequency conversion than α-phase PE waveguides or any others, where the nonlinear coefficient involved in the frequency conversion processes is d_{33} and its value is over

10% of congruent $LiNbO_3$.

5.3 Metal in-diffused waveguides

Once the nonlinear coefficients measurement technique was implemented again in the Nonlinear Optics Laboratory, the characterization of other kinds of waveguides, namely titanium and zinc in-diffused was performed. The first ones were fabricated in our laboratory (see section 4.1.2) in order to compare them with other waveguide fabrication methods. In all cases measured, the values of d_{33} obtained were the same as in pure congruent $LiNbO_3$, which is in good accordance with literature, where their nonlinear coefficient values is usually considered as 100% of the substrate's [41, 112, 192].

In the case of Zn:$LiNbO_3$ waveguides (see also section 4.1.2), the AMIGO group provided us several samples, on x and z-cut substrates ($\sim 4\,\mu\mathrm{m}$ effective depth, $\Delta n_o \sim 0.005$, $\Delta n_e \sim 0.007$). In figure 5.5, the measurement of the nonlinear coefficients can be seen. The graphic shows that the nonlinear coefficients of these samples are almost undistorted after the waveguide fabrication process. In this graph, the dispersion of the data is quite noticeable, even though the fabrication process was the same in all cases. Moreover, the same samples were measured more than once, with different results. This may be caused because, after the diffusion of zinc, the surface is a little damaged and also remains of the metal form ZnO on the surface and it has to be polished. This was made by hand and it probably made the surface quite inhomogeneous. Given that our technique is very sensitive to the roughness of the sample, this may affect the measurements.

In these samples the electro-optic coefficients were also measured, and

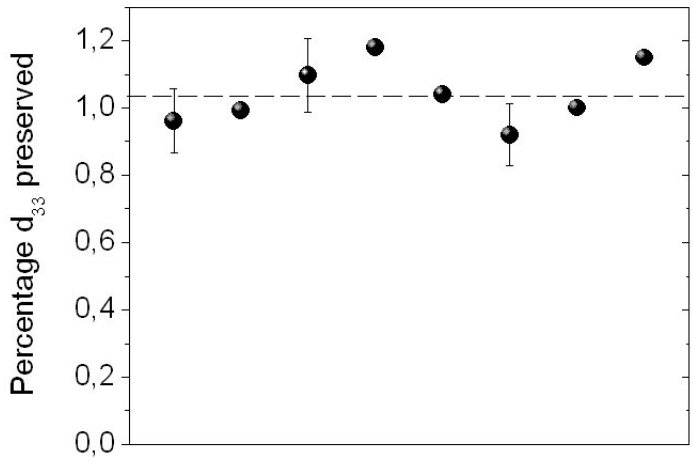

Figure 5.5: Percentage of the preserved nonlinear coefficient d_{33} (measured in transmission and reflection geometries) of Zn-in-diffused waveguides, fabricated in **x** and **z** faces of congruent $LiNbO_3$ substrates.

the values obtained ($r_{33} = 14.6 \pm 0.9$ and $r_{13} = 3.3 \pm 0.2$) present a decrease with respect to bulk $LiNbO_3$ of 50% in the case of r_{33} and 70% for r_{13}. This reduction is in good agreement with the one shown in $LiNbO_3$ crystals doped with Zn concentrations of the order of 2% molar [1], which is the estimated concentration of Zn in these waveguides. The explanation given for this effect is that the concentration of Li vacancies decreases with the incorporation of Zn (which takes Li positions). These reduction of the electro-optic coefficient may seem contradictory with the fact that the second order susceptibility does not appear to be affected in Zn-in-diffused waveguides. But this effect could be understood as follows. Zn impurities mainly affect the nonlinear response at very low frequencies, where the crystal lattice contribution is relevant. For higher frequencies, within the optical range ($\sim 10^{15}$ Hz) the nonlinear response is little altered. In any case, these waveguides have proved a high efficient nonlinear conversion [50, 52].

5.4 Ion irradiated waveguides

The last kind of waveguides where the second order susceptibility has been characterized with this method are the novel *ion irradiated waveguides*, fabricated at the CMAM (see section 4.1.3). Two different fabrication processes were studied, the first ones based on a buried heavily damaged and amorphous layer caused by electronic excitation damage, and the second ones produced by higher energy ion irradiations that produce single tracks of nanometer size.

5.4.1 High energy low fluence irradiation (Fluorine and Oxygen ions)

The fabrication method of this waveguides was presented in section 4.1.3. The characterization of their nonlinear coefficient d_{33} compared to that of the substrate was performed for oxygen and fluorine ions at different fluences and energies (fluorine ions at $22\,\mathrm{MeV}$ and oxygene ions at $20\,\mathrm{MeV}$). All of them give rise to step-like, high-jump index profiles and support highly confined propagation modes (see page 67). Being all the substrates **z**-cut, the measurements were made with the incident light beam forming a certain angle with the normal of the surface.

The nonlinear coefficient d_{33} preserved after the waveguide fabrication, compared to that of a virgin substrate, can be seen in figure 5.6 as a function of the irradiation fluence. Both measurement configuration, that is, transmission and reflection, were used. In the case of transmission, most of the times the Brewster angle was chosen to assert a good repetitiveness, and in reflection configuration, the angle was chosen arbitrarily as 42 or $45°$. The data show that both configurations are equivalent, as expected. For the different fluorine irradiations fluences, the SHG susceptibility

in the waveguide shows a rapid decrease as the fluence increases up to $10^{15}\,\mathrm{at/cm^2}$. With higher fluences, it seems to reach an stable value of 60% of the value of d_{33} of congruent $LiNbO_3$. As far as the oxygen irradiation data are concerned, it also shows a first decrease and then remains at $60-50\%$ of the virgin $LiNbO_3$ value. The origin of this initial decrease is unclear. One possible explanation may be that there are lattice defects created during the preamorphization stage, which produce small changes in the refractive index at the surface. In the case of ion implanted $LiNbO_3$ waveguides, this effect is also present and has been ascribed to depoling caused by the irradiation [181].

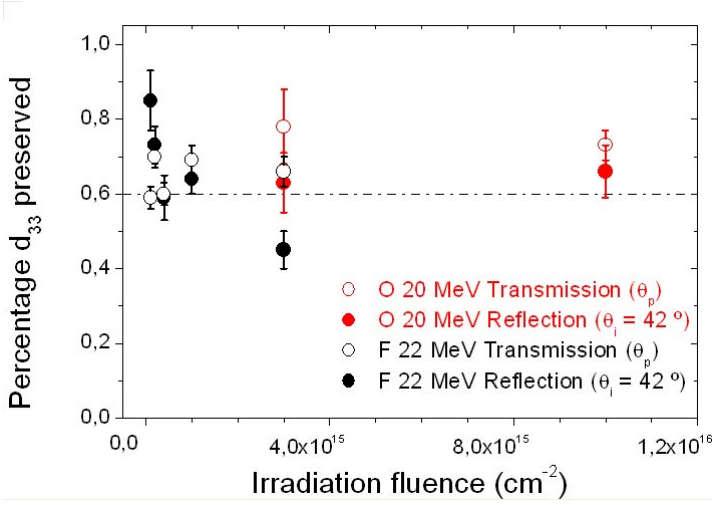

Figure 5.6: Percentage of the nonlinear coefficient d_{33} of z-cut $LiNbO_3$ preserved after ion irradiation waveguide fabrication with different ions (fluorine at $22\,\mathrm{MeV}$(circles) and oxygen at $20\,\mathrm{MeV}$(squares)) at different fluences, in transmission (open symbols) and reflection (solid simbols) configurations.

If this assertion is right, that is, if the lowering of the second order coefficient in these waveguides is due to a depolarization, the original values should be at least partially recovered with an annealing process. Therefore, further experiments were carried out with the fluorine irradiated

waveguides. The objective was to see how this annealing treatments affected the nonlinear coefficients of these waveguides, in order to know if the decrease of the nonlinear susceptibility could be recovered or not. In figure 5.7, the preserved nonlinear coefficient d_{33} is shown as a function of the fluence for two sets of samples, one of them as fabricated, the other after a thermal treatment (annealing at $300°\,\mathrm{C}$ for $30\,\mathrm{minutes}$). At this temperature, the refractive index profiles remain almost unaltered (they just become a little sharper), but the color centers generated by the irradiation process are removed, and the transparency of the samples is greatly enhanced. As it can be seen in figure 5.7, after the thermal treatment this initial drop of the nonlinear coefficient value is maintained, and only at higher fluences a partial recovery of the nonlinear coefficient can be observed.

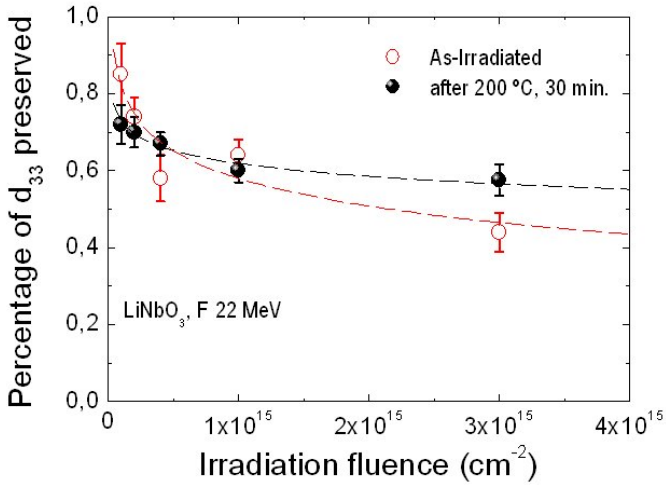

Figure 5.7: Nonlinear coefficient d_{33} preserved after fluorine ion irradiation at $22\,\mathrm{MeV}$ waveguide fabrication (z-cut substrates) normalized to that of virgin $LiNbO_3$, as a function of fluence. Open symbols correspond to data of the waveguides as fabricated, and full symbols represent the same samples after a thermal treatment of $30\,\mathrm{minutes}$ at $300°$.

Preliminary results on the electro-optic coefficient in this samples before and after the annealing show a similar drop ($r_{33} = 18.1 \pm 0.5\,\mathrm{pm/V}$, that is a reduction of around 44% compared to the substrate's value) for irradiation doses of 4×10^{14}, [145], which is in good accordance with the showed nonlinear coefficient measurement data. Then, if the depolarization was responsible of this first decrease of these coefficeints in the crystal, the annealing treatment should be enough to obtain a bigger recovery at low fluences. Therefore, as no substantial recovery can be seen, another explanation was proposed by G. García *et al.* [87]. They propose that, at low fluences, the irradiation process produce local rigid rotations of the $LiNbO_3$ structure (more precisely, of the oxygen octahedra), giving a theoretical explanation not only the behaviour of the second order nonlinear coefficients with the fluence, but also of the refractive index tensor. In the framework of this model, the initial decrease of the nonlinear coefficient showed in figure 5.6 is explained. Moreover, the data of figure 5.7 sustain the idea of local rigid rotations, because these lattice distortions should not dissapear with the annealing processes.

5.4.2 Swift ion irradiation at ultra-low fluences (chlorine ions, $45\,\mathrm{MeV}$)

Recently, another novel kind of waveguides has been developed. These samples are fabricated in the same irradiation regime as the ones fabricated with medium-mass high-energy ions, where the electronic stopping power becomes higher than the nuclear stopping power. In this regime, other ions such as silicon, nickel, oxygen, fluorine, chlorine, nitrogen... at energies from $3\,\mathrm{MeV}$ to $50\,\mathrm{MeV}$ have been reported as waveguide fabrication techniques [101, 137, 21, 22]. The fabrication process of these waveguides is described in section 4.1.3.

In figure 5.8 the measured relative d_{33} coefficient versus fluence for these waveguides can be seen. For fluences of less than $3 \times 10^{12}\,\mathrm{cm}^{-2}$ the SHG coefficients are preserved. These fluences are also the ones where practical optical waveguides are obtained. Even though the propagation losses of this waveguides were found $\sim 10\,\mathrm{dB/cm}$, the ultra-low fluences necessary to fabricate them, the fact that they provide a nano-structured waveguide media with high nonlinear coefficients, and the possibility of guiding TE and TM modes, make these waveguides quite appealing for a wide range of applications. For higher irradiation fluences, the d_{33} coefficient is almost 0%, due to the high amorphization of the waveguide.

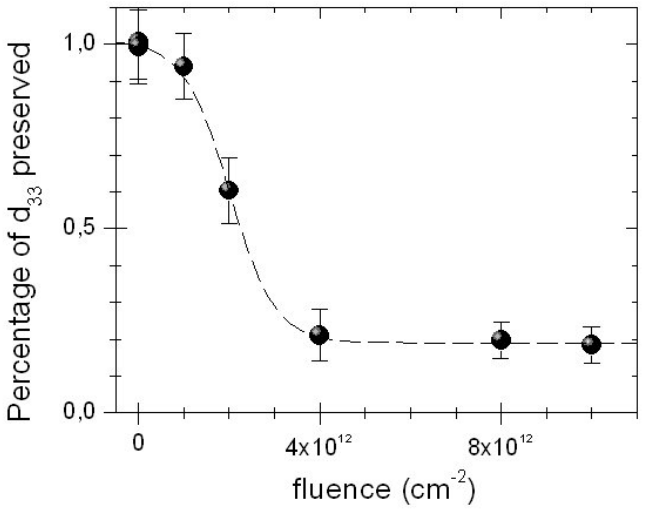

Figure 5.8: Nonlinear coefficient d_{33} preserved as a function of the ion irradiation fluence of clorine ions ($45\,\mathrm{MeV}$. The measurement configuration was reflection, with an incident angle of $4°$. The dashed line is only a guideline for the eyes.

For these waveguides, the electro-optic coeffcient r_{33} was also measured in a sample with an irradiation fluence of $2 \times 10^{12}\,\mathrm{cm}^{-2}$. The obtained value was $13.5 \pm 0.7\,\mathrm{pm/V}$, that is, around 40% of congruent $LiNbO_3$, which is in good agreement with the measured second order

nonlinear coefficient obtained for this value, because for these waveguides the loss of nonlinear properties is due to the amorphization of the waveguide layer produced by the irradiation. Anyhow, further work is necessary to understand the origin of the propagation losses in order to reduce them.

5.5 Summary

From the evaluation of the second order susceptibility of different optical waveguides, a first estimation of the suitability for nonlinear devices among these waveguides can be made. A summary of the properties of the various waveguides studied can be found in table 5.3.

Fabrication method	$\Delta n_e/\Delta n_o$	h_{eff} (μ m)	$r_{33}\%$ relative(*)	$r_{13}\%$ relative(*)	$d_{33}\%$ relative(*)
PE α-phase	$0.004-0.01/-$	$2-4$	$70-95$	$-$	90
Vapor PE	$0.101/-$	$1-4.5$	$-$	$-$	$10-40$
Reverse PE	$-/0.04$	~ 2.9	$-$	74	73
Zn-diffusion	$0.005/0.007$	~ 4	48	31	100
F irradiation	$\sim 0.1/\sim 0.2$	$2-4.5$	58	$-$	68
Cl irradiation	$0.005/0.01$	~ 2	43	$-$	60

Table 5.3: Summary of optical properties of $LiNbO_3$ waveguides. (*) relative refers to the substrate values, $r_{33} = 32\,\mathrm{pm/V}$, $r_{13} = 10\,\mathrm{pm/V}$, and $d_{33} = 34.4\,\mathrm{pm/V}$

From the first group, that is, proton exchanged waveguides, α-phase are the ones which show higher nonlinear coefficients (around 90% in x-cut and 70% in z-cut), along with a quite good homogeneity and well-defined phase. Then, vapor proton exchange waveguides present the next higher nonlinear susceptibility (up to 40% in some cases), but their fabrication method has to be thouroughly studied in order to obtain repetitiveness in

long samples. As far as other proton exchange waveguides are concerned, really good nonlinear coefficients have been found in reversed proton exchanged waveguides, but the fact that only ordinary polarized light can be guided in these samples, makes that the nonlinear coefficient which plays a role in this generation is d_{22}, and its value is around 10% of the d_{33} coefficient responsible of the nonlinear generation in all the other waveguides. Then, the effective coefficient is much lower than for the other waveguides and the generation in reversed proton exchange waveguides is not efficient at all.

Then, metal in-diffused waveguides, namely Zn-in-diffused and Ti-in diffused waveguides were characterized. Both of them presented nonlinear susceptibilities comparable to that of the substrate.

Finally, the preserved nonlinear coefficient was measured for ion irradiated waveguides. Two different sets of samples were studied, being the first ones fabricated via medium mass high-energy irradiation and the second via swift-ion irradiation at low fluences. In the first case, the nonlinear coefficient was higher than 60% of the value of congruent $LiNbO_3$, which makes them quite promising for nonlinear applications. Moreover, the measurement of the nonlinear susceptibility has been used as a tool to determine how the ion irradiation affects the $LiNbO_3$ structure. The last ones, while having a quite high nonlinear susceptibility at low fluences, (60% for fluences lower than $3 \times 10^{12}\,\mathrm{cm}^{-2}$), are a real novel waveguide fabrication technique, and further studies should be carried out in order to investigate the origin of the nonlinear coefficient loss at higher fluences. To sumarize, these two different ion irradiated kinds of waveguides are quite promising for nonlinear applications, but there is still much work to be done in order to clarify their nature. Besides, from a technological point of view, a lot of effort is being done in the fabrication of larger size samples, because the ones available now are not big enough

for practical applications and their optical losses are still fairly high.

Chapter 6
Optical Damage

Optical Damage

In this chapter a study on the optical damage of different kinds of waveguides is presented. The most important feature that these measurements provide is the light intensity threshold, that is, the loss of linearity between the in- and out-coupled intensities in single beam configuration. To have a reliable measurement of this threshold, a great effort was done in our group to have a method that provided the actual intensity inside the waveguide, which is not a trivial issue. The method proposed is treated in the appendix .

The first part of the chapter, section 6.1, is devoted to make a thorough comparative study of optical damage measurements in different planar $LiNbO_3$ waveguides fabricated on monodomain congruent $LiNbO_3$ **x**-cut substrates. For a further understanding of the phenomena underlaying the optical damage, the basic photovoltaic transport mechanism has been studied for several of these waveguides. Therefore, measurements of the photovoltaic current as a function of the in-coupled light intensity will be also discussed.

Then, in the second part of the chapter, section 6.2, optical damage measurements performed in **z**-cut samples will be shown, in order to examine whether there were any relevant differences with the **x**-cut ones. Besides, data of optical damage measured in periodically poled $LiNbO_3$

substrates and α-phase waveguides fabricated in those substrates will be also presented. Finally, preliminary measurements of optical damage in α-phase channel waveguides will be discussed.

6.1 x-cut substrates

A first study of the optical damage phenomena in x-cut planar α-phase proton-exchanged waveguides can be found in [4]. The corresponding experimental setup was described in section 4.2.5. There, three different regions were determined as a function of the propagating light intensity in the waveguide. In figure 6.1 these thresholds can be easily seen, when the light intensities at the input and output of the propagating fundamental mode of an α-phase waveguide are measured, as well as the three different regions mentioned above.

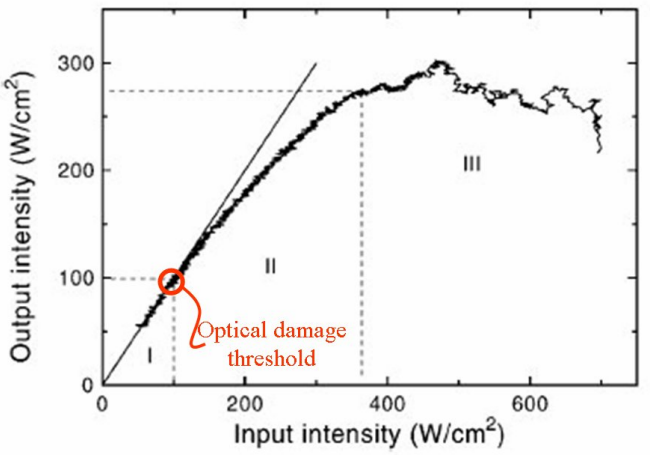

Figure 6.1: Output intensity (before out-coupling) versus input intensity (after in-coupling) in an α-phase waveguide. The two different thresholds determine three regions: I lineal, II not-lineal, and III chaotic [4]. The optical damage threshold, which is the boundary between regions I and II is pointed out.

In the first one (region I), which corresponds to low light intensities, the output intensity is proportional to the input light intensity, and no appreciable damage can be observed. This first region is delimited by the optical damage threshold. This threshold can be defined as the input light intensity at which the beam is widened and the linearity between the in-coupled and out-coupled intensity is lost. Region II begins at this optical damage threshold and comprises the range where the light beam is somehow degradated, being the output intensity related to the input intensity by a sublinear dependence, that is, the out-coupled light intensity is lower than the in-coupled intensity. Finally, region III, apart from presenting an output power lower than in region I, it is distinguished by a chaotic behavior of the output power. Moreover, the beam profile is clearly widened and the waveguide acts as an optical limiter, with an output intensity limit that cannot be overpassed, no matter how much light intensity is in-coupled into the waveguide. These effects were also observed also in bulk $LiNbO_3$, associate with parametric noise-amplification processes [176].

From now on, the results showed throughout this chapter will be focused on the measurement of the optical damage threshold. These measurements will be performed with the same experimental setup for different waveguides, because our aim will be to know how much light intensity can be propagated in each of these waveguides without suffering appreciable beam distortion.

6.1.1 Comparison of different x-cut optical waveguides

In this section, the optical damage resistance of several planar $LiNbO_3$ waveguides will be studied. There have been many previous works where the optical damage was measured for different waveguides. Some of these

experiments were based in the refractive index change measurement with interferometric [84] or holographic [104] configurations. As the damage threshold determination method varied from one work to the others,the obtained data is hard to compare. Moreover, as it is indicated in a recent review on the subject [95, 118], that even in nominally undoped substrates, the remaining impurity concentration can vary a lot from one sample to another and also the influence of light intensities and wavelengths is not the same for different waveguides. To avoid these problems, in this study a single beam setup was chosen in this work for all the samples, and all the waveguides were made in pure congruent $LiNbO_3$ substrates from the same origin. This way, the differences obtained can be attributed to the properties of the waveguides due to their fabrication process. Parameters such as dark conductivity, photo-conductivity or the role of second centers in the photo-refractive charge transport vary for the distinct waveguide fabrication methods.

Extraordinary polarized light

Optical damage measurements obtained with the single-beam setup for different waveguides supporting modes extraordinary polarized light can be seen in figure 6.2. This is the most interesting configuration for frequency conversion experiments, since it permits to take advantage of the highest nonlinear coefficient in $LiNbO_3$, that is, d_{33}. In all cases, the coupled mode was the fundamental one.

In this graph, the optical damage threshold of bulk $LiNbO_3$ appears at around $0.2\,\mathrm{W/cm^2}$. All the studied waveguide fabrication processes show a higher optical damage resistance. Among them, the less resistant waveguides are the Ti-in-diffused ones, as expected. These waveguides are known to have a very low optical damage threshold [90], almost of the same order of magnitude than that of the substrate.

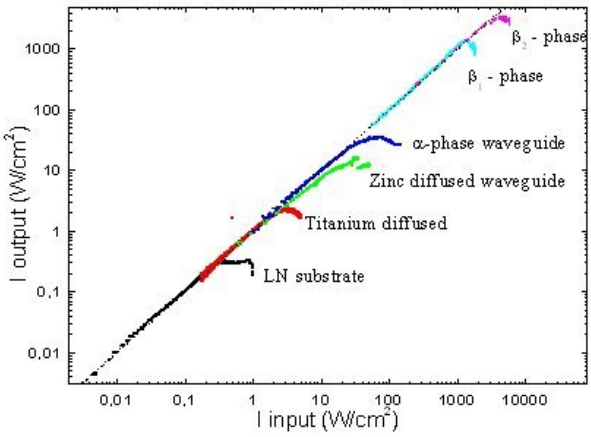

Figure 6.2: Output intensity (before out-coupling) versus input intensity (after in-coupling) different waveguides which support extraordinary polarized light. Bulk $LiNbO_3$ measurements are included for comparison.

The second thresholds that appear correspond to Zn-in-diffused and α-phase proton exchanged ones. The intensity which can propagate in these waveguides without suffering beam distortion is between one and two orders of magnitude higher than in the case of the substrate. As long as Zn-in-diffused waveguides are concerned, Zn doping in $LiNbO_3$ is usually used to increase the resistance to optical damage of $LiNbO_3$ [232], because Zn ions play a similar role to Mg, that is, they produce a decrease of the antisite Nb_{Li} defects. But this effect is evident in crystals with a Zn concentration is over $6\,\mathrm{mol}\%$ [232], which is much higher than the Zn concentration present in these waveguides (of about $2\,\mathrm{mol}\%$). Then, it is totally understandable that the measured optical damage threshold for this Zn-in-diffused waveguides is lower than the obtained in the case of highly Zn doped bulk crystals. Note that, both Zn-in-diffused and α-phase proton exchanged waveguides present an optical damage threshold relatively

low and nonlinear susceptibilities comparable to that of the substrate. Therefore, they are good candidates for frequency conversion. In fact, there are a number of reported experiments of second harmonic geration using these waveguides [50, 36].

Finally, β_1- and β_2-phase PE waveguides appear the most resistant to optical damage, with a measured optical damage threshold around four orders of magnitude greater than the substrate. Although these waveguides are not suitable for frequency conversion experiments, due to their low nonlinear coefficients, this extremely high optical damage resistance becomes a very important feature in the case of passive optical components, such as Y-junctions, light polarizers and others when high light intensities are used.

Ordinary polarized light

Then, guides supporting ordinary polarized modes will be also considered. The separation of both polarizations is due to the role played by the electro-optic coefficients on the optical damage. In the case of ordinary polarized light, the electrooptic coefficient r_{31} is involved, whereas for extraordinary polarized light is the r_{33} coefficient the associated one. The rate between this coefficients is $r_{33}/r_{31} \sim 3$ (see table 1.1). On the one hand, this difference stands for the higher optical damage thresholds found in this configuration. Then, for lineal optical components where the ordinary polarization index can be used, this configuration assures a higher light intensity propagation without distortion in the waveguide. On the other hand, one must be aware that frequency conversion is much less efficient in this configuration, because of the lower nonlinear susceptibilities

In figure 6.3 the results for ordinary polarized light propagating in the fundamental mode for different waveguides can be seen. The obtained

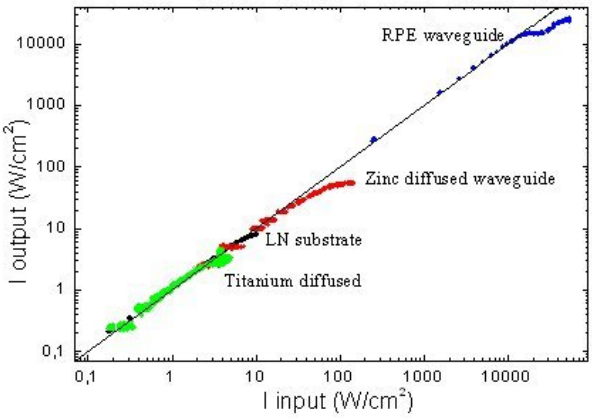

Figure 6.3: Output intensity (before out-coupling) versus input intensity (after in-coupling) different waveguides which support ordinary polarized light. Bulk $LiNbO_3$ measurements in both polarizations are included for comparison.

optical damage thresholds are around one order of magnitude higher than in the case of extraordinary polarized light, and that could be due to the different electrooptic coefficients. As in the previous section, the Ti-in-diffused waveguides show the lowest resistance to optical damage, being their optical damage threshold of the same order of magnitude than that of bulk $LiNbO_3$.

The optical damage threshold of ordinary polarized modes in Zn-in-diffused waveguides also appears over one order of magnitude higher than that of the substrate, being the reason of this behavior the same as the above explained in the case of extraordinary polarized light.

The most resistant waveguides for ordinary polarization are the Reversed PE. The threshold found for this kind of PE waveguides is higher than three orders of magnitude compared to the substrate. Nevertheless, the reason why these waveguides present such a strong resistance to

optical damage is still unclear.

6.1.2 Photovoltaic Currents in optical waveguides

In the introduction of this chapter, it was said that photovoltaic transport mechanism in waveguides was studied in order to gain a better understanding of the optical damage effect. In this section, the photovoltaic currents for different waveguides will be studied to get more information on the differences of the optical damage among them, because the photovoltaic effect is the main photorefractive transport mechanism in $LiNbO_3$, and the photorefractive effect is the main cause of the optical damage. In fact, relevant correlations between photovoltaic currents and the optical damage will be found and discussed next.

In figure 6.4, the measured photovoltaic currents are plotted as function of the in-coupled light intensity of the fundamental mode for different waveguides. The single-beam configuration setup was already described in section 4.2.4. All the waveguides are shown together, because in this case the involved coefficients in each configuration are very similar ($\beta_{33}/\beta_{31} \sim 0.85$ [218]) and the comparison can be directly made.

The results obtained in figure 6.4 point out some apparent differences among the studied waveguides. First of all, the order of magnitude of the photovoltaic current, which is several times greater for α-phase and Zn in-diffused waveguides compared to RPE and β phases. This seems to be correlated with the corresponding differences in the optical damage thresholds (see figure 6.2). In turn, the variations in the photovoltaic current j_{pv}, should arise from the changes induced by the fabrication processes to some relevant photovoltaic parameters. If one considers the simple expression for the photovoltaic current introduced in section 2.2,

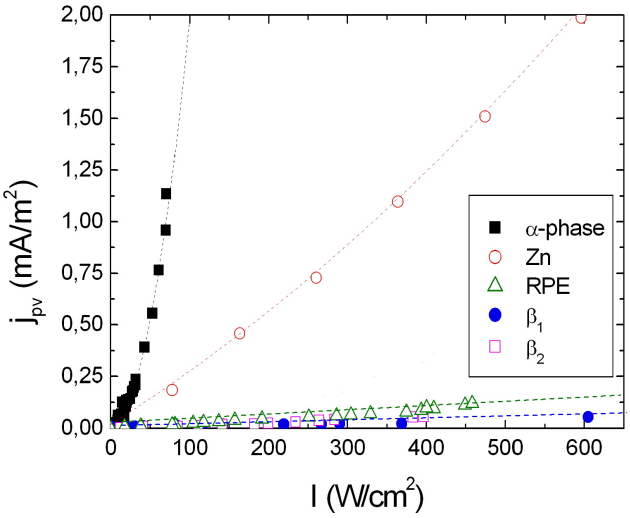

Figure 6.4: Photovoltaic current density versus the in-coupled $532\,\mathrm{nm}$ light intensity for different $LiNbO_3$ waveguides: α-phase (solid squares), Zn-in-diffused (open circles), RPE (open triangles), β_1 (solid circles) and β_2 (open squares).

$$j_{ph} = eL_{ph}\sigma I[Fe^{2+}] \tag{6.1}$$

the most probable parameters that may experiment changes are the photovoltaic transport length, L_{ph} and the concentration of [Fe^{2+}] related with the reduction state of the iron impurity.

Another striking characteristic that this measurements present is the super-linearity of the curves, that cannot be explained by this simple model. This behavior was first detected for α-phase waveguides by G. de la Paliza and myself [66], and it was confirmed in these measurements and also observed here in Zn-diffused and in RPE waveguides, although it is much less pronounced for the latter waveguides. In figure 6.5 the results of RPE and β-phases at a greater scale are shown, (α-phase is plotted in a different scale for comparison). Here one can better appreciate the

superlinear behaviour of RPE waveguides. On the other hand, one can also see the linear behavior of the β_1 and β_2 samples for the whole measured range, hence they follow the above mentioned one center model for the photovoltaic current.

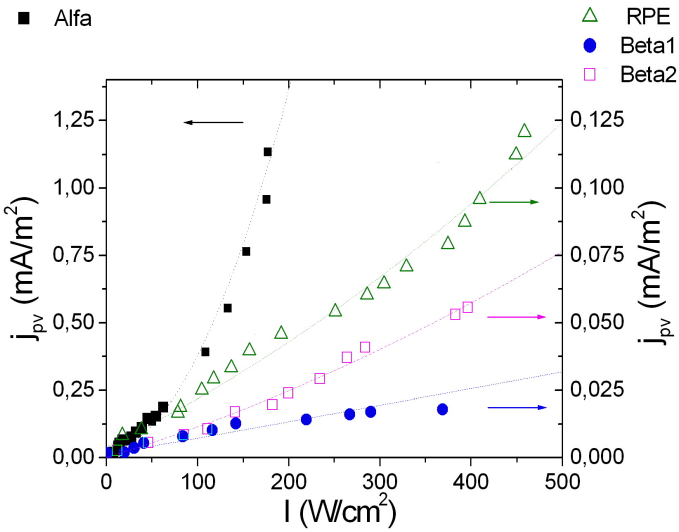

Figure 6.5: Photovoltaic current density versus the in-coupled $532\,\mathrm{nm}$ light intensity for RPE (open triangles), β_1- (solid circles), β_2- (open squares) and α-phase (solid squares) $LiNbO_3$ waveguides. α-phase is plotted with a different scale for comparison.

In summary, the lower the optical damage threshold is, the higher the photovoltaic current becomes. Moreover, for those waveguides with less optical damage resistance, the photovoltaic current has a super-linear behavior, and the starting point of this super-linearity roughly coincides with the actual value of the optical damage threshold. Due to these results it is worthwhile a further investigation on the superlinear behaviour of the different waveguides.

α-phase waveguides

A very detailed experimental and theoretical study has been carried out for α-phase PE waveguides. Firstly, the main experimental trends already described have been obtained using different wavelengths (see figure 6.6). If one looks at the low intensity regime represented in figure 6.6.b, the photovoltaic current depends linearly on the light intensity, following the equation 6.1

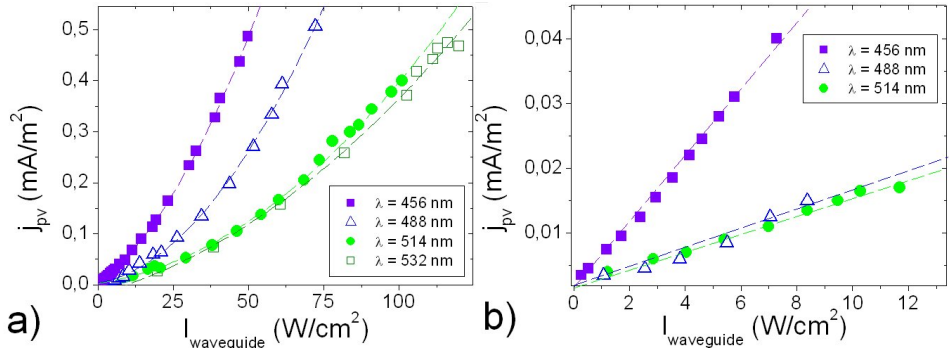

Figure 6.6: Photovoltaic current density versus the in-coupled light intensity for different wavelengths in an α-phase $LiNbO_3$ waveguides a) whole reachable range b) low intensity region.

When the in-coupled intensity is enhanced, the behavior becomes superlinear (figure 6.6.a), and the data can be fitted with a quadratic function, such as

$$j_{pv} = a \cdot I + b \cdot I^2 \tag{6.2}$$

being a and b constants to be fitted. This behavior is observed for all the measured wavelengths when a certain light intensity value is overpassed. To explain this behaviour, a possible proposal is the existence of a second center with a higher photovoltaic effect and with a low thermal activation

energy, so that at low intensities, being optical excitation negligible. As a consequence, the second center only influences the photovoltaic behaviour at large intensities. A similar model was proposed for bulk $LiNbO_3$ to explain the photorefractive effect by Jerman *et al.* and others [109, 115], although in those cases, the photovoltaic current was not analyzed in detail.

Then, we used this theoretical model in order to explain in detail the photovoltaic current behaviour in these waveguides. In our microscopic model of the photovoltaic, iron ions [Fe^{2+}/Fe^{3+}] are considered as primary centers (as usual) and [$Nb_{Li}^{4+}/Nb_{Li}^{5+}$], always present in congruent $LiNbO_3$, as the secondary ones. Moreover, these antisites were chosen because they fulfill all the conditions mentioned above and are the ones usually considered as secondary photorefractive centers in $LiNbO_3$. Very detailed calculations under this model were performed by a collaborator, Jesús Carnicero and can be found in reference [55]. In this approach, the expression for the photovoltaic current becomes

$$j_{pv} = eI(L_{pv1}S_{ph1}N_1 + L_{pv2}S_{ph2}N_2) \tag{6.3}$$

where N_1 and N_2 depend on the light intensity I and are also calculated from the equations of the model. In order to calculate $j_{pv}(I)$, and compare it with the experimental data, material parameters for the iron center were obtained from former photorefractive measurements [146] and the antisite concentration was also taken from literature. Then, the values for $L_{pv}S_{ph}$ is obtained from the fitting to experimental data. The result is plotted in figure 6.7. There, the contributions from both centers to the total photovoltaic current are shown (j_1 for the primary center and j_2 for the secondary). Both contributions are added to give the total photovoltaic current, plotted along with the experimental data. In the inset of the figure, the specific contributions of both centers at low light intensities are drawn, showing

that at very low intensities, only the primary center contributes to the photovoltaic current and then, at higher light intensities, the secondary center becomes the fundamental contribution to the total current.

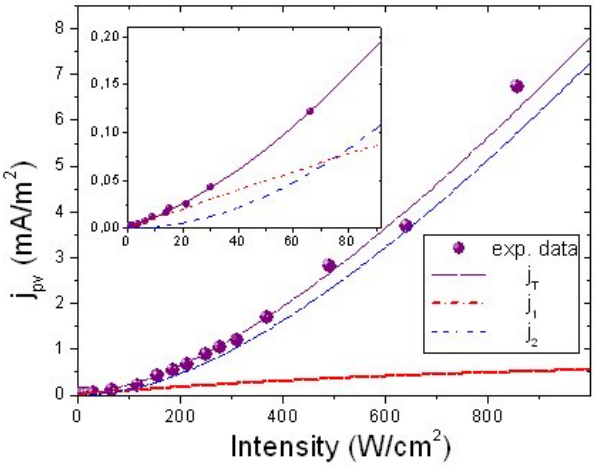

Figure 6.7: The dependence of the theoretical calculated photovoltaic current density $j(I)$ on the light intensity I (continuous line) and the individual contributions from the primary (j_1), red dotted line) and the secondary (j_2, blue dashed line) centers. Solid circles stand for the experimental data obtained for α-phase waveguides.

Zn in-diffused waveguides

In order to better characterize the superlinear behaviour of Zn-in-diffused waveguides, TM polarized modes were measured for higher light intensities. The result is plotted in figure 6.8), where a marked superlinear behaviour is found for light intensities in the waveguide over $1000\,\mathrm{W/cm^2}$, although the photovoltaic current also superlinear at lower intensities. This result is in good accordance with the obtained photovoltaic currents obtained in bulk Zn-doped $LiNbO_3$ crystals. In reference [198], an study

on the influence of different concentrations of ZnO (from 1.1 to $5.3\,\mathrm{mol\%}$) present in a $LiNbO_3$ substrate on the photovoltaic currents measured in bulk is shown. There, for ZnO concentrations similar to those present in these Zn-in-diffused waveguides ($\sim 2\,\mathrm{mol\%}$), also a superlinear behavior is shown. Note that in waveguides, the ZnO concentration cannot be varied as freely as in bulk, and these measurements provide a first characterization of the photovoltaic behaviour of these samples.

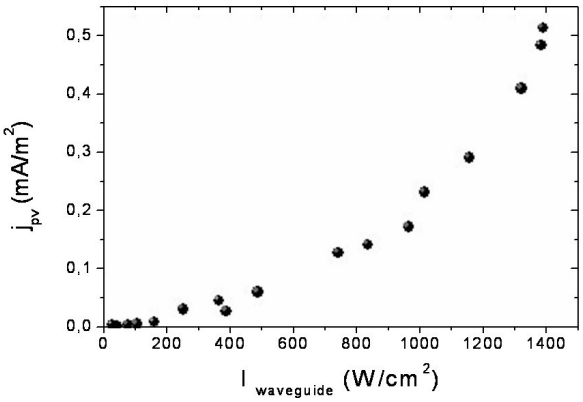

Figure 6.8: Photovoltaic current density versus the in-coupled light intensity in Zn in-diffused waveguides a) for different wavelengths b) for high in-coupled light intensities.

Apart from the antisite information that can be dragged from the photovoltaic curves, there is an additional photovoltaic parameter that could be obtained for these Zn-in-diffused waveguides, and that has not been measured previously. Given that not only TM, but also TE polarized light can be propagated, measurements at $488\,\mathrm{nm}$ were made for the fundamental modes of both polarizations. The results can be seen in figure 6.9. From the slopes of the curves in extraordinary and ordinary polarizations ($4.95 \pm 0.08\,\mathrm{A/W}$ and $3.52 \pm 0.06\,\mathrm{A/W}$ respectively), the relationship between the photovoltaic parameters β_{33} and β_{32} can be

obtained, and it results $\beta_{33}/\beta_{32} \sim 1.4$, being this value is of the order of the measured one in bulk, which is around 1.13 [218].

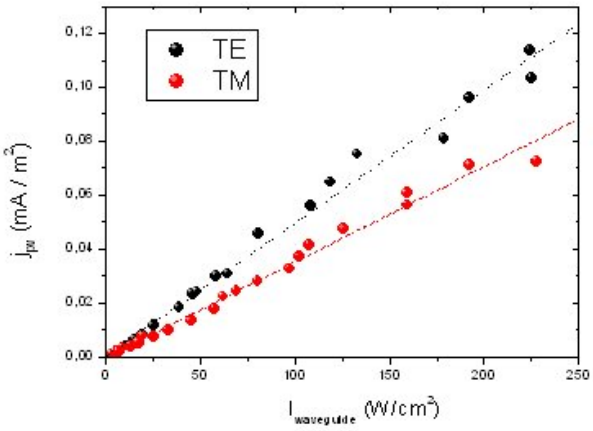

Figure 6.9: Photovoltaic current density versus the in-coupled light intensity in Zn in-diffused waveguides for TE and TM propagation modes at $488\,\mathrm{nm}$.

RPE

The study of $j_{pv}(I)$ in RPE waveguides requires more careful measuremens due to the low values of the photovoltaic current that were at the limit of our experimental resolution. However, the photovoltaic behaviour can be clearly observed in figure 6.10, where the measured photovoltaic current versus the in-coupled light intensity for different wavelengths is plotted. In this graph, it can be seen that j_{pv} increases at lower wavelengths. It can be also appreciated that for every wavelength, $j_{pv}(I)$ presents a superlinear behaviour, that is more evident for smaller wavelengths.

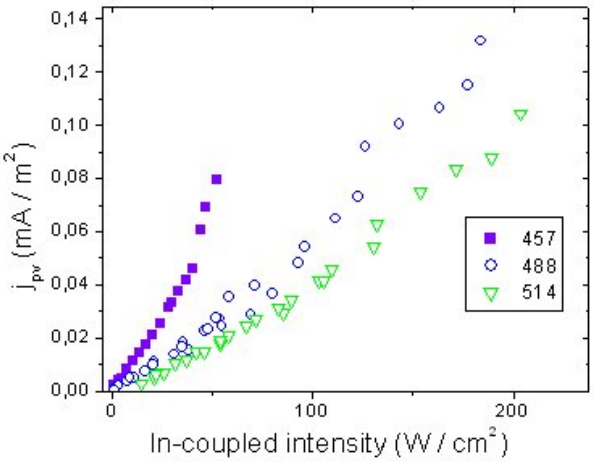

Figure 6.10: Photovoltaic current density versus the in-coupled light intensity for different wavelengths in a Reversed PE $LiNbO_3$ waveguide.

6.1.3 Summary and discussion

Along this section photovoltaic current data obtained for different kinds of waveguides has been presented. In these measurements, there are two different behaviours: linear and superlinear. A first linear region is found for all the measured waveguides, at least when low light intensities were coupled. In the case of β-phase waveguides, this behaviour extends to the whole measured region, which could be associated to a low photovoltaic transport length, L_{ph}, due to the crystalline structure of this waveguides, more centrosymmetric than congruent $LiNbO_3$. As far as the second superlinear region is concerned, this behavior has been associated to a secondary photovoltaic center, namely Nb_{Li} antisites. Figures 6.4 and 6.5 suggest that the concentration of this Nb_{Li} is lower after the fabrication of Zn or RPE waveguides than after α-phase fabrication processes.

A relevant result arises from the comparison between optical damage and photovoltaic current curves. There, it can be seen that the loss of linearity between the in- and out-coupled light in the optical damage measurements corresponds roughly with the region where the superlinear behavior of the photovoltaic currents appear. Moreover, this correspondence suggests a connection between this superlinearity and the appearance of single-beam optical damage, as it was proposed in [4, 5]. This result is in good accordance with other studies that indicate that in Mg-doped or stoichiometric $LiNbO_3$ crystals, the optical damage is reduced, because in these cases, the concentration of Nb_{Li} antisites is lower than in congruent $LiNbO_3$.

But there are some other parameters that may play an important role in the optical damage effect, apart from the photovoltaic current, such as the dark conductivity, which are difficult to determine in waveguides. Therefore, a full understanding of the mechanisms involved, including quantitative predictions of optical damage thresholds in waveguides, requires the characterization of these additional magnitudes and the extension of the two center model to the description of the photorefractive index change.

6.2 z-cut substrates

One of the objectives of this thesis work was the fabrication of periodically poled waveguide structures. Two techniques were used to fabricate the periodically poled substrates, namely Czochralski off-center technique and Electric Field Poling (more details about these techniques can be found in section 4.3). In the second case, the field has to be applied along the **z** direction of the crystal, and the usual experiment setup requires **z**-cut $LiNbO_3$ substrates. Also with this method, the fabrication of periodic

ferroelectric domains in **z**-cut substrates with waveguides in one or in both faces was possible, as it will be shown in the next chapter.

The problem was that in the case of planar waveguides fabricated in **z**-cut substrates, the confinement direction the **z** direction instead of **x**, and there was no previous study on the optical damage in this configuration. Moreover, the photovoltaic effect plays no role along the **x** axis, which makes the mechanisms involved in the photorrefractive damage different than in **x**-cut substrates. Therefore, measurements of the optical damage threshold of optical waveguides in this configuration were made. From the waveguides studied up to know in this work the most promising ones for future nonlinear devices seemed to be α-phase waveguides, because of their optical damage threshold is over one order of magnitude higher than that of the substrate and their nonlinear coefficients were around 75% of congruent $LiNbO_3$.

As far as the other kinds of PE waveguides, β-phase waveguides were disregarded due to their low nonlinear coefficients, RPE waveguides were also left out because they are not suitable for nonlinear generation for ordinary polarized light (see section 5.2.3). Ion-irradiated waveguides dimensions are presently far too small to study optical damage in them, although a great effort is being done on the homogeneous irradiation of larger areas. Finally, metal in-diffused waveguides were disregarded because of the high optical damage of the Ti in-diffused waveguides and the similarity in the properties between Zn-in-diffused and α-phase PE waveguides, being the last ones fabricated in our own laboratory. Consequently, from now on, all the experimental efforts will be focused on α-phase waveguides.

6.2.1 Comparison between α-phase waveguides fabricated in x and z-cut $LiNbO_3$ substrates

To obtain α phase waveguides of almost the same effective thickness as the ones studied in **x**-cut substrates, exchange times of $25\,\mathrm{hours}$ were made. In figure 6.11 the in-coupled versus the out-coupled light intensities are shown for α-phase PE waveguides fabricated on **x** and **z** cut substrates. In the second case, the increase of the optical damage threshold with respect to the threshold found for congruent bulk $LiNbO_3$ under extraordinary polarized light, is of one order of magnitude greater. This is the same relation found for α-phase waveguides fabricated on **x**-cut substrates.

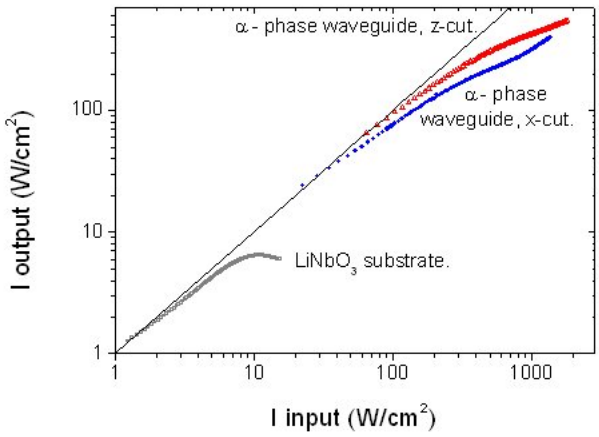

Figure 6.11: Output intensity (before out-coupling) versus input intensity (after in-coupling) for α-phase proton exchanged waveguides fabricated in **x** (blue circles) and in **z**-cut (red open triangles) substrates. As both support extraordinary polarized light, analogous measurements performed in bulk $LiNbO_3$ (grey open squares) with extraordinary polarized light are included.

Although the actual values of the optical damage threshold are equivalent for both configurations, in figure 6.12 the observed far field

images of the distorted beam in the case of α-phase PE waveguides fabricated in **x** and **z** cut substrates can be seen for different in-coupled light intensities. These images show a quite different behavior of the effect in both cases, being much bigger and asymmetric for **x**-cut samples.

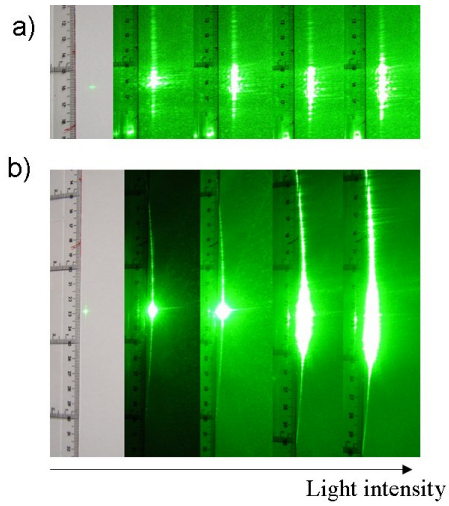

Figure 6.12: Far field images of the output light intensity in α-phase waveguides fabricated on a) **z**-cut substrates and b) **x**-cut substrates. The in-coupled intensity increases from left to right.

Anyhow, the most important differences are seen in the dynamics of the far field images. Once the out-coupled beam is distorted, the behavior of **x**-cut waveguides is completely chaotic, and when the intensity was decreased, the region where the beam has been propagated remains *damaged* for a certain extent of time. For **z**-cut waveguides, the distorted beam does not present such a marked chaotic behavior and the recovery of the undistorted beam when light intensity is lowered is almost instantaneous.

6.2.2 α-phase waveguides in z-cut substrates with different exchange times

As it was mentioned before, some studies are being made in our group to determine the Fe oxidation level in PE waveguides. The first results obtained for **x**-cut waveguides by J. Carnicero *et al.* indicated that the more exchange time (that is, the longer the substrate is immersed in the acid melt), the more reduced the waveguide is. This reduces the photorefractive effect and the optical damage resistance is enlarged. Given this preliminary result, it was found worth to study how much was enhanced the optical damage threshold in the case of α-phase waveguides fabricated in **z**-cut substrates. In figure 6.13 an increase in the optical damage threshold of one order of magnitude can be found when the waveguides are fabricated with a $90\,\mathrm{hours}$ process.

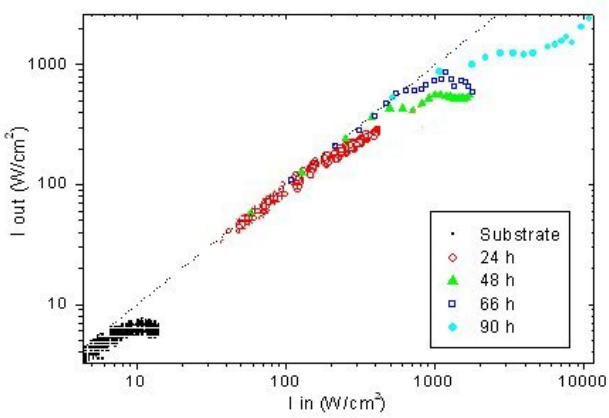

Figure 6.13: Output intensity (before out-coupling) versus input intensity (after in-coupling) of different α-phase waveguides fabricated on **z**-cut substrates with different exchange times. Bulk $LiNbO_3$ measurements are included for comparison.

6.2.3 Optical damage thresholds of α-phase waveguides in PPLN substrates

At the beginning of this section, it was said that the fabrication of periodically poled waveguide structures was one of the objectives of this work. At the start of this thesis work, the fabrication of different waveguides on PPLN substrates was studied, and it was found that the fabrication of α-phase waveguides in these substrates maintained the domain structure. Then, we managed to periodically pole α-phase waveguides fabricated on **z**-cut $LiNbO_3$ substrates. It is obviously very important to know whether the domain structure affects the waveguide performance, particularly if the optical damage effect is influenced by this periodic poling. Therefore, optical damage measurements were carried out in both kind of samples, namely, α-phase waveguides fabricated in PPLN substrates (first PPLN, then waveguide) and electrical field periodically poled α-phase waveguides (first waveguide, then PPLN).

As long as the first kind of samples are concerned, periodically poled erbium doped $LiNbO_3$ substrates grown in the Crystal Growth Laboratory of the UAM were used. Different proton exchange treatments were done to study if they destroyed the domain structure or not. It was found that the pattern was erased after VPE processes, but not after α-phase waveguide fabrication. In order to study the optical damage behavior of these waveguides, some measurements were taken with the one-beam configuration technique, both for the PPLN substrate and for the waveguide [1]. The results are shown in figure 6.14

The increase of the optical damage threshold with respect to the bulk PPLN is over one order of magnitude, as in the case of waveguides

[1] The optical damage measurements were performed by Dr. Ángel Alcázar de Velasco and Axel Alonso

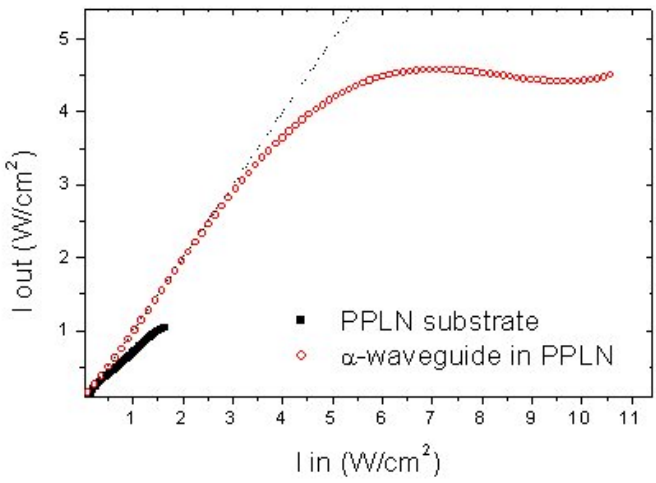

Figure 6.14: Output intensity (before out-coupling) versus input intensity (after in-coupling) of an α-phase waveguide fabricated on a PPLN **z**-cut substrate and bulk PPLN.

fabricated on congruent single-domain $LiNbO_3$ studied before. The main drawback of these crystals from the optical damage point of view, is that the substrate is damaged at intensities of two orders of magnitude lower than bulk congruent $LiNbO_3$ purchased to Photox. The origin of this low damage threshold should be a higher level of residual photorefractive impurities. Even though the waveguide fabrication enhances the resistance to optical damage, the intensities that can be guided without beam distortion are very low.

As far as the second kind of samples are concerned, that is, electrical field periodically poled α-phase waveguides, the next chapter (chapter 6.2.4) will be devoted to the electric field periodic poling of previously fabricated α-phase waveguides. to these results, this section deals with the comparison of the optical damage threshold in two α-phase waveguides, both fabricated with a $24\,\mathrm{hour}$ proton exchange on congruent **z**-cut congruent $LiNbO_3$ substrates, but one of them was afterwards periodically

poled by the application of an electric field, with a domain period of $15\,\mu\mathrm{m}$. The measurements were made with almost the same single-beam setup described before, except that the guided light was not out-coupled with a rutile prism but edge-out-coupled with the aid of a microscope objective. An iris was also placed as spatial filter to determine whether the beam remained undistorted or not. The problem with this setup is that it is not completely analogous to the one used throughout this chapter, but the small dimensions of the periodically poled area made impossible any other experimental configuration. Therefore the measurement of the not poled sample was carried out again with this setup to compare directly both waveguides in the same experimental conditions. Periodically poled $LiNbO_3$ is reported to have lower optical damage than single-domain $LiNbO_3$ [162, 210, 111], but in our case the measured behavior of both samples (see figure 6.15) is almost the same.

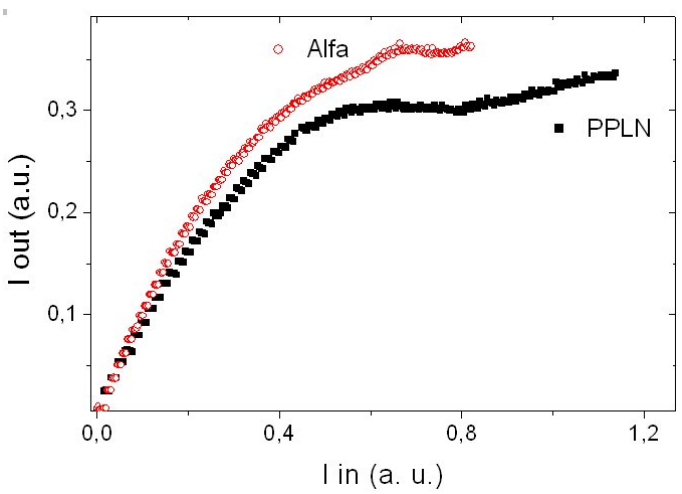

Figure 6.15: Output intensity (before out-coupling) versus input intensity (after in-coupling) of a periodically poled α-phase waveguide compared to a monodomain α-phase waveguide, both fabricated in **z**-cut substrates.

This may be due to the large period of this sample, since, as reported

by Sturman *et al.*, the PPLN structure diminishes the optical damage only for small domain periods [202].

6.2.4 Optical damage in channel waveguides

The last measurements in relation with the optical damage effect that will be discussed in this chapter, deal with the light intensity that can be guided in channel waveguides. Given that we know the optical damage behaviour of z-cut planar α-phase waveguides, we will compare one of these samples with the data measured in channel waveguides.

The planar waveguide was measured in the same configuration used in the previous section, that is, the edge was polished and light was focused with a lens and then prism in-coupled and out-coupled with microscope objective. As far as the channel waveguides are concerned, they were also fabricated in z-cut single domain congruent $LiNbO_3$, with an SiO_2 mask (as described in section 4.1.4) and a proton exchange treatment of $24\,\mathrm{hours}$ that gave rise to an array of α-phase channel waveguides. In these samples, light was in- and out-coupled with the aid of microscope objective, and then, the out-coupled light power was recoiled with the aid of a photodetector.

The results are plotted in figure 6.16, where the in-coupled light intensity versus the out-coupled light intensity can be seen. For both channel and planar waveguides, light is out-coupled in the same way, and, if one takes into account the different effective areas of each waveguide, the comparison between them can be made. The light intensity that can be guided in a channel waveguide is more than three orders of magnitude higher than in the case of planar waveguides. Given that the optical damage threshold measured for this planar α-phase waveguide is roughly $100\,\mathrm{W/cm^2}$, the optical damage threshold in the case of channel

waveguides appears around $100 - 1000\,\mathrm{KW/cm^2}$.

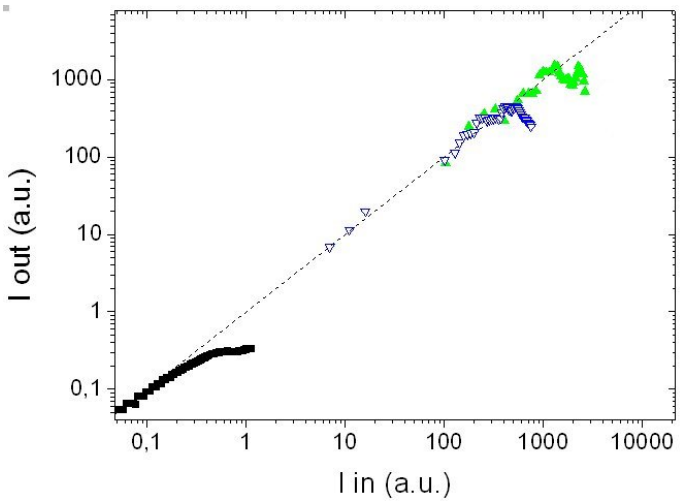

Figure 6.16: Output intensity (before out-coupling) versus input intensity (after in-coupling) of a planar α-phase waveguide fabricated in a z-cut $LiNbO_3$ substrate (solid squares) compared to a set of channel α-phase waveguides also in z-cut substrates. The channels widths are $20\,\mu\mathrm{m}$ (open blue triangles) and $10\,\mu\mathrm{m}$ (solid green triangles) and $3\,\mu\mathrm{m}$.

Although these are preliminary results and a deeper study should be performed, these measurements show that the optical damage mechanisms in planar and channel waveguides are not the same. This may be due to the lack of fanning in the case of channel waveguides, which would explain the higher damage resistance that they show. This is a very appealing result, because for nonlinear frequency conversion applications, channel waveguides are preferred because of the higher light confinement that they provide. But this advantage would be rather poor if they had not, in addition, a higher resistance to the optical damage effect, as it has been found here.

Chapter 7
Electric Field Periodic Poling

Electric Field Periodic Poling

In the previous chapters the nonlinear characterization of different waveguides has been carried out. From the nonlinear coefficients measurement and their optical damage threshold characterization, one of the most suitable for the fabrication of nonlinear devices among the studied waveguides, resulted the α-phase PE ones, which were also available for the present research. In order to achieve efficient nonlinear devices in $LiNbO_3$, this chapter will be devoted to the investigation of the possibility of combining this α-PE waveguides with the fabrication of periodic domains by the application of an external electric field. Domain structures down to $5\,\mu\mathrm{m}$ period length, which is the lowest limit generally accepted for the standard electrical poling technique in bulk, were achieved.

At difference with most previous works in proton exchange waveguides, electric field poling at room temperature has been carried out after waveguide fabrication. In this case, to periodically poled the waveguide, the domain structure has to be homogeneous along the first microns below the surface, where the guiding layer is, but it is not necessary to pole the whole bulk.

To give a brief overview of previous experiences in periodically poling of $LiNbO_3$, there are some groups that have chosen to prepare different

PE waveguides on previously poled bulk PPLN substrates by electric field application [81, 61, 169]. Other groups have developed new methods of electric field poling which result in a domain structure only in the surface of the sample (achieving smaller domain periods), and then they fabricate the waveguide [41]. However, some of the above mentioned waveguide fabrication processes cause partial ferroelectric domain reversal, i.e. the ferroelectric domain pattern of the bulk is partially or totally erased after the PE. Given that it may also happen with other kind of waveguides that are being optimized these days, such as those made by ion irradiation, it was found preferably for our waveguides the study of the possibility of this new sequence (periodically poling after waveguide fabrication), that has been previously used in PE only by Gallo *et al.* [86] and never in α-phase waveguides.

This chapter will show first the adjustment of the electric field poling technique at room temperature to waveguide samples. Firstly, it will be applied to bare congruent $LiNbO_3$ substrates to check that the poling technique worked for our experimental conditions. Secondly, α-phase PE waveguides will be periodically poled. For each of the periodic poling experiments, the visualization of the domains was performed, via chemical etching, diffraction techniques and SNOM. The first technique was used to study the homogeneity and quality on the domain structures in the surface and in the waveguide depth, and the others were used as non-destructive qualitative characterization techniques about the domains present in the waveguide layer. Moreover, the excellent optical performances of single-domain α-phase-PE waveguides were checked again after the domain reversal and they were not found to be affected by the periodic poling. (The results of this chapter have been published in reference [46]).

7.1 Adaptation of the electric field poling technique

The electric field periodical poling of $LiNbO_3$ technique has already been described in sections 1.2.4 and 4.3.2. As it is quite recent, there are still a lot of open questions about the relevant parameters, the dynamics of the poling, the domain wall growth and many others. At the beginning of our study, I made a three months stay in the Photonics Center of Boston University (USA) to learn the basics of this technique applied to bulk $LiNbO_3$ samples around $30 \times 20 \times 0.5\,\mathrm{mm}^3$ and with domain periods around $20\,\mu\mathrm{m}$. There I started to work with the polarization setup, photolithographic facilities and also gathered information about the whole process. Although one of the objectives was to adapt the experiment to samples of the sizes employed for waveguide fabrication (approx. $25 \times 8 \times 0.5\,\mathrm{mm}^3$), that was not possible.

Back in Spain, a poling chamber adapted to our size $LiNbO_3$ substrates was designed and fabricated, and another stay was planned, in Bonn University (Germany) in the group of Prof. Buse, where they had a vast experience in periodic poling and domain visualization but with relative large domain periods. Moreover, they shared with us the aim to go to lower domain periods under $10\,\mu\mathrm{m}$ and we worked together to achieve them.

7.1.1 Checking of the poling chamber performance

The electric field poling is a quite common technique, and there are several groups that use it for PPLN fabrication. The problem that is found in literature is that the process, although extensively used, has not standard conditions. Different groups use different liquid electrodes,

o-ring materials, voltage pulse waveforms and so on. It was found that the smaller the period length that was trying to be made, the easier any change in the experimental parameters of the poling setup resulted in unsuccessful experiments and broken samples. And, consequently, the change of the poling chamber usually used for poling experiments in Bonn by our chamber made us make a lot of adjustments for it to work again. For that reason, a number of attempts had to be made with different o-ring materials, metal electrodes, resists and liquid electrodes to obtain the first results in the domain reversal of whole bulk samples with voltage ramps in our samples. Experiments, such as the measurement of the coercive field (E_c) of $LiNbO_3$ (shown in figure 7.1), were tried until they were successful and reproducible with this new chamber. This experiment consists on the domain reversal of a non structured sample, using the poling chamber. The applied voltage was increased with a slow ramp, and when the coercive field was reached, a current flow through the sample was detected. Once the whole area was reversed and no more current was detected, the voltage was ramped down. Then, another ramp was applied to the sample, but with in the opposite direction, in order to pole again the sample.

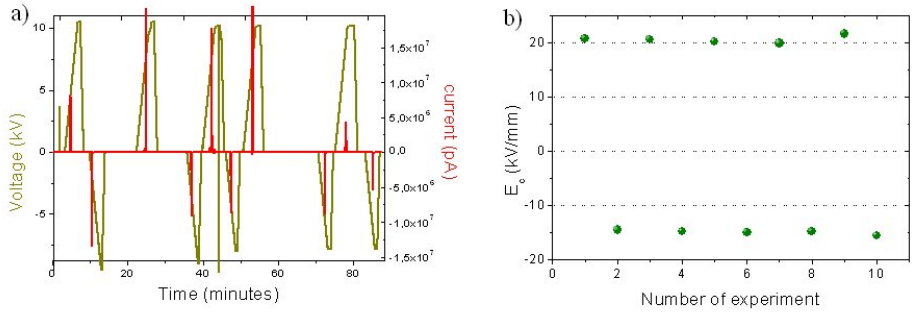

Figure 7.1: Forth and back domain reversal of a $0.5\,\mathrm{mm}$ thick bulk congruent $LiNbO_3$ sample. a) The different voltage ramps applied (dark yellow) and the current obtained (red) b) The field at which the poling happened, that is, the coercive field, for each of the times the experiment was performed

7.1.2 Periodic poling of $LiNbO_3$ substrates

The next step was the application of pulsed voltage waveforms to samples with lithographically defined electrodes in the same chamber while the current through the material was being monitored (as was described in section 4.3.2). The first poling trials were intended to create domain structures of $18\,\mu\mathrm{m}$ period length, which was already smaller than the period length previously used by the group of Prof. Buse [122] but was still bigger than the usual admitted limit for this technique. In order to find an appropriate waveform shape, the previous experience of this group along with the works of Fejer *et al.* [197, 19] were considered.

Voltage waveform

The chosen voltage pulse has different stages, and each of them is supposed to enhance a certain step of the poling process. This stages were already mentioned in the Experimental Techniques chapter (section 4.3.2). Thus, a proof voltage waveform was applied to the samples and, depending on the domain pattern obtained after the selective chemical etching of the structure (see section 4.3.3), this pulse was modified until the resulting domain structure was satisfactory. A brief description of how the voltage waveform is supposed to affect the domain reversal dynamics can be seen in figure 7.2 and it could be explained as follows [194]:

- First stage: The voltage is increased up to a value such that the field applied to the sample is kept below the coercive field.
- Second stage: This voltage is maintained for a certain time.
- Third stage: A voltage peak of a few ms is applied to the sample, making the applied field go far over the coercive field. At this point,

domain seeds arise along the electrode surface in what is called the *nucleation* stage of the poling process.

- Fourth stage: The voltage is decreased down to an applied electric field a little over the coercive field. At this stage, the domain seeds begin to grow along the depth of the sample and also sideways under the electrodes and the domain walls are formed. This voltage is maintained until the switching process is finished.

- Fifth stage: Once again the voltage is decreased to a value of the applied field near the coercive field but a little below it. This is called the *stabilization stage* and prevents the backswitching or *flip-back* of the domains to their initial state.

- Sixth stage: The applied voltage is ramped to zero.

The voltage waveform was adapted experimentally, that is, after several voltage pulses were applied to the sample, the domain pattern was etched and the structure created was studied under the microscope. This observation, along with the recorded current, was used to determine whether the applied voltage was appropriate. If it was not so, this information was used to correct it. For example, if the nucleation rate has not been enough, there were regions without any domain reversal. In order to enhance it, the third stage peak was increased in the next experiment. On the contrary, if the third stage peak was too high, the nucleation started all over the sample, not only under the electrodes, and the whole sample presented domain reversal. The fourth stage could also be experimentally controlled by the observation of the boundaries of the switched domains. If the applied voltage at this stage is too high or too long, the domain boundaries overpass the limits of the electrodes and they can even collide with each other.

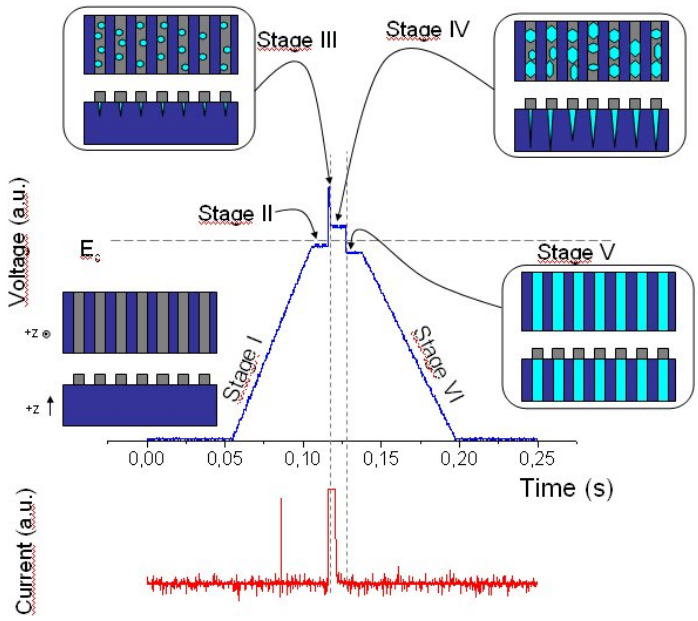

Figure 7.2: A typical voltage waveform and the different stages of the poling process that take place with it.

Other parameters, such as the evaporation of metal on the resist pattern, which is supposed to enhance the nucleation rate, and different liquid electrodes were also tried, but no difference was found.

Deep studies on the dynamics of periodic poling can be found in references [227, 196], even from a theoretical point of view [38]. Most of their considerations were taken into account for the design of the first trial waveform. However, at difference with that works, this empirical approach does not intend to make an analysis on the domain structure evolution, but it provides a simpler way of engineering the fabrication of periodically poled $LiNbO_3$.

Results

The first samples that where tried to pole had resist structured electrodes in the +**z**-face for $18\,\mu\mathrm{m}$ period length structures. The resist stripes were $9\,\mu\mathrm{m}$ and they were $9\,\mu\mathrm{m}$ apart from each other. In the initial experiments, up to 50 pulses were applied to the samples, before a little current was detected during the process. After each pulse, the sample was observed through crossed polarizers, in order to determine in a very rough way if there had been any domain reversal. Then, the pulses were changed and, after a few more trials, the number of pulses applied decreased to 20 and the first quasi-periodically poled samples were obtained. Even though these early experiences showed too large reversed domains or too little nucleation or inhomogeneities all over the sample, they helped us to adjust the waveform pulse. Finally, homogeneous periodically poled $LiNbO_3$ of $18\,\mu\mathrm{m}$ period length was obtained after the application of three voltage pulses, with a maximum voltage of around $24\,\mathrm{kV/mm}$. One of these samples can be seen in figure 7.3.

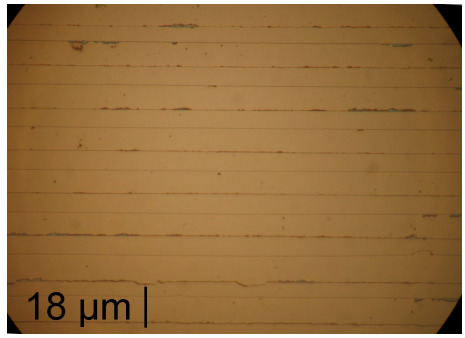

Figure 7.3: An $18\,\mu\mathrm{m}$ period length PPLN substrate after 30 minutes of chemical etching at room temperature.

Then, we started to make poling attempts to substrate samples with resist periodicities of $15\,\mu\mathrm{m}$. Even though there was only a small change in

the period, compare to the previous samples of $18\,\mu\mathrm{m}$ period length, some adjustments had to be made to the waveform to achieve homogeneously poled $LiNbO_3$. The modifications were mainly done to increase the nucleation everywhere on the sample. Therefore, its maximum peak, corresponding to the third stage of the waveform, was increased (around $26\,\mathrm{kV/mm}$) and it was also made shorter (only $1\,\mathrm{ms}$) to prevent excessive domain spreading. This shows how precisely had to be the poling parameters in order to achieve high quality periodic poling. In figure 7.4 it can be seen one of this PPLN in two different magnifications, after 20 minutes of chemical etching.

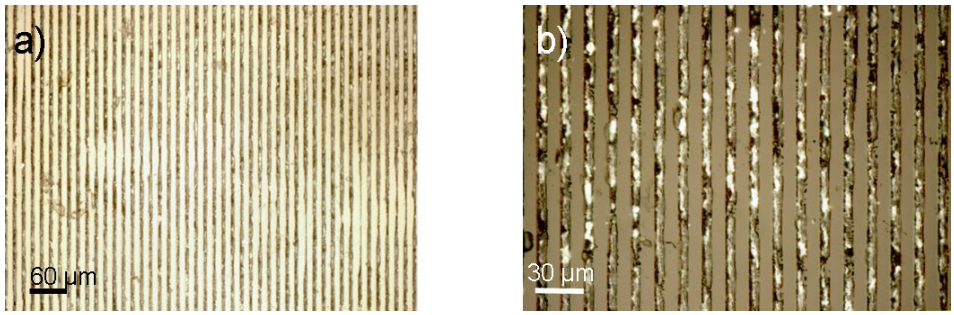

Figure 7.4: A $15\,\mu\mathrm{m}$ period length PPLN substrate after 20 minutes of chemical etching at room temperature.

Once the periodic poling of congruent $LiNbO_3$ substrates was achieved, the setup was considered completely checked in order to begin with the next step: the periodical poling of α-phase-PE waveguides.

7.2 Periodical poling of α-phase waveguides

Periodical poling by structured electrodes and electric fields has been extensively investigated in the past years to obtain high quality ferroelectric domain structures with a periodicity of $30 - 15\,\mu\mathrm{m}$. Our results up to

this point do not add anything new, as far as periodic poling in $LiNbO_3$ substrates are concerned. At variance, our next step combines two subjects that attract a great effort nowadays:

- Obtaining smaller periods adequate for frequency conversion in the green-blue range region (that is, $10 - 3\,\mu\mathrm{m}$ period length).
- Periodically poling of waveguide layers, to take advantage of their high light confinement capabilities.

First of all, it is worthwile mentioning that in bulk $LiNbO_3$ substrates it is quite difficult to obtain homogeneous domain structures for period lengths lower than about $5\,\mu\mathrm{m}$, unless much thinner samples than the usual 0.5 mm thick $LiNbO_3$ substrates are used.

Then, as far as waveguide poling is concerned, there is no need of periodically poling the whole substrate, as it must be done in bulk. As the waveguide lays in the first microns under the surface, several methods that produce domain reversal in the surface, such as Ti in-diffusion [36], Li out-diffusion, thermal treatments [100], and proton exchange [236] have been tried (see table 3.1). The problem is that, with these methods, the in-depth profile of the ferroelectric domains show a triangular or semicircular profile, as it can be seen in figure 7.5.

Apart from the in depth shapes of the domains, these procedures give rise to periodical inhomogeneities of the refractive index profile along the propagation direction of the waveguide. As it was already said in the introduction of this chapter, there are groups that fabricate PE-waveguides on electric field periodically poled substrates. Then, the obtained domains have a constant in depth profile, but as we have already seen, almost the same fabrication processes that give rise to guiding layers can also reverse the polarization of $LiNbO_3$, thus the ferroelectric domain structure may be damaged or altered.

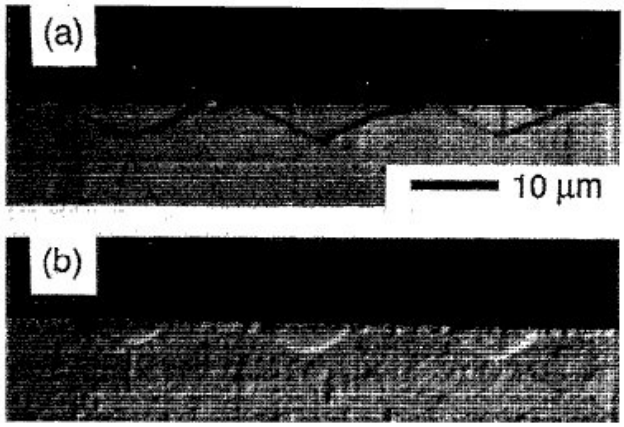

Figure 7.5: Photographs of polished and etched **y** faces of z-cut $LiNbO_3$ substrates after the fabrication of a domain pattern of $21\ \mu\mathrm{m}$ a) by Ti-in-diffusion (showing the triangular shape of the reversed domains) and b) by annealed PE (showing round shapes of the domains). These photographs are taken from reference [134].

At difference with them, a different fabrication sequence will be used in this work. In this section the new results on the periodic poling of previously made α-phase-PE waveguides will be shown. Once the electric field technique was operative, the experience acquired with bare $LiNbO_3$ samples was applied to samples with waveguides in one or both **z** faces. As a result, high-quality PPLN structures were fabricated with duty cycles of around 0.5.

7.2.1 Periodically poled α-phase waveguides: $15\,\mu\mathrm{m}$ period length

As it was said at the beginning of this section, proton exchange process itself can change the spontaneous polarization of $LiNbO_3$. In references [216, 236] the effect of proton exchange followed by a quick thermal

treatment can be found. In these works, the PE is considered as a trigger of the domain reversal, that is carried out after it, at temperatures higher than $1000^{\circ}\,\mathrm{C}$. The reason why the domain reversal happens is still unclear, and neither why it happens mainly in the positive **z**-face, as in the case of Ti in-diffusion.

Although this effect has been reported for aggressive proton exchange treatments, not for α-phase fabrication methods, the possibility of taking advantage of a possible partial polarization (or depolarization) of the surface layer due to the waveguide fabrication lead us to begin with samples with an α-phase PE waveguide fabricated on the positive **+z** face of the substrate. Then a photoresist grating of $15\,\mu\mathrm{m}$ length was made on the same face where the waveguide was. In the initial trials, the same pulses as the ones used for bulk periodic poling were used, but the samples broke. As it was not clear at which point had the sample cracked, instead of applying directly the final voltage waveform, a previous pulse was sent with the same timing and values of the ones used for bulk $LiNbO_3$ periodic poling but without the third stage, that is, without the high voltage peak (see figure 7.6.a). That time, the sample did not broke, and no current flow was detected. After it, two other complete voltage pulses were applied (basically the same ones used before, of around $100\,\mathrm{ms}$ and $24\,\mathrm{kV/mm}$ maximum field each, as can be seen in figure 7.6.b), a certain current was detected and when the sample was examined under crossed polarizers, it seemed to be poled.

Then similar experiments were carried out on substrates with samples in both sides or only in the **-z**-face. When the photoresist pattern was deposited onto the -z face, the shape of the pulses had to be slightly modified. In this case we observed that there were more pulses needed to periodically pole the sample, and that resulted in overpoling. To avoid that, the maximum field applied was slightly increased to favor domain

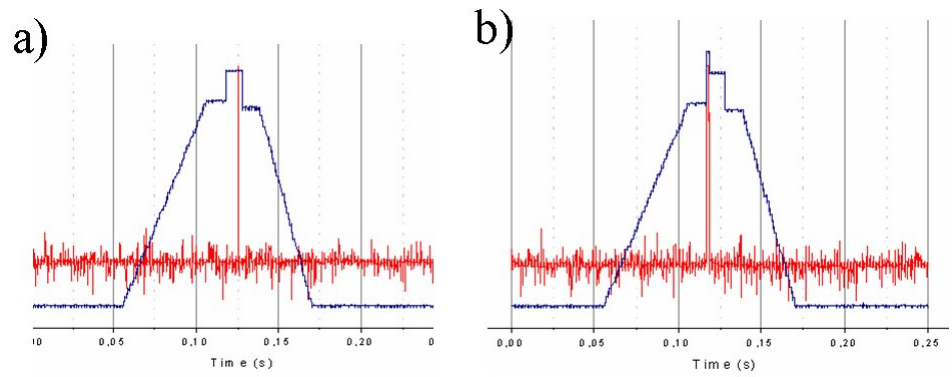

Figure 7.6: Voltage pulse waveforms applied to an α-phase waveguide along with the current flowing through the sample. a) without the third stage, no current is detected b) with the peak there is current flow and, after two of these pulses, the sample was poled.

nucleation. These modifications were optimized through a number of experiments, until we obtained a duty cycle of about 0.5.

Non-destructive characterization

a. Propagation properties

In order to investigate the effect of periodical polarization on the waveguide quality, its guiding properties were checked again. Two modes, as in the original waveguide, were found in the red with the dark mode technique. Propagation losses after the domain inversion were found to be similar to the previously obtained values, that is, below $0.4\,\mathrm{dB/cm}$ (which is the detection limit of the setup).

b. Light diffraction

To further confirm that the waveguide layer was periodically poled, diffraction of guided modes by the domain walls was investigated (see section 4.3.3). The diffraction pattern was observed with maxima at angles corresponding to a refractive index grating due to the domain walls, that is, half of the periodicity of the reversed domains. An image of the screen with the fundamental bright mode and the diffracted maximum can be seen in figure 7.7.a. The diffraction in the domain walls of light normal to the surface, that is, not guided, was also checked. The diffraction pattern obtained can be seen in figure 7.7.b.

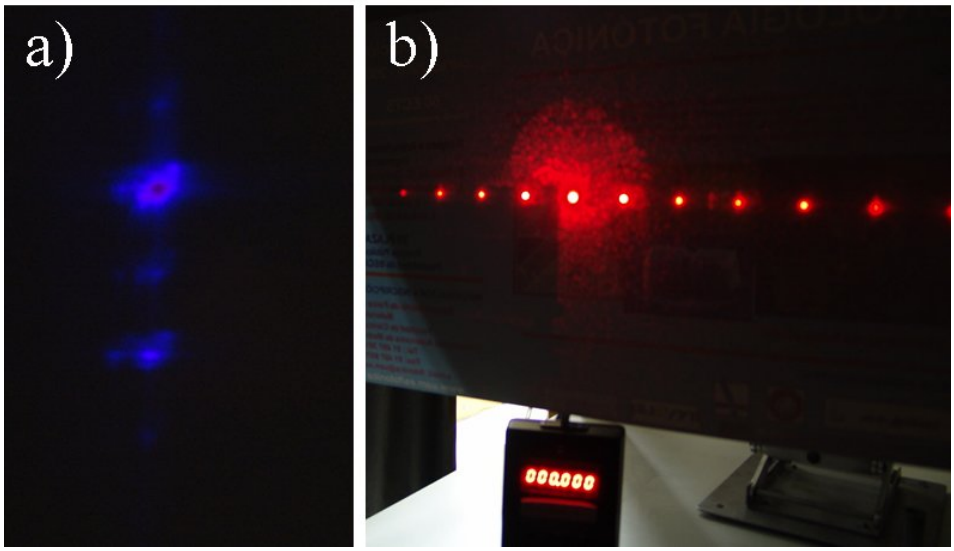

Figure 7.7: Diffraction by the domain walls a) of light guided in the waveguide and propagated along the **y**-axis b) not guided light.

c. SNOM

A little time after, prof. Jaque offered us to make Scanning near-field optical microscopy *SNOM* of these α-phase waveguide samples. This technique, which combines optical microscopy and scanning probe technology, provides a surface analysis of the ferroelectric domain structure [98, 116]. In figure 7.8, a three dimensions image of the structured surface of a sample, measured in reflexion configuration, can be seen. [1] In this image, the domains can be clearly seen, though the actual reason for this pronounced contrast between the domains is being now under study [127]

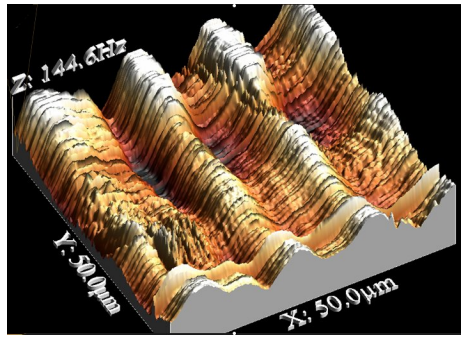

Figure 7.8: SNOM image of the surface of an α-phase waveguide after the periodic poling process

Further characterization of the domain structure: chemical etching

The halves of the samples with the edged polished were then etched in HF or HF:HNO (1:2) for some minutes at room temperature. Then the domain structure was easy to study. As it can be seen in figure 7.9, the quality of the domains in the +z face, where the periodic electrodes were deposited,

[1] The SNOM measurements were made by J. Lamela and F. Jaque.

is really good, with a duty cycle (D.C.) around 0.4.

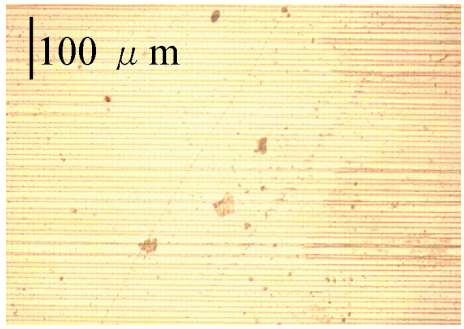

Figure 7.9: +z face of a periodically poled $LiNbO_3$ crystal with an embedded waveguide in the same face, after 10 minutes selective etching. Electrodes were also deposited onto the +z face

The same procedure was repeated for the other α-phase samples that we have mentioned before, that is, with waveguides fabricated in the -z face or with waveguides prepared in both faces. Images after etching of different samples can be seen in figure 7.10, where the homogeneity and the good domain wall quality are clearly apparent. Moreover, the duty cycles in this cases is near 0.5 and the domain penetration fully overpasses the waveguide thickness, as it will be shown in brief.

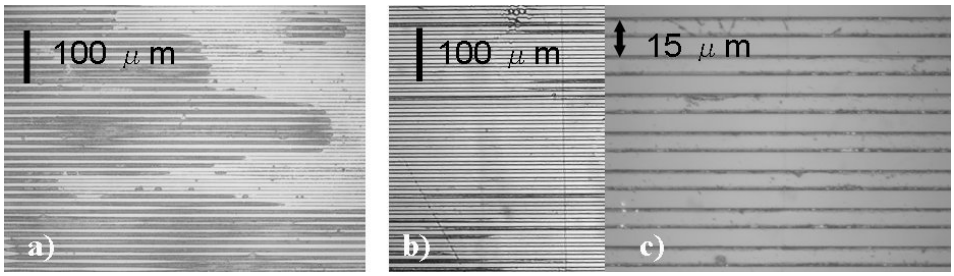

Figure 7.10: -z face after etching: a) Waveguides in both faces, photoresist in -z. b) and c) Waveguide only in -z face. In c), the bigger magnification shows the excellent duty cycle of these samples

In depth analysis of the domains

Our main objective was to obtain a periodical poled waveguide layer. To assess that it had been properly achieved, the depth dynamics of domains across the substrate thickness were also studied. Therefore, the not-structured faces of the periodically poled samples were studied. In figure **??**.a, the not-structure face of sample showed in figure 7.11 is shown. The quality of the domain pattern in this back face is much worse than in the structured one, although some periodicity can be seen. Despite the inhomogeneity of the structure, regions with a D.C. of 0.6 can be discerned.

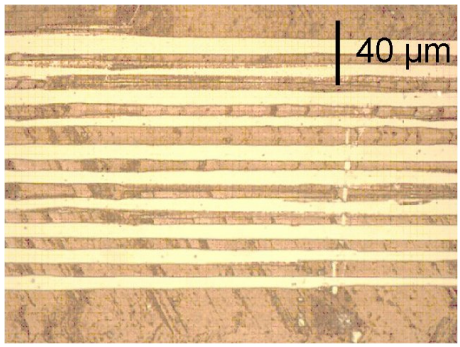

Figure 7.11: The unstructured face of the same periodically poled α-phase waveguide as in figure 7.9 (domain structure of $15\mu m$ lenght) after chemical etching

In order to provide a better insight on the in-depth evolution of the domain switching, the penetration of the domains across the depth of the sample were also studied. Therefore, the polished edge of the sample's halves that had been chemically etched, as it can be seen in figure 7.12. As the etch rate for this edges (which are **y**-faces) is slower than for the **z**-face present in the surface, they were etched for longer times. This in-depth profile also shows that in some areas most of the domains go through the whole crystal and almost the same D.C. is maintained at the unstructured

face.

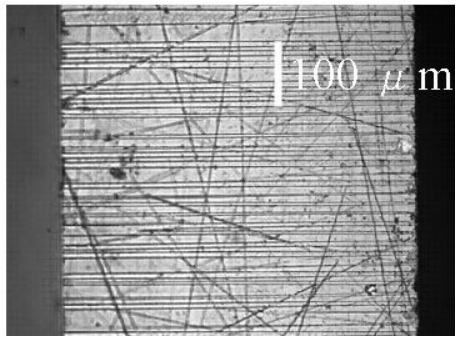

Figure 7.12: The same sample as in figure 7.11 is shown in this picture, but this time the polished edge (**y**-face) is to be seen. The domains along the depth of the substrate show the same periodicity as the unstructured face.

7.2.2 Periodically poled α-phase waveguides: $5\,\mu$m period length

Once the periodic poling of planar α-phase PE waveguides had been successfully achieved with periods of $15\,\mu$m, the next step was to try to fabricate smaller periods. Our aim was to obtain $5\,\mu$m period lengths, just at the reported limit for the possibilities of the standard electrical poling technique [41]. Given that in the former experiments there were no relevant differences between having the structure in the +z or -z face, but an increase of the field required to periodically pole in the second case, for this period lengths the photoresist structure and the waveguide were chosen to be both in the **+z** face.

As long as the poling process is concerned, there were not many differences with the $15\,\mu$m structured samples. The only dissimilarity was found in the shape of the field pulse. On the one hand, it was necessary to increase the peak field responsible for domain nucleation intensity in

order to favor the number of domain seeds in regions without photoresist. On the other hand, the duration of this peak had to be decreased, to avoid the growth of them at that stage. The time where the field was kept above the coercive field was also shorter than in the case of $15\,\mu\mathrm{m}$ structures, because otherwise the domains grew too much and the sample was over-poled. Nevertheless, the duration of the whole voltage waveform was longer than before, because the stabilization field was maintained longer to avoid back-switching.

Characterization of the domain structure within the waveguide

After the periodical poling of the samples, the optical performance of the waveguides were checked. Their light guiding properties were not appreciably modified and diffraction measurements with guided light proved that the correct periodicity was obtained. Then, as in the case of the $15\,\mu\mathrm{m}$ samples, they were cut along their **x** axis in two pieces and one half was etched in HF:HNO (1:2) for some minutes at room temperature to study the domain structure. In figure 7.13, a microscope image of the structured face of one sample can be seen. The quality of the domains in the +z face is very homogeneous and shows an optimum D.C. of about 0.5

In depth analysis of the domains

In the case of the $5\,\mu\mathrm{m}$ periodically poled samples, the not structured face was also imaged after chemical etching with a microscope, as it can be seen in figure 7.14. At difference with the $15\,\mathrm{mum}$ samples, in this case no periodicity was found, but big hexagonal shaped inverted regions.

To study the penetration of the domains into the sample, the edge of one of the pieces obtained after cutting the sample along the **x** axis were

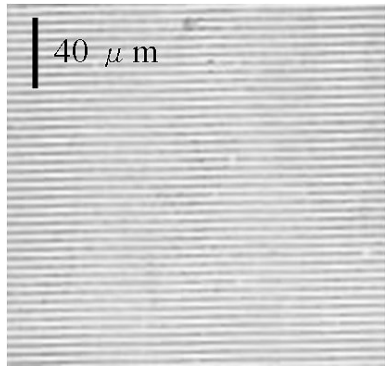

Figure 7.13: **+z** face of a periodically poled planar α-phase waveguide after 10 minutes etching.

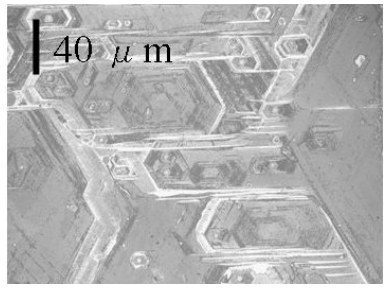

Figure 7.14: The unstructured face of the same periodically poled α-phase waveguide as in figure 7.13 (domain structure of $5\mu m$ lenght) after chemical etching

also etched. The image of this etched **y**-face can be seen in figure 7.15. At difference with the longer period lengths samples, in this case many domain seeds can be found but most of the domains do not go through the whole bulk.

It is quite striking not to found a bigger number of domain seeds in the near the surface, provided that the etching of the structured face showed such a good periodic domain reversal. Therefore, additional selective chemical etching was carried out to investigate the domain penetration. The sample was immersed in acid for longer times and after each etching

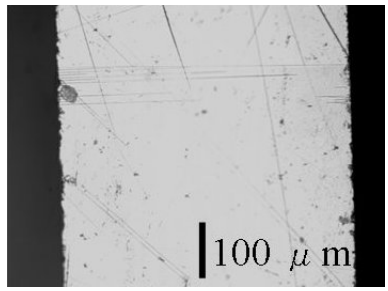

Figure 7.15: The polished edge (**y**-face) of the same sample as figure 7.14 is shown. Some domains can be seen along the depth of the substrate, but most of them are only seeds that do not reach the other face.

experiment, the domain pattern was observed with a microscope and then, the depth of the visualized structure was measured with a profilometer. In figure 7.16, an image of the surface of the sample can be seen after $10\,\mathrm{minutes}$ etching (7.16.a) and after $9\,\mathrm{hours}$(7.16.b). With this method, we have checked that the whole waveguide layer of $2\,\mu\mathrm{m}$ thickness was periodically poled, preserving the domain homogeneity.

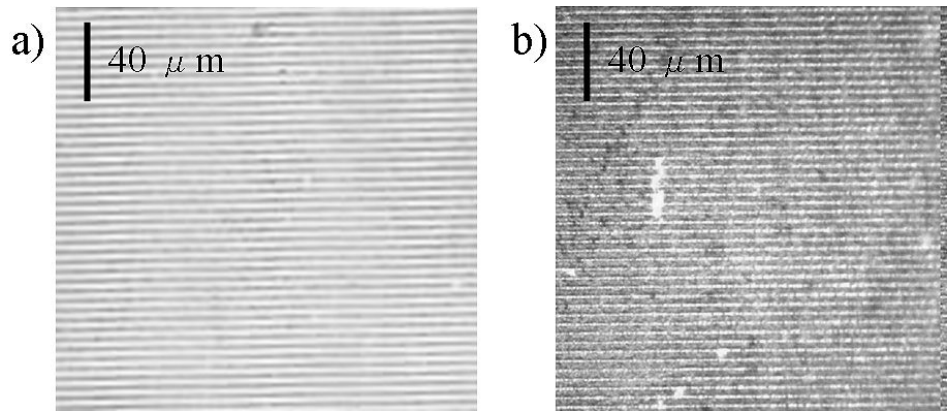

Figure 7.16: **+z** face of a periodically poled planar α -phase waveguide, after $10\,\mathrm{minutes}$ etching. b) Same face after $9\,\mathrm{hours}$ etching, i.e. around $2\,\mu\mathrm{m}$ deep. The homogeneity of the $5\,\mu\mathrm{m}$ period structure is clearly seen.

7.2.3 Discussion

Through this chapter it has been shown that high quality periodic domain inversion in planar α-phase PE waveguides can be made using the less common procedure of waveguide fabrication prior to the electric field polarization, for the first time to our knowledge. This method, already used for Ti-in-diffused waveguides [41], prevents possible degradation of the periodic structure by the proton exchange. With these achievement, one can take advantage not only of the QPM-structure for nonlinear frequency conversion, but also of the higher light intensities present in waveguide configuration, along with the nonlinear coefficients of α-phase waveguides, similar to those of the substrate, and a higher optical damage resistance than congruent $LiNbO_3$.

Down to $5\,\mu\mathrm{m}$ period length domain structures have been fabricated after the waveguide fabrication, with D.C. near 0.5. It has also been studied the penetration of these domains in the substrate, being granted that at least $2\,\mu\mathrm{m}$ were periodically poled. This depth fully covers the waveguide thickness which is sufficient for QPM-SHG within the guiding layer. Decreasing the period length from $15\,\mu\mathrm{m}$ down to $5\,\mu\mathrm{m}$ involves a loss of either periodicity or even the whole structure far from the surface. However, this is not relevant when using guided light, since the duty cycle is maintained across the waveguide thickness.

The reduction of the period length involves a more precise control over the domain nucleation rate and the development of the domain walls, and that was optimized through a number of experiments. Nevertheless, the parameters do not seem to be so critical as when the whole bulk has to be poled.

Finally, the progress of the domains inside the substrate has been also investigated. A subject that is extensively investigated nowadays is the

effect of proton-exchange on $LiNbO_3$ domain inversion [93]. Although it has been mentioned frequently that the presence of protons in the waveguide layer could complicate the electrical periodic poling [86, 93], no significant difference in the case of α-phase (weak exchange of 12%) PE waveguides has been found. In other words, the presence of protons in the waveguide layer has not introduced any appreciable difficulty in the periodical poling of the samples

Light intensity inside the waveguide

In most of the measurements reported in this work, such as optical damage intensity thresholds and photovoltaic currents, the actual light intensity inside the waveguide is a key magnitude. However, an accurate measurement is a subtle matter. In most of these experiments, light is in-coupled and out-coupled via rutile prisms (see section 4.2.4 and 4.2.5 for example). In order to measure the actual light propagating inside the waveguide, the existing methods were too inaccurate and cumbersome to be carried out for each experiment. Therefore, a review of the most employed methods was made, and a new one, more precise and experimentally attainable was proposed. Then, a calibration of our samples with this method was made, in order to avoid further repetitive measurements and simplify the experiments.

.0.4 Measuring the reflected power from the in-coupler

This method consists on the obtainment of the intensity inside the waveguide as the difference between the power of the incoming light, P_i and the power of all the reflected beams from the input prism, P_R. Then, the power inside the waveguide, P_g, becomes

$$P_g \approx P_i - P_R \tag{1}$$

The measurement of all the reflected beams is quite awkward, and it is experimentally impossible to recoil all the power losses produced in the experiment, the method is rather cumbersome. This procedure was used in [90], but when it was repeated in our laboratory, the powers inside the waveguide were up to 3 times greater than those measured by other methods (see below) that seem more reliable.

.0.5 Measuring in- and out coupler

In this second method the intensity inside the waveguide is obtained from the measurement of the incident and output powers (P_i and P_o). Once these values are measured, it is necessary to know the coupling efficiencies, δ_i and δ_o , at the input and output prisms. In most cases, the rather drastic approximation of assuming $\delta_i = \delta_o = \delta$ can be made. Then, the power inside the waveguide takes the form

$$P_g = T_{ap}\delta P_i \tag{2}$$

$$P_o = T_{ap}\delta P_g \tag{3}$$

where T_{ap} is the transmittance at the air-prism interface (about 0.75 for typically used angles). It is easy to see that both the coupling efficiency and the power inside the waveguide can be obtained from the relations mentioned above

$$\delta = \frac{1}{T_{ap}}\sqrt{P_o/P_i} \tag{4}$$

$$P_g = \sqrt{P_i P_o} \tag{5}$$

The main problem with this approximation is that there are a number of requirements on the experimental conditions. To consider that the input and output coupling efficiencies are equivalent, both prisms must have identical geometries and their contacts should be performed as similar as possible. Moreover, the contact area at the input prism should include the incident beam cross section completely, and the profile of the incident beam should match the wave function of the excited mode.

Taking all of these into account, it is not hard to see how the results obtained depend on the completion of the above mentioned requirements. In the whole, the values of δ are overestimated, because δ_i is usually smaller than δ_o, which makes the power inside the waveguide up to two times greater than those measured with the experimental setup described in next section.

Nevertheless, if a focusing lens is used to focus the light in the input contact, the results are substantially improved. In the case of optical damage measurements, a focusing lens of long focal length was used in all the measurements in order to increase the power density in the waveguide, thus the values obtained for the actual power inside the waveguide are quite accurate. But this did not happen in the case of photovoltaic currents measurements, and being this method the one used in our group [4, 66], now the intensity values should be corrected.

.0.6 Measuring the out-coupling efficiency

To overcome both the inaccuracies and the experimental difficulties of the two methods described above, a new method was proposed and implemented in our laboratory. The power inside the waveguide was obtained from the measurement of the coupling efficiency of the out-coupling prism, which is acquired from the power coming out from the polished waveguide edge when the out-coupling prism is placed and when it is removed. As it was shown in equation 3,

$$P_g = \frac{P_o}{T_{ap}\delta_o} \tag{6}$$

The method proposed provides a simple measurement of the coupling efficiency δ_o, which is obtained from the power coming from the polished edge when the second prism is coupled to the waveguide (P_c) and when it is not (P_u). In the first case, the power coming out of the prism (P_o) is also measured. If the prism is coupled, the output power from the guide edge takes the form

$$P_c = T_{ga}(P_g - \delta_o P_g) = T_{ga}P_g(1 - \delta_o) \tag{7}$$

where T_{ga} is the transmittance at the guide-air interface. When the out-coupling prism is not coupled, the power coming from the edge becomes

$$P_u = T_{ga}P_g \tag{8}$$

If one divides 7 by 8, the out-coupling efficiency is obtained as

$$\delta_o = 1 - \frac{P_c}{P_u} \tag{9}$$

which just involves the rate P_c/P_u. Therefore, it is not necessary to measure absolute powers. Moreover, not all the out-coming light has to be collected, which avoids many experimental difficulties, such as scattering due to small defects in the edge. Once the δ_o value is known, one can also determine the in-coupling efficiency at the first prism as

$$\delta_i = \frac{P_o}{P_i T_{ap}^2 \delta_o} \tag{10}$$

With this method, the accuracy obtained for P_g was evaluated by means of successive measurements on the same waveguide, changing the output prism each time, that is, varying δ_o. The values of P_g varied less than 5%, even though some of the measurements were made with extreme conditions, i.e. applying strong or very low pressures at the output contact prism to force different δ_o values (from 0.20 to 0.95)

.0.7 Calibration of the system

The main advantage of the out-coupling method is that one can calibrate the value of δ_o for a given configuration. Once the value of the out-coupling efficiency is known, only the output power P_o has to be measured. In order to obtain a calibration of different setups, method .0.6 was performed several times and then an average over the results was taken.

The first measurements made to confirm the reliability of this calibration were performed by different people, and they were made with different prisms, with and without focusing lenses (spherical and cylindrical), with different waveguides in different configurations. The results obtained after this ample set of experiments can be seen in figure 17.

In this figure a good repeatability for each kind of waveguide can be

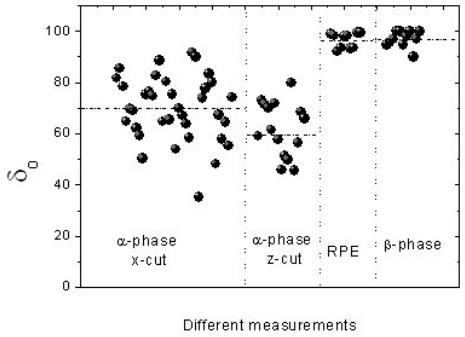

Figure 17: Out-coupling efficiency δ_o obtained for different waveguides performed in different conditions. Dashed lines indicate the average value for each kind of waveguide.

seen, but the values of δ_o differ a lot for different types of waveguides. The calibrated value of δ_o for the different PE waveguides can be found in table 1.

Waveguide	δ_o	error
α, x-cut	0.70	± 0.12
α, z-cut	0.61	± 0.11
RPE	0.97	± 0.03
β	0.97	± 0.03

Table 1: Out-coupling efficiency calibrated for different PE-$LiNbO_3$ waveguides

This measurements were also performed with zinc and titanium in-diffused waveguides, but the coupling efficiencies were found smaller than in the case of PE waveguides, probably due to their worse surface quality. As far as α phase waveguides are concerned, if a better accuracy than $\pm 12\%$ is needed, the out-coupling efficiency should be measured each time with the technique described in .0.6.

Two examples of the reliability of the proposed method are shown in

figures 18 and 19. These are two cases of practical interest, involving the measurement of photovoltaic currents versus intensity and the photorefractive damage.

In figure 18 two measurements of the photovoltaic current in an α-phase PE waveguide is plotted as a function of the light intensity in the waveguide, I_g. In each case, the intensity is determined by a different method, 18.a with the calibrated value of δ_o 0.70 and in figure 18.b with the direct measurement of the coupling efficiency.

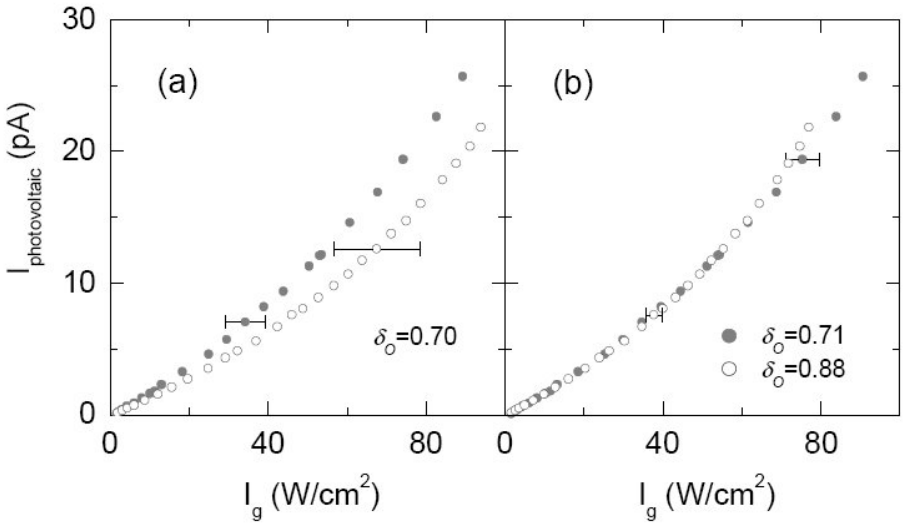

Figure 18: Two sets of measurements of the photovoltaic currents versus the intensity in the waveguide, being this intensity calculated by a) the calibrated δ_o value and b)direct measurement of the coupling efficiency.

In the case of figure 19, the optical damage threshold for an α-phase PE waveguide has been measured. The output power has been plotted versus the intensity in the waveguide, I_g. Again, two measurements have been carried out, being I_g determined with the calibrated value in 19.a and with a direct measurement of the coupling efficiency in figure 19.b.

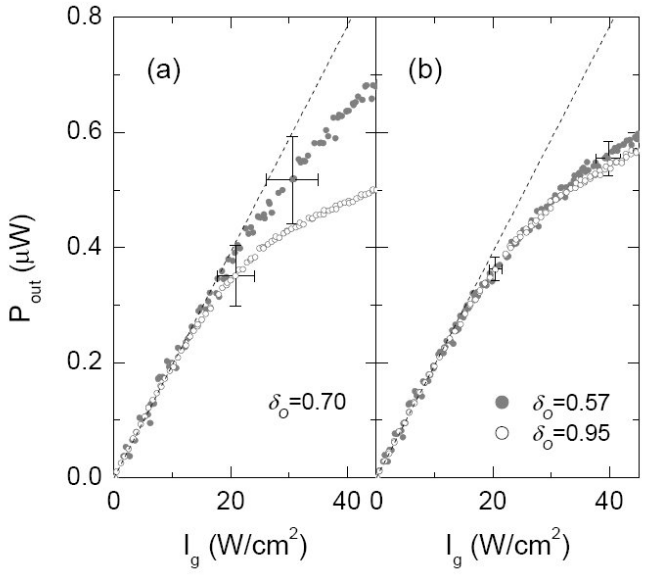

Figure 19: Two sets of measurements of the optical damage threshold of an α waveguide, being the intensity inside the waveguide calculated by a) the calibrated δ_o value and b)direct measurement of the coupling efficiency.

These results show that the light intensity actually propagating inside the waveguide can be obtained with the proposed technique with a very high accuracy. Moreover, the calibration of the system provides also a good measurement of the light intensity inside the waveguide, although it is less precise (with errors around 15%). But this accuracy is enough for most practical applications.

Conclusions

In this work, the following contributions to the nonlinear characterization of a wide variety of optical waveguides fabricated by proton exchange, metal-in-diffusion and ion irradiation in $LiNbO_3$ have been made:

- The second order nonlinear coefficients of a wide variety of $LiNbO_3$ waveguides have been obtained and compared.
  - α phase PE and Zn-in-diffused waveguides present excellent second order nonlinear susceptibilities, around $70 - 100\%$ of the value of congruent $LiNbO_3$, being comparable to Ti-in-diffused waveguides in this feature.
  - The new ion irradiated waveguides present also quite high nonlinear coefficients, around $60 - 70\%$ of the substrate, making these samples very promising for nonlinear applications.
- A comparative study of the optical damage thresholds in different waveguides has been carried out.
  - α phase PE and Zn-in-diffused waveguides show higher optical damage thresholds than bulk $LiNbO_3$, clearly higher than those of Ti-in-diffused waveguides and congruent $LiNbO_3$.
  - One the photorefractive damage mechanisms, the photovoltaic effect, has been studied in PE and Zn-in-diffused waveguides.

A superlineal behaviour with the light intensity has been found and it has been demonstrated that this behaviour is related to the antisites present in $LiNbO_3$. Then, the influence of these antisites in the optical damage effect has been demonstrated.

  - Optical damage has been investigated in α phase waveguides fabricated in z-cut substrates and, varying the fabrication time, the optical damage threshold has been increased 10 times.
  - Periodically poled optical waveguides and waveguides fabricated in periodically poled $LiNbO_3$have been also measured, and no difference with optical waveguides fabricated in single domain $LiNbO_3$ has been found.
  - Preliminary measurements of optical damage in α phase PE channel waveguides have been carried out. These results show that this configuration present an optical damage threshold over three times larger than planar α-phase PE waveguides.

- The electrical field periodic poling technique has been developed and adapted for α phase waveguides, and periodically poled samples with periods down to $5\,\mu\mathrm{m}$ have been obtained. These samples present a good homogeneity and a very good quality (D.C. ~ 0.5).

- The outstanding properties obtained in this study concerning nonlinear susceptibility, low optical damage, and the posiblity of periodical poling allow us to consider α-phase PE as excellent waveguides for second order nonlinear applications.

The different studies carried out in this Thesis work have resulted in the following publications:

[46, 43, 45, 44, 42, 164, 55, 66, 5].

Conclusiones

En este trabajo, se ha contribuido a la caracterización no lineal de una gran variedad de guías ópticas en $LiNbO_3$ fabricadas mediante intercambio protónico, difusión de metales e irradiación iónica, obteniendo las siguientes conclusiones:

- Se han determinado y comparado los coeficientes no lineales de segundo orden. Resultados relevantes son:

  - Las guías por intercambio protónico en fase α y las guías fabricadas por difusión de Zn presentan unos excelentes valores en sus susceptibilidades no lineales, del orden del $70 - 100\%$ del valor del sustrato, siendo en este aspecto comparables con las guías fabricadas por difusión de titanio.

  - Nuevas guías, fabricadas por irradiación iónica, presentan también unos apreciables coeficientes no lineales de segundo orden, entre el $60 - 70\%$ del valor del sustrato, lo que hace que estas guías sean muy prometedoras para aplicaciones no lineales.

- Se ha realizado un estudio comparativo de los umbrales de daño óptico en guías $LiNbO_3$.

- Las guías en fase α y las de difusión de Zn presentan altos umbrales de daño óptico, claramente por encima de las guías de Ti y del sustrato.
- Para investigar los mecanismos de daño fotorrefractivo, se ha estudiado el efecto fotovoltaico en estas guías (de Zn y en fase α). Se ha obtenido un comportamiento súper lineal de la corriente fotovoltaica con la intensidad luminosa, y se ha probado su relación con la presencia de antisitios. De este modo, ha quedado patente la importancia de estos antisitios en el daño óptico.
- Dado que son especialmente idóneas para aplicaciones no lineales de segundo orden, se ha investigado con mayor profundidad el daño óptico en guías PE en fase α. Específicamente:
  - Se ha investigado el daño óptico en guías en fase α sobre sustratos en corte z, y mediante la variación del tiempo de fabricación se han conseguido aumentar el umbrales hasta 10 veces.
  - Se han hecho medidas en guías periódicamente polarizadas, así como en guías fabricadas en sustratos periódicamente polarizados, obteniéndose los mismos resultados que en guías fabricadas sobre sustratos monodominio.
  - Medidas preliminares de daño óptico en guías PE en fase α acanaladas han mostrado unos umbrales de más de tres órdenes de magnitud que los hallados en guías planares del mismo tipo.

- Se ha puesto a punto una técnica de polarización eléctrica de guías en fase α, con la que se han conseguido estructuras periódicamente polarizadas con períodos de tan solo $5\,\mu\mathrm{m}$. Éstos presentan muy buena calidad (D.C. ~ 0.5) y homogéneos.

- Las buenas propiedades obtenidas en este estudio en cuanto a susceptibilidad de segundo orden, bajo daño óptico y la posibilidad de polarizarlas periódicamente, convierten a las guías por intercambio protónico en fase α en guías excelentes para aplicaciones no lineales de segundo orden.

Los distintos estudios llevados a cabo a lo largo de esta Tesis han sido publicados en los artículos que aparecen como referencias:

[46, 43, 45, 44, 42, 164, 55, 66, 5].

Bibliography

[1] F. Abdi, M. Aillerie, M. Fontana, P. Bourson, T. Volk, B. Maximov, S. Sulyanov, N. Rubinina, M. Wöhlecke. «Influence of zn doping on electrooptical proerties and structure parameters of lithium niobate crystals». *Appl. Phys. B* **68**:795 – 799 (1999).

[2] A. Adibi, K. Buse, D. Psaltis. «Multiplexing holograms in $LiNbO_3$:fe:mn crystals». *Optics Lett.* **24**(10):652–654 (1999).

[3] F. Agulló-López, J. M. Cabrera, F. Agulló-Rueda. *Electrooptics. Phenomena, Materials and Applications*. Academic Press Inc., San Diego, CA (USA) (1994).

[4] A. Alcázar, J. Rams, J.M. Cabrera, F. Agulló-López. «Light-induced damage mechanisms in α-phase proton-exchanged $LiNbO_3$ waveguides». *Appl. Phys. B* **68**:989–993 (1999).

[5] A. Alcázar de Velasco, **O. Caballero**, G. de la Paliza, A. García-Cabañes, M. Carrascosa, J. M. Cabrera. «Optical damage and photovoltaic current in proton-exchanged $LiNbO_3$ waveguides». *TOPS* **87**:376 – 380 (2003).

[6] Ángel Alcázar de Velasco. *Daño Óptico En Guías de Onda PE:LiNbO$_3$*. Ph.D. thesis, Universidad Autónoma de Madrid (2004).

[7] J. Amin, V. Pruneri, J. Webjörn, P. St. J. Russell, D. C. Hanna, J. S. Wilkinson. «Blue light generation in a periodically poled ti:$LiNbO_3$ channel waveguide». *Optics communications* **135**:41 – 44 (1997).

[8] N. Argiolas, M. Bazzan, C. Sada. «A study on the periodicity of PPLN grown by the offcenter czochralski technique». *J. of Cryst. Growth* **249**:275 – 282 (2002).

[9] L. Arizmendi. Ph.D. thesis, Universidad Autónoma de Madrid (1983).

[10] L. Arizmendi. «Simple holographic method for determination of Li/Nb ratio and homogeinity of $LiNbO_3$ crystals». *J. of Appl. Phys.* **64**(9):4654–4656 (1988).

[11] L. Arizmendi, J. M. Cabrera. «Optical absorption, excitation, and emission spectra of eu^{3+} in $LiNbO_3$». *Phys. Rev. B* **31**:7138 – 7145 (1985).

[12] J.A. Armstrong, N. Bloembergen, J. Ducuing, P.S. Pershan. «Interactions between light waves in a nonlinear dielectric». *Phys. Rev.* **127**(6):1918 (1962).

[13] A. Ashkin, G. D. Boyd, J. M. Dziedzic, R. G. Smith, A. A. Ballman, J. J. Levinstein, K. Nassau. «Optically-induced refractive index inhomogeneities in $LiNbO_3$ and $LiTaO_3$». *Appl. Phys. Lett.* **9**:72 (1966).

[14] M. Asobe, O. Tadanaga, H. Miyazawa, Y. Nishida, H. Suzuki. «Wavelength conversion devices using quasi-phase-matched $LiNbO_3$». *NTT Tech. Rev.* **1**(1):59 – 67 (2003).

[15] Masaki Asobe, Osamu Tadanaga, Tsutomu Yanagawa, Hiroki Itoh, Hiroyuki Suzuki. «Reducing photorefractive effect in periodically poled ZnO- and MgO- doped $LiNbO_3$ wavelength converters». *Appl. Phys. Lett.* **78**:3163–3165 (2001).

[16] A. A. Ballman. «Growth of piezoelectric and ferroelectric materials by the Czochralski technique». *J. Am. Ceram. Soc.* **48**:112 (1965).

[17] Cynthia Baron, Hsing Cheng, Mool C. Gupta. «Domain inversion in $LiTaO_3$ and $LiNbO_3$ by electric field application on chemically patterned crystals». *Appl. Phys. Lett* **68**(4):481 – 483 (1996).

[18] T. Bartholomäus, K. Buse, C. Deuper, E. Krätzig. «Pyroelectric coefficients of $LiNbO_3$ crystals of different compositions». *Phys. Stat. Sol. (a)* **142**:K55–K57 (1994).

[19] R. G. Batchko, G. D. Miller, V. Ya. Shur, E. I. Rumyantsev, M. M. Fejer, R. L. Byer. «Domain patterning in lithium niobate using spontaneous backswitching». *SPIE* **3610**:36 (1999).

[20] I. Baumann, P. Rudolph, K. Krabe, R. Schalge. «Orthoscopic investigation of the axial optical and compositional homogeneity of Czochralski grown $LiNbO_3$ crystals». *J. Cryst. Growth* **128**:903–908 (1993).

[21] G. G. Bentini, M. Bianconi, M. Chiarini, L. Correra, C. Sada, P. Mazzoldi, N. Argiolas, M. Bazzan, R. Guzzi. «Effect of low dose high energy O^{3+} implantation on refractive index and linear electro-optic properties in x-cut $LiNbO_3$: Planar waveguide formation and characterization». *J. Appl. Phys.* **92**(11):6477–6483 (2002).

[22] G. G. Bentini, M. Bianconi, L. Correra, M. Chiarini, P. Mazzoldi, C. Sada, N. Argiolas, M. Bazzan, R. Guzzi. «Damage effects produced in the near-surface region of x-cut $LiNbO_3$ by low dose, high energy implantation of nitrogen, oxygen, and fluorine ions.» *J. Appl. Phys* **96**:242 (2004).

[23] D. Berben, K. Buse, S. Wevering, P. Herth, M. Imlay, Th. Woike. «Lifetime of small polarons in iron-doped lithium-niobate crystals». *J. Appl. Phys.* **87**(3):1034 – 1041 (2000).

[24] J. G. Bergman, A. Ashkin, A. A. Ballman, J. M. Dziedzic, H. V. Levinstein, R. G. Smith. «Curie temperature, birrefringence and phase-matching temperature variations in $LiNbO_3$ as a function of melt stoichiometry». *Appl. Phys. Lett.* **12**(3):92–94 (1968).

[25] V. Bermúdez, F. Caccavale, C. Sada, F. Segato, E. Diéguez. «Etching effect on periodic domain structures of lithium niobate crystals». *J. Crystal Growth* **191**:589 – 593 (1998).

[26] V. Bermúdez, D. Callejo, F. Caccavale, E. Diéguez. «On the effect of li diffusion in er-doped bulk periodic poled lithium niobate crystals». *J. Crystal Growth* **205**:328 – 332 (1999).

[27] V. Bermúdez, D. Callejo, F. Caccavale, F. Segato, F. Agulló-Rueda, E. Diéguez. «On the compositional nature of bulk doped periodic poled lithium niobate crystals». *Sol. State Comm.* **114**(10):555 – 559 (2000).

[28] V. Bermúdez, D. Callejo, E. Diéguez. «On the cooling effect in the formation of periodic poled lithium niobate crystals grown by cz technique». *J. Crystal Growth* **207**:303 – 307 (1999).

[29] V. Bermúdez, P. S. Dutta, M. D. Serrano, E. Diéguez. «In situ poling of $LiNbO_3$ bulk crystal below the curie temperature by application of electric field after growth». *J. Crystal Growth* **169**:409–412 (1996).

[30] V. Bermúdez, A. Gil, L. Arizmendi, J. Colchero, A. M. Baró, E. Diéguez. «Techniques of observation and characterization of the domain structure in periodically poled lithium niobate». *J. Mater. Res* **15**(12):2814 – 2821 (2000).

[31] A. R. Betts, C. W. Pitt. «Growth of thin-film lithium niobate by molecular beam epitaxy». *Electron. Lett.* **21**:960–962 (1985).

[32] J. Blümel, E. Born, Th. Metzger. «Solid state NMR study supporting the lithium vacancy model in congruent lithium niobate». *J. Phys. Chem. Solids* **55**(7):589–593 (1994).

[33] W. Bollmann, H. J. Stöhr. «Incorporation and mobility of OH^- ions in $LiNbO_3$ crystals». *Phys. Stat. Sol. (a)* **39**:477–483 (1977).

[34] P. F. Bordui, R. G. Norwood, C. D. Bird, G. D. Calvert. «Compositional uniformity in growth and poling of large-diameter lithium niobate crystals». *J. Crystal Growth* **113**:61–68 (1991).

[35] P. F. Bordui, R. G. Norwood, D. H. Jundt, M. M. Fejer. «Preparation and characterization of off-congruent lithium niobate crystals». *J. Appl. Phys.* **71**(2):875–879 (1992).

[36] M.L. Bortz, S.J. Field, M.M. Fejer, D.W. Nam, R.G. Waarts, D.F. Welch. «Noncritical quasi-phase-matched second harmonic generation in an annealed proton-exchanged $LiNbO_3$ waveguide». *IEEE Transactions on Quant. Electr.* **30**:2953 – 2960 (1994).

[37] R. W. Boyd. *Nonlinear Optics*. Academic Press, California, USA (1992).

[38] A.M. Bratkovsky, A. P. Levanyuk. «Easy collective polarization switching in ferroelectrics». *Phys. Rev. Lett.* **85**(21):4614 (2000).

[39] S. Breer, K. Buse. «Wavelength demultiplexing with volume phase holograms in photorefractive lithium niobate». *Appl. Phys. B* **66**:339–345 (1998).

[40] R. Brooks, P. D. Townsend, D. E. Hole, D. Callejo, V. Bermúdez, E. Diéguez. «Domain wall width of lithium niobate poled as growth». *J. Physics D* **36**:1 – 6 (2003).

[41] A. C. Busacca, C. L. Sones, R. W. Eason, S. Mailis. «First-order quasi-phase-matched blue light generation in surface-poled ti:indiffused lithium niobate waveguides». *Appl. Phys. Lett.* **84**(22):4430 – 4432 (2004).

[42] O. Caballero, A. Alcázar, J. Herrero, J. Carnicero, C. Ong, M. Domenech, G. Lifante, A. García-Cabañes, J. M. Cabrera, M. Carrascosa. «Comparative study of optical damage and photovoltaic currents in planar LiNbO3 waveguides». *Proc. SPIE* **5840**:695 (2005).

[43] O. Caballero, G. de la Paliza, A. García-Cabañes, M. Carrascosa, M. Domenech, G. Lifante. «Second order susceptibilities and electro-optic coefficients of zn-indiffused $LiNbO_3$ waveguides». *Ferroelectrics* p. to be published (2007).

[44] O. Caballero, A. García-Cabañes, J. Carnicero, M. Carrascosa, F. Agulló-López, J. Olivares, A. García-Navarro, G. García. «Nonlinear and photorefractive characterisation of highly confined $LiNbO_3$ waveguides prepared by high-energy, low-fluence ion irradiation». *TOPS* **99**:179 (2005).

[45] O. Caballero-Calero, A. García-Cabañes, J. M. Cabrera, M. Carrascosa, A. Alcázar. «Optical damage in x-cut proton exchanged LiNbO3 planar waveguides». *J. Appl. Phys.* **100**:093103 (2006).

[46] O. Caballero-Calero, M. Kösters, T. Woike, K. Buse, A. García-Cabañes, M. Carascosa. «Electric field periodical poling of lithium niobate crystals alter soft-proton-exchanged waveguide fabrication». *Appl. Phys. B* p. accepted for publication (2007).

[47] J.M. Cabrera, F. Agulló-López, F.J. López. *Óptica Electromagnética II: Materiales Y Aplicaciones*, volume 2. Addison-Wesley / Universidad Autónoma de Madrid (2000).

[48] J.M. Cabrera, J. Olivares, M. Carrascosa, J. Rams, R. Müller, E. Diéguez. «Hydrogen in lithium niobate». *Advances in Phys.* **45**(5):349–392 (1996).

[49] C. Canali, A. Carnera, G. D: Mea, P. Mazzoldi, S. M. Al Shukri, A. C. G. Nutt, R. M. De la Rue. «Structural characterization of proton exchanged $LiNbO_3$ optical waveguides». *J. Appl. Phys.* **59**(8):2643–2649 (1986).

[50] E. Cantelar, R. E. Di Paolo, J. A. Sanz-García, P. L. Pernas, R. Nevado, G. Lifante, F. Cussó. «Second harmonic generation in zn-diffused periodically poled $LiNbO_3$ channel waveguides». *Appl. Phys. B* **73**:515 – 517 (2001).

[51] E. Cantelar, J. A. Sanz-García, F. Cussó. «Growth of $LiNbO_3$ co-doped with er^{3+}/yb^{3+}». *J. Cryst. Growth* **205**:196 – 201 (1999).

[52] E. Cantelar, G. A. Torchia, J. A. Sanz-García Nad P. L. Pernas, F. Jaque, G. Lifante, F. Cussó. «CW, broadly tunable, red, green and blue light generation in aperiodically poled zn-diffused $LiNbO_3$:Er/Yb channel waveguides». *ECIO'03* **1**:209 – 211 (2003).

[53] X. Cao, R. Srivastava, R. V. Ramaswamy. «Simultaneous blue and green second harmonic generation in quasiphase matched $LiNbO_3$ waveguide». *Appl. Phys. Lett.* **60**(26):3280 – 3282 (1992).

[54] X. Cao, R. Srivastava, R. Ramaswany. «Efficient quasi-phase-matched blue second-harmonic generation in $LiNbO_3$ channel waveguides by a second-order grating». *Opt. Lett.* **17**(8):592 – 594 (1992).

[55] J. Carnicero, O. Caballero, M. Carrascosa, J.M. Cabrera. «Superlinear photovoltaic currents in $LiNbO_3$: Analyses under the two-center model». *Appl. Phys. B* **79**:351 – 358 (2004).

[56] J. Carnicero, M. Carrascosa, A. García-Cabañes, F. Agulló-López. «Site correlation effects in the dynamics of iron impurities (fe^{2+}/fe^{3+}) and antisite defects (nb^{4+}/nb^{5+}) after short pulse excitation in $LiNbO_3$». *Phys. Rev. B* **72**:245108 (2005).

[57] J. Carnicero, A. Méndez, M. Carrascosa, A. García-Cabañes. «Photorefractive alpha-phase proton exchanged $LiNbO_3$ waveguides prepared on iron doped substrates.» *Ferroelectrics* p. Accepted for publication (2007).

[58] M. Carrascosa, F. Agulló-López. «Optimization of the developing for fixed gratings in $LiNbO_3$». *Opt. Comm.* **126**:240 (1996).

[59] J. R. Carruthers, G. E. Peterson, M. Grasso, P. M. Brindenbaugh. «Nonstoichiometry and crystal growth of lithium niobate». *J. Appl. Phys.* **42**(5):1846–1851 (1971).

[60] P. J. Chandler, F. L. Lama. «A new approach to the determination of planar waveguide profiles by means of a non-stationary mode index calculation». *Opt. Acta* **33**(2):127–143 (1986).

[61] L. Chanvillard, P. Aschièri, P. Baldi, D. B. Ostrowski, M. De Micheli, L. Huang, D. J. Bamford. «Soft proton exchange on periodically poled $LiNbO_3$: A simple waveguide fabrication process for highly efficient nonlinear interactions». *Applied Physics Letters* **76**:1089–1091 (2000).

[62] Y. L. Chen, J. J. Xu, X. Z. Zhang, Y. F. Kong, X. J. Chen, G. Y. Zhang. «Ferroelectric domain inversion in near stoichiometric lithium niobate for high efficiency blue light generation». *Appl. Phys. A* **74**:187–190 (2002).

[63] K. Chow, H. G. McKnight, L. R. Rothrock. «The congruently melting composition of $LiNbO_3$». *Mat. Res. Bull.* **9**:1067 (1974).

[64] J. Czochralski. «Ein neues verfahren zur messung der kristallisationsgeschwindigheit der metalle». *Z. Phys. Chemie* **92**:219–221 (1918).

[65] G. de la Paliza. *Guías de onda PE:$LiNbO_3$ para aplicaciones fotorrefractivas*. Ph.D. thesis, Univ. Autónoma de Madrid (2004).

[66] G. de la Paliza, O. Caballero, A. García-Cabañes, M. Carrascosa, J.M. Cabrera. «Superlinear photovoltaic currents in proton exchanged $LiNbO_3$ waveguides». *Appl. Phys. B* **76**:555 – 559 (2003).

[67] M. de Micheli, D. B. Ostrowsky, J. P. Barety, C. Canali, A. Carnera, G. Mazzi, M. Papuchon. «Crystalline and optical quality of proton exchanged waveguides». *J. Lightw. Technol.* **4**(7):743–745 (1986).

[68] J. A. de Toro, M. D. Serrano, A. García-Cabañes, J. M. Cabrera. «Accurate interferometric measurement of electro-optic coefficients: Application to quasi-stoichiometric $LiNbO_3$». *Optics Comm.* **154**:23–27 (1998).

[69] M. DiDomenico, S. H. Wemple. «Oxygen-octaedra ferroelectrics. i. theory of electro-optical and nonlinear optical effects». *J. Appl. Phys.* **46**(2):720–734 (1969).

[70] M. Domenech, G. Lifante. «Continuous wave laser operation at 1.3 microns in nd^{3+}-doped zn:$LiNbO_3$ channel waveguides.» *Appl. Phys. Lett* **84**(17):3271 – 3273 (2004).

[71] M. Domenech, R. E. Di Paolo, G. Lifante, F. Cusso. «Blue light by SHG in diode pumped $LiNbO_3$ waveguides». *Phys. Stat. Sol* **192**(1):135 – 138 (2002).

[72] H. Donnerberg, S. M. Tomlinson, C. R. A. Catlow, O. F. Schirmer. «Computer-simulation studies of intrinsic defects in $LiNbO_3$». *Phys. Rev. B* **40**(17):11909–11916 (1989).

[73] R.C. Eckardt, H. Masuda, Y. X. Fan, R. L. Byer. «Absolute and relative nonlinear optical coefficients of KDP, MgLN and KTP measured by phase-matched second-harmonic generation». *IEEE J. Quant. Electr.* **26**(5):922 (1990).

[74] M. Falk, K. Buse. «Thermo-electric method for nearly complete oxidation of highly iron-doped lithium niobate crystals». *Appl. Phys. B* **81**:853 – 855 (2005).

[75] Martin M. Fejer, G. A. Magel, Dieter H. Jundt, Robert L. Byer. «Quasi-phase-matched second harmonic generation: Tuning and tolerances». *J. Quant. Electr.* **28**(11):2631 – 2654 (1992).

[76] X. Feng, T. Shao, J. Zhang. «An infrared absorption band caused by H^+ implantation in $LiNbO_3$ crystals». *J. Phys. Condens. Matter* **3**:4145–4150 (1991).

[77] H. G. Festl, P. Hertel, E. Krätzig, R. Von Baltz. «Investigations of the photovoltaic tensor in doped $LiNbO_3$». *Phys. Stat. Sol. (b)* **113**:157 (1982).

[78] B. M. Foley, P. Melman, K. T. Vo. «Novel loss measurement technique for optical waveguides by imaging of scattered light». *Electr. Lett.* **28**(6):584 – 585 (1992).

[79] P.A. Franken, J. F. Ward. «Optical harmonics and nonlinear phenomena». *Rev. Modern Phys.* **35**(1):23 – 39 (1963).

[80] V. M. Fridkin, R. M. Magomadov. «Anomalous photovoltaic effect in $LiNbO_3$:fe in polarized light». *JETP Lett.* **30**:686 (1979).

[81] M. Fujimura, M. Sudoh, K. Kintaka, T. Suhara, H. Nishihara. «Resonant waveguide quasi-phase-matched SHG devices with electrooptic phase-modulator for tuning». *IEEE J. Select. Topics Quant. Electr.* **2**(2):396 (1996).

[82] M. Fujimura, T. Suhara, H. Nishihara. «Ferroelectric domain inversion induced by SiO_2 cladding for lithium niobate waveguide second harmonic generation». *Electr. Lett.* **27**(13):1207 (1991).

[83] T. Fujiwara, R. Srivastava, X. Cao, R. V. Ramaswamy. «Comparison of photorefractive index change in proton exchanged and ti-diffused $LiNbO_3$ waveguides». *Opt. Lett.* **18**:346 (1993).

[84] T. Fujiwara, A. Terashima, H. Mori. «Photorefractive deffects in ti-diffused channel waveguides using $LiNbO_3$ substrate with reduced optical absorption». *Appl. Phys. Lett* **55**:2781 (1989).

[85] T. Fukuda, H. Hirano. «Growth and characteristics of $LiNbO_3$ plate crystals». *Mater. Res. Bull.* **10**(8):801–806 (1975).

[86] Katia Gallo, Marc de Micheli, Pascal Baldi. «Parametric fluorescence in periodically poled $LiNbO_3$ buried waveguides». *Appl, Phys. Lett.* **80**:4492–4494 (2002).

[87] G. García, J. Olivares, F. Agulló-López, A. García-Navarro, F. Agulló-Rueda, A. García-Cabañes, M. Carrascosa. «Effect of local rotations on the optical response of $LiNbO_3$: Application to ion-beam damage.» *Europhys. Lett.* **2**:10375 (2006).

[88] A. García-Navarro, F. Agulló-López, M. Bianconi, J. Olivares, G. García. «Kinetics of ion-beam damage in lithium niobate». *J. Appl. Phys.* **101**(1) (2007).

[89] A. M. Glass, D. Van der Linde, T. J. Negran. «High voltage bulk photovoltaic effect and the photorefractive process in $LiNbO_3$». *Appl. Phys. Lett.* **25**:233–235 (1974).

[90] E. Glavas, J. M. Cabrera, P. D. Townsend. «A comparison of optical damage in different types of $LiNbO_3$ waveguides». *J. Phys. D: Appl. Phys* **22**:611–616 (1989).

[91] E. Glavas, J. M. Cabrera, P. D. Townsend, G. Droungas, M. Dorey, K.K. Wong, L. Allen. «Optical damage resistance of ion implanted LiNbO3 waveguides». *Electron. Lett.* **23**:73 (1987).

[92] B. C. Grabmaier, W. Wersing, W. Koestler. «Properties of undoped and MgO-doped $LiNbO_3$; correlation to the defect structure». *J. Crystal Growth* **110**:339–347 (1991).

[93] S. Grilli, C. Canalias, F. Laurell, P. Ferraro, P. De Natale. «Control of lateral domain spreading in congruent lithium niobate by selective proton exchange». *Appl. Phys. Lett.* **89**:032902 (2006).

[94] P. Günter, editor. *Nonlinear Optical Effects and Materials*. Springer (1999).

[95] P. Günter, J.-P. Huignard. *Photorefractive Materials and Applications*, volume I. Springer-Verlag, USA (1988).

[96] L. Hafid, F. M. Michel-Calendini. «Electronic structure of $LiNbO_3$: Densities of states, optical anisotropy and spontaneous polarisation calculated from the xα molecular orbital method». *J. Phys. C: Solid State Phys* **19**:2907–2917 (1986).

[97] P. W. Haycock, P. D. Townsend. «A method of poling $LiNbO_3$ and $LiTaO_3$ below t_c». *Appl. Phys. Lett* **48**(11):698 – 700 (1986).

[98] B. Hecht, B. Sick, U. P. Wild, V. Deckert, R. Zenobi, O. J. F. Martin, D. W. Phol. «Scanning near-field optical micrsocopy with aperture probes: Fundamentals and applications». *J. Chem. Phys* **112**(8):7761 (2000).

[99] P. Hertel, H. P. Menzler. «Improved inverse WKB method procedure to reconstruct refractive index profiles of dielectric planar waveguides». *Appl. Phys. B* **44**:75–80 (1987).

[100] M. Houé, P. D. Townsend. «Thermal polarization reversal of lithium niobate». *Appl. Phys. Lett* **66**:2667 (1995).

[101] H. Hu, F. Lu, F. Chen, B Shi, K. Wang, Ding-Yu Shen. «Monomode optical waveguide in lithium niobate formed by MeV si^+ ion implantation». *Journal of applied physics* **89**(9):5224 – 5226 (2001).

[102] J. Hukriede, B. Gather, D. Kip, E. Krätzig. «Copper diffusion into lithium niobate». *Phys. Stat. Sol. (a)* **172**:R3–R4 (1999).

[103] N. Iyi, K. Kitamura, F. Izumi, J. K. Yamomoto, T. Hayashi, H. Asano, S. Kitamura. «Comparative study of defect structures in lithium niobate with different compositions». *J. Solid State Chem.* **101**(2):340–352 (1992).

[104] J. Jackel, D. H. Olson, A. M. Glass. «Optical damage resistance of monovalent ion diffused $LiNbO_3$ and $LiTaO_3$ waveguides». *J. Appl. Phys* **52**:4855 (1981).

[105] J. L. Jackel, C. E. Rice, J. J. Veselka. «Proton exchange for high-index waveguides in $LiNbO_3$». *Appl. Phys. Lett.* **41**(7):607–608 (1982).

[106] J.L. Jackel, V. Ramaswamy, S.P. Lyman. «Elimination of out-diffused surgace guiding in titanium-diffused $LiNbO_3$». *Appl. Phys. Lett.* **38**:509 – 511 (1981).

[107] F. Jaque, T.P.J. Hana, G. Lifante. «Comparative study of the singularity in the optical properties of congruent doped $LiNbO_3$ crystals». *Journal of Luminiscence* **102**:248 – 252 (2003).

[108] F. Jermann, E. Krätzig. «Charge transport processes in $LiNbO_3$:fe at high intensity laser pulses». *Applied Physics A* **55**:114 – 118 (1992).

[109] F. Jermann, J. Otten. «Light-induced charge transport in $LiNbO_3$: Fe at high light inensities». *Journal of Optical Society of America* **10**(11):2085 – 2092 (1993).

[110] D. H. Jundt, M. M. Fejer, R. L. Beyer. «Optical properties of lithium-rich lithium niobate fabricated by vapor transport equilibration». *IEEE J. Quantum Electron.* **26**(1):135–138 (1990).

[111] D. H. Jundt, G. A. Magel, M. M. Fejer, R. L. Byer. «Periodically poled $LiNbO_3$ for high-efficiency second-harmonic generation». *Applied Physics Letters* **59**(21):2657 – 2659 (1991).

[112] H. Kanbara, H. Itoh, M. Asobe, K. Noguchi, H. Miyazawa, T. Yanagawa, I. Yokohama. «All-optical switching». *IEEE Photonics Tech. Lett.* **11**(3):328 (1999).

[113] R. W. Keys, A. Loni, R. M. de la Rue. «Cerenkov second harmonic generation in proton exchanged lithium niobate waveguides». *Journal of modern optics* **37**(4):545 – 553 (1990).

[114] B. Kim, B.K. Rhee, M. Cha. «Simple measurement of space-charge field in a $LiNbO_3$ crystal doped with 0.65 mol% MgO using second harmonic generation». *Optics Communications* **173**:377 – 380 (2000).

[115] Dae M. Kim, J. G. Gallagher, T. A. Rabson, F. K. Tittel. «Intensity enhanced bulk photovoltaic effects in $LiNbO_3$:fe». *Applied Physics* **17**:413 – 416 (1978).

[116] S. Kim, V. Gopalan. «Optical index profile at an antiparallel ferroelectric domain wall in lithium niobate». *Mat. Science and Eng.* **120**:91 – 94 (2005).

[117] D. Kip, B. Gather, H. Bendig, E. Krätzig. «Concentration and refractive index profiles of titanium and iron diffused planar $LiNbO_3$ waveguides». *Phys. Stat. Sol* **139**(241):241 – 248 (1993).

[118] D. Kip, M. Wesner. *Photorefractive Waveguides*. Springer Verlag, ?? (2003).

[119] K. Kitamura, J. K. Yamamoto, N. Iyi, S. Kimura, T. Hayashi. «Stoichiometric $LiNbO_3$ single crystal growth by double crucible Czochralski method using automatic powder supply system». *J. Cryst. Growth* **116**:327–332 (1992).

[120] Y. Kondo, Y. Fujii. «Photorefractive effects in PE waveguiding layers formed on $LiNbO_3$ and $LiTaO_3$». *Jpn. J. Appl. Phys.* **34**:L309 (1995).

[121] Yu. N. Korkishko, V. A. Fedorov. «Structural phase diagram of $h_xli_{1-x}nbo_3$ waveguides: The correlation between optical and structural properties». *Journal of selected topics in quantum electronics* **2**:187–196 (1996).

[122] M. Kösters, U. Hartwig, Th. Woike, K. Buse, B. Sturman. «Quantitative characterization of periodically poled lithium niobate by electrically induced bragg diffraction». *Appl. Phys. Lett.* **88**:182910 (2006).

[123] S. M. Kostritskii, O. G. Sevostyanov. «Influence of intrinsic defects on light-induced changes in the refractive index of lithium niobate crystals». *Appl. Phys. B* **65**:527–533 (1997).

[124] L. Kovacs, K. Polgar. *Properties of Lithium Niobate*. EMIS Datareviews Series. INSPEC (1989).

[125] L. Kovács, G. Ruschhaupt, K. Polgár, G. Corradi, M. Wöhlecke. «Composition dependence of the ultraviolet absorption edge in lithium niobate». *Appl. Phys. Lett* **70**(21):2801–2803 (1997).

[126] M. Kuneva, S. Tonchev, M. Pashtrapanska, I. Nedkov. «Proton exchange in y-cut $LiNbO_3$». *Materials science in semiconductor processing* **3**:581–583 (2000).

[127] J. Lamela, A. Rodenas, G. Lifante, D. Jaque, F. Jaque, A.A. Kaminskii. «Light confinement in periodically poled nonlinear laser-host crystal $ba_2nanb_5o_{15}$ (BNN).» *J. Appl. Physics* p. Sent (2007).

[128] F. Laurell, M. G. Roelofs, H. Hsiung. «Loss of optical nonlinearity in proton-exchanged $LiNbO_3$ waveguides». *Appl. Phys. Lett.* **60**:301 (1992).

[129] J. Lee, M. P. Singh, J. Zucker. «Suppresion of higher harmonic generations of SAW in $LiNbO_3$». *Appl. Phys. Lett.* **36**(11):896–898 (1980).

[130] Y.L. Lee, H. Suche, G. Schreiber, R. Ricken, V Quiring, W. Sohler. «Periodical domain inversion in singlemode ti:mg0:LiNb03 channel waveguides». *Electronics letters* **38**(5):812 – 813 (2002).

[131] M. J. Li, M. de Micheli, Q. He, D. B. Ostrowsky. «Cerenkov configuration second harmonic generation in proton-exchanged lithium niobate guides». *IEEE J. Quantum Electronics* **26**(8):1384 – 1393 (1990).

[132] E. J. Lim, M. M. Fejer, R. L. Byer. «Blue light generation by frequency doubling in periodically poled lithium niobate channel waveguide». *Electronics letters* **25**(11):730 – 731 (1989).

[133] E. J. Lim, M. M. Fejer, R. L. Byer. «Second harmonic generation of green light in periodically poled planar lithium niobate waveguide». *electronics letters* **25**(3):174 – 175 (1989).

[134] E. J. Lim, H. M. Hertz, M. L. Bortz, M. M. Fejer. «Infrared radiation generated by quasi-phase-matched difference-frequency mixing in a periodically poled lithium niobate waveguide». *Appl. Phys. Lett* **59**(18):2207 – 2209 (1991).

[135] J. Liu, P. P. Banerjee, Q. W. Song. «Role of diffusive, photovoltaic, and thermal effects in beam fanning in $LiNbO_3$». *J. Opt. Soc. Am.* **11**(9):1688–1693 (1994).

[136] A. Loni, G. Hay, R. M. De la Rue, J. M. Winfield. «Proton-exchanged $LiNbO_3$ waveguides: The effects of post-exchange annealing and buffered melts as determined by infrared spectroscopy, optical waveguide measurements, and hydrigen isotopic exchange reactions». *J. Lightw. Technol.* **7**(6):911–919 (1989).

[137] F. Lu, T. Zhang, X. Wang, S. Li, K. Wang, D. Shen, H. Ma. «Formation of waveguides by implantation of 3.0 MeV ni^{2+}». *Journal of Applied Physics* **96**(6):3463 – 3466 (2004).

[138] M. Luennemann, U. Hartwig, K. Buse. «Improvements of sensitivity and refractive-index changes in photorefractive iron-doped lithium niobate crystals by application of extremely large external electric fields». *J. Opt. Soc. Am* **20**(8):1643 – 1648 (2003).

[139] G. Malovichko, V. Grachev, O. Schirmer. «Interrelation of intrinsic and extrinsic defects - congruent, stoichiometric, and regularly ordered lithium niobate». *Appl. Phys. B* **68**:185–193 (1999).

[140] G. I. Malovichko, V. G. Grachev, L. P. Yurchenko, V. Y. Proshko, E. P. Kokanyan, V. T. Gabrielyan. «Improvement of $LiNbO_3$ microstructure by crystal growth with potassium». *Phys. Stat. Solidi* **133**(1):K29–K32 (1992).

[141] A. M. Mamedov. «Optical properties (VUV region) of $LiNbO_3$». *Opt. Spectrosc. (USRR)* **56**(6):645 – 649 (1984).

[142] P. Mathey, P. Jullien. «Numerical analysis of a WKB inverse method in view of index profile reconstruction in diffused waveguides». *Optics Comm.* **122**:127–134 (1996).

[143] B. T. Matthias, J. P. Remeika. «Ferroelectricity in the ilmenite structure». *Phys. Rev.* **76**:1886 (1949).

[144] A. Méndez, G. de la Paliza, A. García-Cabañes, J.M. Cabrera. «Comparison of the electro-optic coefficient r_{33} in well-defined phases of proton exchanged $LiNbO_3$ waveguides». *Applied Physics B* **73**:485–488 (2001).

[145] A. Méndez, A. García-Cabañes. *Private communication* (2007).

[146] A. Méndez, A. García-Cabañes, M. Carrascosa, J.M. Cabrera. «Photorefractive charge compensation in α-phase proton-exchanged $LiNbO_3$ waveguides». *J. Opt. Soc. Am. B* **17**(8):1412–1419 (2000).

[147] R.C. Miller, A. Savage. «Dierect observation of antiparalell domains during polarization reversal in single-crystal barium tantanate». *Phisical Review Letters* **2**:294 – 297 (1959).

[148] Mark J. Missey, Steve Russell, Vince Dominic, Robert G. Batchko, Kenneth L. Schepler. «Real-time visualization of domain formation in periodically poled lithium niobate». *Optics Express* **6**(10):186 – 195 (2000).

[149] K. Mizuuchi, A. Morikawa, T. Sugita, K. Yamamoto. «Electric field poling in mg-doped $LiNbO_3$». *Journal of Applied Physics* **96**(11):6585 – 6590 (2004).

[150] F. H. Mok. «Angle-multiplexed storage of 5000 holograms in lithium niobate». *Optics Lett.* **18**:915–917 (1993).

[151] M. Molotskii. «Foward motion of ferrroelectric domain walls». *Philosophical Magazine Letters* **83**(12):763 – 767 (2003).

[152] M. Müller, E. Soergel, K. Buse. «Influence of ultraviolet illumination on the poling characteristics of lithium niobate rystals». *Appl. Phys. Letters* **83**(9):1824 – 1826 (2003).

[153] M. Müller, E. Soergel, K. Buse. «Visualization of ferroelectric domains with coherent light». *Optics Letters* **28**(24):2515 (2003).

[154] M. Müller, E. Soergel, M. C. Wengler, K. Buse. «Light deflection from ferroelectric domain boundaries». *Appl. Phys. B* **78**:367 – 370 (2004).

[155] R. Müller, M.T. Santos, L. Arizmendi, J.M. Cabrera. «A narrow-band interference filter with photorefractive $LiNbO_3$». *Journal of Physics D: Applied Physics* **27**:241–246 (1994).

[156] K. Nakamura, H. Shimizu. «Hysteresis-free piezoelectric actuators using $LiNbO_3$ plates with a ferroelectric inversion layer». *Ferroelectrics* **93**:211–216 (1989).

[157] Koichiro Nakamura, Jonathan Kurz, Krishnan Parameswaran, M. M. Fejer. «Periodic poling of magnesium-oxide-doped lithium niobate». *Journal of applied physics* **91**:45284534 (2002).

[158] K. Nassau, H. J. Levinstein, G. M. Loiacono. «Ferroelectric lithium niobate. 1. growth, domain structure, dislocations and etching». *J. Phys. Chem. Solids* **27**:983–988 (1966).

[159] K. Nassau, H. J. Levinstein, G. M. Loiacono. «Ferroelectric lithium niobate. 2. preparation of single domain crystals». *J. Phys. Chem. Solids* **27**:989–996 (1966).

[160] R. Nevado, G. Lifante. «Low-loss, damage-resistant optical waveguides in Zn-diffused $LiNbO_3$ by a two-step procedure». *Appl. Phys. A* **72**(6):725–728 (2001).

[161] H. M. O'Bryan, P. K. Gallagher, C. D. Brandle. «Congruent composition and li-rich phase boundary of $LiNbO_3$». *J. Am. Ceram. Soc.* **68**(9):493–496 (1985).

[162] S. Odulov, T. Tarabrova, A. Shumelyuk, I. I. Naumova, T. O. Chaplina. «Photorefractive response of bulk periodically poled $LiNbO_3$:y:fe at high and low spatial frequencies». *Phys. Rev. Lett.* **84**(15):3294 (2000).

[163] J. Olivares. *Guías de onda planares en $LiNbO_3$ por intercambio protónico*. Ph.D. thesis, Univ. Autónoma de Madrid (1994).

[164] J. Olivares, G. García, A. García-Navarro, F. Agulló-López, **O. Caballero**, A. García-Cabañes. «Generation of high-confinement step-like optical waveguides in $LiNbO_3$ by swift heavy ion-beam irradiation». *Applied Physics Letters* **86**:183501 (2005).

[165] J. Olivares, A. García-Navarro, G. García, F. Agulló-López, F. Agulló-Rueda, A. García-Cabañes, M. Carrascosa. «Buried amorphous layers by electronic excitation in ion-beam irrradiated lithium niobate: Structure and kinetics». *Journal of Applied Physics* **101**:033512 (2007).

[166] J. Olivares, A. García-Navarro, G. García, A. Méndez, F. Agulló-López. «Optical determination of three-dimensional nanotrack profiles generated by single swift-heavy ion impacts in lithium niobate». *Appl. Phys. Lett.* **89**:071923 (2006).

[167] J. Olivares, A. García-Navarro, G. García, A. Méndez, F. Agulló-López, A. García-Cabañes, M. Carrascosa, O. Caballero. «Non linear optical waveguides generated in lithium niobate by swift-ion irradiation at ultralow fluences». *Opt. Lett.* p. Accepted for publication (2007).

[168] J. Olivares, A. García-Navarro, A. Méndez, F. Agulló-López, G. García, A. García-Cabañes, M. Carrascosa. «Novel optical waveguides by in-depth controlled electronic damage with swift ions». *Nuclear Instr. and Methods in Phys. Res. B* p. In press (2007).

[169] Krishnan R. Parameswaran, Roger K. Route, Jonathan R. Kurz, Rotislav V. Roussev, M. M. Fejer, M. Fujimura. «Highly efficient second-harmonic generation in buried waveguides fromed by annealed and reverse proton exchange in periodically poled lithium niobate». *Opt. Lett.* **27**(3):179 – 181 (2002).

[170] Carlos Pascual. *Experimental Determination of Stopping Forces for Ions in Matter*. Ph.D. thesis, Universidad Autónoma de Madrid (2004).

[171] K. Peithmann, N. Korneev, M. Flashpöhler, K. Buse, E. Krätzig. «Investigation of small polarons in reduced iron-doped lithium niobate crystals by non-steady-state photcurrent techniques». *pys. stat. sol.* **178**(R1):1 – 3 (2000).

[172] G. E. Peterson, A. Carnevale. «^{93}Nb NMR linewidths in nonstoichiometric lithium niobate». *J. Chem. Phys.* **56**:4848 (1972).

[173] F.C. Philips. *An Introduction to Crystallography*. Oliver&Boyd, Edinburgh (1971).

[174] I. Pracka, A. L. Bajor, S. M. Kaczmarek, M. Swirkowicz, B. Kaczmarek, J. Kisielewski, T. Lukasiewicz. «Growth and characterization of $LiNbO_3$ single crystals doped with CU and fe ions». *Cryst. Res. Technol.* **34**(5-6):627–634 (1999).

[175] J. Rams Ramos. *Caracterización y fabricación de guías de onda por intercambio protónico en $LiNbO_3$*. Ph.D. thesis, Universidad Autónoma de Madrid (1998).

[176] J. Rams, A. Alcázar-de-Velasco, M. Carrascosa, J. M. Cabrera, F. Agulló-López. «Optical damage inhibition and thresholding effects in lithium niobate above room temperature». *Optics Commun.* **178**:211–216 (2000).

[177] J. Rams, J. M. Cabrera. «A far-field method for characterizing thin planar optical waveguides». *Opt. Commun.* **139**:205–208 (1997).

[178] J. Rams, J. M. Cabrera. «Near-field characterization method of thin planar optical waveguides». *J. Mod. Opt.* **46**(7):1137–1147 (1999).

[179] J. Rams, J. M. Cabrera. «Near field characterization of thin planar optical waveguides». *Journal of modern optics* **46**(7):1137 – 1147 (1999).

[180] J. Rams, J.M. Cabrera. «Second harmonic generation in the strong absorption regime». *Journal of modern optics* **47**:1659–1669 (2000).

[181] J. Rams, J. Olivares, P. J. Chandler, P. D. Townsend. «Second harmonic capabilities of ion implanted $LiNbO_3$ waveguides». *Journal of applied physics* **84**(9):5180 – 5183 (1998).

[182] A. Räuber. *Current Topics in Materials Science*, volume 1. North Holland Publishing Company, Holland (1978).

[183] D. Redfield, W. J. Burke. «Optical absorption edge of $LiNbO_3$». *Journal of Applied Physics* **45**(10):4566 – 4571 (1974).

[184] C. E. Rice. «The structure and properties of $Li_{1-x}H_xNbO_3$». *J. Sol. State Chem.* **64**(2):188–199 (1986).

[185] C. C. W. Ruppel, L. Reindl, R. Weigel. «SAW devices and their wireless communications aplications». *IEEE Microwave Magazine* pp. 65–71 (June 2002).

[186] F. P. Safaryan, R. S. Feigelson, A. M. Petrosyan. «An approach to the defect structure analysis of lithium niobate single crystals». *J. Appl. Phys.* **85**(12):8079–8082 (1999).

[187] B.E.A. Saleh, M.C. Teich. *Fundamentals of Photonics*. Wiley Series in Pure and Applied Optics. Wiley Interscience, USA (1991).

[188] L. B. Schein, P. J. Cressman, L. E. Cross. «Electrostatic measurements of tertiary pyroelectricity in partially clamped $LiNbO_3$». *Ferroelectrics* **22**:945–948 (1979).

[189] L. B. Schein, P. J. Cressman, L. E. Cross. «Electrostatic measurements of unusually large secondary pyroelectricity in partially clamped $LiNbO_3$». *Ferroelectrics* **22**:937–943 (1979).

[190] U. Schlarb, K. Betzler. «Refractive indices of lithium niobate as a function of temperature, wavelength and composition: A generalized fit». *Phys. Rev. B* **48**(21):15613–15620 (1993).

[191] U. Schlarb, S. Klauer, M. Wesselmann, K. Betzler, M. Wöhlecke. «Determination of the Li/Nb ratio in lithium niobate by means of birefringence and raman measurements». *Appl. Phys. A* **56**:311–315 (1993).

[192] G. Schreiber, H. Suche, Y. L. Lee, W. Grundkötter, V. Quiring, R. Ricken, W. Sohler. «Efficient cascaded difference frequency conversion in periodically poled ti:$LiNbO_3$ waveguides using pulsed and cw pumping». *Appl Phys B* **73**:501–504 (2001).

[193] M. D. Serrano, V. Bermúdez, L. Arizmendi, E. Diéguez. «Determination of the Li/Nb ratio in $LiNbO_3$ crystals grown by the czochralski method with k_2o added to the melt». *Journal of Crystal Growth* **210**:670 – 676 (2000).

[194] V. Shur, E. Rumyantsev, R. Batchko, G. Miller, M. Fejer, R. Byer. «Physical basis of the domain engineering in the bulk ferroelectrics». *Ferroelectrics* **221**:157 – 167 (1999).

[195] V. Y. Shur. «Kinetics of ferroelectric domains: Application of general approach to $LiNbO_3$ and $litao_3$». *J. Mater. Science* **41**:199 –210 (2006).

[196] V. Y. Shur, R.G.Batchko, E.L. Rumyantsev, G.D.Miller, M.M.Fejer, R.L.Byer. «Domain engineering: Periodic domain pattering in lithium niobate». *Proc. 11th ISAF:IEEE* pp. 299–406 (1999).

[197] V. Ya. Shur, E. L. Rumyantsev, R. G. Batchko, G. D. Miller, M. M. Fejer, R. L. Byer. «Domain kinetics in the formation of a periodic domain structure in lithium niobate». *Physics of the solid state* **41**(10):1681 – 1687 (1999).

[198] M. Simon, St. Wevering, K. Buse, E. Kratzig. «The bulk photovoltaic effect of photorefractive $LiNbO_3$:fe crystals at high light intensities». *J. Phys. D* **30**:144 – 149 (1997).

[199] O. D: D. Soares, M. J. D. Z. Silva. «Ion-exchanged slab waveguides characterization». *Opt. Acta* **33**(10):1321–1334 (1986).

[200] Shinichiro Sonoda, IsaoTsuruma, Masami Hatori. «Second harmonic generation in a domain-inverted MgO-doped $LiNbO_3$ waveguide by using a polarization axis inclined substrate». *Appl. Phys. Lett* **71**:3048 – 3050 (1997).

[201] D. L. Staebler, J. J. Amodei. «Thermally fixed holograms in $LiNbO_3$». *Ferroelectrics* **3**(2-4):107–113 (1972).

[202] B. Sturman, M. Aguilar, F. Agullo-Lopez, V. Pruneri, P. G. Kazansky. «Photorefractive nonlinearity of periodically poled ferroelectrics». *J. Opt. Soc. Am. B* **14**:2641–1649 (1997).

[203] Tomoya Sugita, Kiminori Mizzuchi, Yasuo Kitaoka, Kazuhisha Yamamoto. «Ultraviolet light generation in a periodically poled MgO:$LiNbO_3$ waveguide». *Jpn Journal of applied Physics* **40**:1751–1753 (2001).

[204] T. Suhara, H. Tazaki, H. Nishira. «Measurement of reduction in SHG coefficient of $LiNbO_3$ by proton exchange». *Electron. Lett.* **25**:1326 – 1328 (1989).

[205] L. O. Svaasand, M. Eriksrud, G. Nakken, A. P. Grande. «Solid solution range of $LiNbO_3$». *J. Cryst. Growth* **22**:230 (1974).

[206] K. L. Sweeney, L. E. Halliburton. «Oxygen vacancies in lithium niobate». *Applied Physics Letters* **43 (3)**:336–338 (1983).

[207] K.L. Sweeney, L. E. Halliburton, D. A. Bryan, R. R. Rice, H. E. Tomaschke. «Point deffects in mg-doped lithium niobate». *J. Appl. Phys* **57 (4)**:1036–1043 (1985).

[208] H. Tamada. «Coupled-mode analysis of second harmonic generation in the form ofCerenkov radiation from a planar optical waveguide». *IEEE J. Quant. Electronics* **27**(3):502–508 (1991).

[209] M. Tasson, H. Legal, J. C. Peuzin, F. C. Lissalde. «Mécanismes d'orientation de la polarisation spontanée dans le niobate de lithium au voisinage du point de curie». *Phys. Stat. Sol. (a)* **31**:729–737 (1975).

[210] M. Taya, M. C. Bashaw, M.M. Fejer. «Phtorefractive effects in periodically poled dielectrics». *Opt. Lett.* **21**:857 (1996).

[211] J.R. Tesmer, M. Nastasi. *Handbook of Modern Ion Beam Materials Analysis*. MRS, Pittsburg, Pennsilvania (1995).

[212] R. I. Tomov, T. K. Kabadjova, P. A. Atanasov, S. Tonchev, M. Kaneva, A. Zherikhin, R. W. Eason. «$LiNbO_3$ optical

waveguides deposited on sapphire by electric-field-assisted pulsed laser deposition». *Vacuum* **58**:396–403 (2000).

[213] P. D: Townsend. «Optical effects of ion implantation». *Rep. Prog. Phys.* **50**(5):501–558 (1987).

[214] R. C. Twu, C. Chih Huang, Way-Seen Wan. «Zn indiffusion waveguide polarizer on a y -cut $LiNbO_3$ at 1.32 $/mu$m wavelength». *IEEE PHOTONICS TECHNOLOGY LETTERS* **12**(2):161 – 163 (2000).

[215] D. Von der Linde, O. F. Schirmer, H. Kurz. «Intrinsic photorefractive effect of $LiNbO_3$». *Applied Physics* **15**:153–156 (1978).

[216] H. Wang, Y. Zhu, Z. Zhang, S. Zhu, N. Ming. «Study on the proton profile in proton-exchanged and heat-treated $LiNbO_3$ with domain reversal». *J. Phys. Condens. Matter* **7**:7583 – 7588 (1995).

[217] Jonas Webjorn, Sabeur Siala, Derek W. Nam, Robert G. Waarts, Robert J. Lang. «Visible laser sources based on frequency doubling in nonlinear waveguides». *IEEE J. Quant. Electronics* **33**:1673 – 1685 (1997).

[218] R. S. Weis, T. K. Gaylord. «Lithium niobate: Summary of physical properties and crystal structure». *Appl. Phys. A* **37**:191 – 203 (1985).

[219] M. C. Wengler, M. Müller, E. Soergel, K. Buse. «Poling dynamics of lithium niobate crystals». *Appl. Phys. B* **76**:393 (2003).

[220] A. A. Wernberg, H. J. Gysling, A. J. Filo, T. N. Blanton. «Epitaxial growth of lithium niobate thin films from a single-source organometallic precursor using metalorganic chemical vapor deposition». *Appl. Phys. Lett.* **62**:946–950 (1993).

[221] J.M. White, P.F. Heidrich. «Optical waveguide refractive index profiles determined from measurement of mode indices: A simple analysis». *Applied Optics* **15**(1):151–155 (1976).

[222] E. Wiesendanger, G. Güntherodt. «Optical anisotropy of $LiNbO_3$ and $KNbO_3$ in the interband transition region.» *Solid Stat. Comm.* **14**:303 (1974).

[223] A. P. Wilkinson, A. K. Cheetham, R. J. Jarman. «The defect structure of congruently melting lithium niobate». *J. Appl. Phys* **75**(5):3080 – 3083 (1993).

[224] W.W. Wong. *Properties of Lithium Niobate*. INSPEC, London, United Kingdom (2002).

[225] A. Yamada, H. Tamada, M. Saitoh. «$LiNbO_3$ thin-film optical waveguide grown by liquid phase epitaxy using Li_2O-B_2O_3 flux». *Appl. Phys. Lett.* **61**(24):2848–2851 (1992).

[226] M. Yamada, N. Nada, M. Saitoh, K. Watanabe. «First-order quasi-phase matched $LiNbO_3$ waveguide periodically poled by applying an external field for efficient blue second-harmonic generation». *Appl. Phys. lett* **62**(5):435 – 436 (1993).

[227] F. Yazdani, M. L. Sundheimer, A. S.L. Gomes. «Ferroelectric domain inversion in congruent lithium niobate». *Proc. SBMO/IEEE MTT-S IMOC* p. 453 (2003).

[228] S. Yin. «Lithium niobate fibers and waveguides: Fabrication and applications». *Proc. IEEE* **87**(11):1962–1974 (1999).

[229] W. M. Young, R. S. Feigelson, M. M. Fejer, M. J. F. Digonnet, H. J. Shaw. «Photorefractive-damage-resistant zn-diffused waveguides in mgo:$LiNbO_3$». *Optics Letters* **16**(13):995 – 997 (1991).

[230] Sungkyu Yu, A.M. Weiner. «Phase-matching temperature shifts in blue generation by frequency doubling of femtosecond pulses in KNbO3». *J. Opt. Soc. Am. B* **16**:1300 – 1304 (1999).

[231] Y. Zhang, Y. H. Xu, M. H. Li, Y. Q. Zhao. «Growth and properties of Zn doped lithium niobate crystal». *J. Crystal Growth* **233**:537–540 (2001).

[232] X. H. Zhen, L. C. Zhao, Y. H. Xu. «Defect structure and optical damage resistance of zn:fe:$LiNbO_3$ crystals». *Appl. Phys. B* **76**:655 – 659 (2003).

[233] G. Zhong, Z. Jian, Z. Wu. *Proc. IEEE* **80**(60-0):395–399 (1980).

[234] H. Zhong, Y. Hou, N. Quan, X. Chen, R. Wang. «Growth of lithium niobate single crystal fiber by an edge-defined, film-fed growth method». *Cryst. Res. & Tech.* **26**(4):395–399 (1991).

[235] S. Zhu, Y. Zhu, H Wang, Z Zhang, N Ming, Y Chang, X. Shen. «Field-induced periodic poled bulk $LiNbO_3$ using al electrodes». *J. Phys. D: Appl. Phys* **29**:76 – 79 (1996).

[236] Y. Y. Zhu, S. N. Zhu, J. F. Hong. «Domain inversion in $LiNbO_3$ by proton exchange and quick heat treatment». *Appl. Phys. Lett* **65**:558 (1994).

[237] N. Zotov, H. Boysen, F. Frey, T. Metzger, E. Born. «Cation substitution models of congruent $LiNbO_3$ investigated by x-ray and neutron powder diffraction». *J. Phys. Chem. Solids* **55**(2):145–152 (1994).